

Air Force Institute of Technology

AFIT Scholar

Theses and Dissertations

Student Graduate Works

3-2001

Optical and Etching Studies of Native Aluminum Oxide Layers for Use in Microcavity Photonic Devices

William L. Bernhard

Follow this and additional works at: <https://scholar.afit.edu/etd>



Part of the [Electromagnetics and Photonics Commons](#), and the [Semiconductor and Optical Materials Commons](#)

Recommended Citation

Bernhard, William L., "Optical and Etching Studies of Native Aluminum Oxide Layers for Use in Microcavity Photonic Devices" (2001). *Theses and Dissertations*. 4569.

<https://scholar.afit.edu/etd/4569>

This Thesis is brought to you for free and open access by the Student Graduate Works at AFIT Scholar. It has been accepted for inclusion in Theses and Dissertations by an authorized administrator of AFIT Scholar. For more information, please contact richard.mansfield@afit.edu.

AFIT/GE/ENG/01M-01



Optical and Etching Studies of Native Aluminum Oxide
Layers for Use in Microcavity Photonic Devices

THESIS

William L. Bernhard
Captain, USAF

AFIT/GE/ENG/01M-01

DEPARTMENT OF THE AIR FORCE

AIR UNIVERSITY

AIR FORCE INSTITUTE OF TECHNOLOGY

Wright-Patterson Air Force Base, Ohio

Approved for public release; distribution unlimited.

20010706 126

REPORT DOCUMENTATION PAGE

Form Approved
OMB No. 0704-0188

Public reporting burden for this collection of information is estimated to average 1 hour per response, including the time for reviewing instructions, searching existing data sources, gathering and maintaining the data needed, and completing and reviewing the collection of information. Send comments regarding this burden estimate or any other aspect of this collection of information, including suggestions for reducing this burden to Washington Headquarters Services, Directorate for Information Operations and Reports, 1215 Jefferson Davis Highway, Suite 1204, Arlington, VA 22202-4302, and to the Office of Management and Budget, Paperwork Reduction Project (0704-0188), Washington, DC 20503.

PLEASE DO NOT RETURN YOUR FORM TO THE ABOVE ADDRESS.

1. REPORT DATE (DD-MM-YYYY) 07-03-2001		2. REPORT TYPE Master's Thesis		3. DATES COVERED Sep 2000 - Mar 2001	
4. TITLE AND SUBTITLE OPTICAL AND ETCHING STUDIES OF NATIVE ALUMINUM OXIDE LAYERS FOR USE IN MICROCAVITY PHOTONIC DEVICES				5a. CONTRACT NUMBER	
				5b. GRANT NUMBER	
				5c. PROGRAM ELEMENT NUMBER	
6. AUTHOR(S) WILLIAM LEE BERNHARD Captain, USAF				5d. PROJECT NUMBER	
				5e. TASK NUMBER	
				5f. WORK UNIT NUMBER	
7. PERFORMING ORGANIZATION NAME(S) AND ADDRESS(ES) AFIT/ENGBldg 640 2950 P Street WPAFB, OH 45433-7765				8. PERFORMING ORGANIZATION REPORT NUMBER AFIT/GE/ENG/01M-01	
9. SPONSORING/MONITORING AGENCY NAME(S) AND ADDRESS(ES) Dr Thomas R. Nelson, Jr. AFRL/SNDD Bldg 620 2241 Avionics Circle Ste 20 WPAFB, OH 45433-7322 (937) 255-1874 x3512				10. SPONSOR/MONITOR'S ACRONYM(S)	
				11. SPONSOR/MONITOR'S REPORT NUMBER(S)	
12. DISTRIBUTION/AILABILITY STATEMENT Approved for public release; distribution unlimited					
13. SUPPLEMENTARY NOTES					
14. ABSTRACT Optical communication and computing systems are required to meet future information transfer and processing needs . Microcavity devices serve as an enabling technology to implement and integrate optoelectronic systems. It is important to understand the optical and mechanical properties of materials utilized within microcavity devices. Only then is it possible to accurately model and analyze structures. Microcavity structures incorporating high aluminum content AlGaAs layers are designed, grown, processed, and measured. The processing of these devices includes the conversion of high aluminum-content AlGaAs layers to native aluminum oxide (AlO) layers through the process of thermal oxidation. This selective conversion of microcavity layers provides for the necessary electrical and optical confinement required to produce a plethora of microphotonic devices. The optical properties of hydrolyzed AlO layers within a monolithic microcavity structure are experimentally determined. Also examined is the induced AlO layer stress, a result of volumetric shrinkage. Additional mechanical properties of GaAs/AlAs multilayer Fabry-Perot etalon structures are explored through the process of chemical etching. A suitable chemical solution to selectively etch converted AlO layers within a microcavity structure is developed. This research provides the foundation for future III-V MEMS technology development.					
15. SUBJECT TERMS Aluminum Oxide Refractive Index Etching Semiconductor Lasers Microelectromechanical Systems					
16. SECURITY CLASSIFICATION OF:			17. LIMITATION OF ABSTRACT	18. NUMBER OF PAGES	19a. NAME OF RESPONSIBLE PERSON
a. REPORT	b. ABSTRACT	c. THIS PAGE			James A. Lott, AFIT/ENG, Lt Col, USAF
Unclassified	Unclassified	Unclassified	SAR	138	19b. TELEPHONE NUMBER (Include area code) 937-255-3636 x 4576

The views expressed in this thesis are those of the author and do not reflect the official policy or position of the United States Air Force, Department of Defense, or the United States Government.

AFIT/GE/ENG/01M-01

Optical and Etching Studies of Native Aluminum Oxide
Layers for Use in Microcavity Photonic Devices

THESIS

Presented to the Faculty of the Graduate School of Engineering and Management
of the Air Force Institute of Technology
Air University
In Partial Fulfillment of the
Requirements for the Degree of
Master of Science in Electrical Engineering

William L. Bernhard, B.S.E.E.

Captain, USAF

March 2001

Approved for public release; distribution unlimited.

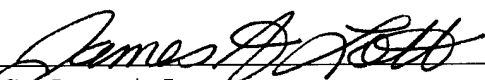
Optical and Etching Studies of Native Aluminum Oxide
Layers for Use in Microcavity Photonic Devices

THESIS

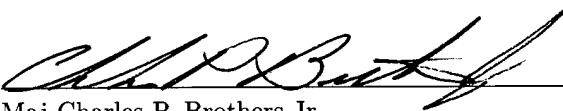
William L. Bernhard, B.S.E.E.

Captain, USAF

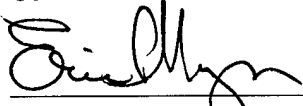
Approved:


Lt Col James A. Lott
Chairman

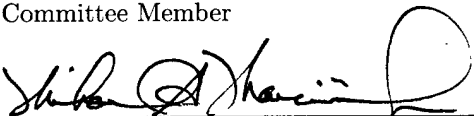
07 MARCH 2001
Date


Maj Charles P. Brothers Jr.
Committee Member

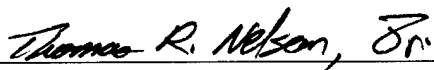
7 Mar 01
Date


Maj Eric P. Magee
Committee Member

7 MAR 01
Date


Lt Col Michael A. Marciniak
Committee Member

7 Mar 01
Date


Dr. Thomas R. Nelson Jr. (AFRL)
Committee Member

3/7/01
Date

Preface

My time at AFIT has been a true test of will and motivation. It has been a learning, trying, exciting, frustrating, and fulfilling experience all wrapped into one. I would just like to acknowledge and thank those who helped me, guided me, inspired me, and afforded me the opportunity to complete my research.

First I would like to thank Mr and Mrs Brad Thode for their innovation, creativity, love of teaching, and time spent with me during my younger years to instill an appreciation and an appropriate level of fascination in me for the field of technology as a whole.

Next, I would like to give thanks my advisor, Lt Col James Lott, for introducing me to the exciting optoelectronic field. This field offers many challenges, opportunities for new research, and possibilities for great rewards. Thanks also to my committee members for their time spent reviewing my manuscript and for their insightful comments.

I would also like to recognize my mentors and co-workers at AFRL for their support to my research efforts. Dr. Stu Feld taught me more in two weeks about fabrication processes than I could have ever gleaned from reading a textbook. Dr. Tom Nelson proved to be an invaluable mentor who taught me much about optical bench testing, design methodologies, and generally how to overcome shortfalls. His late nights and hours spent "explaining" are truly appreciated. The AFIT PhD candidate crew was a big help in overcoming technical obstacles and other events; the assistance of "Fast" Eddie Ochoa, Vern Starman, and Todd Hale was a tremendous help. Special thanks also to Bill (60') Siskaninetz, Jim Ehret, Paul Cassity, Becky Cortez, and Wally Rice for all of their processing and characterization help.

Next on the list of thanks are the friends I've made while here at AFIT. It would have been a rough road without friends to smooth things out and provide an opportunity to blow off some steam and enjoy the fun side of life from time to time. Our weekly lunches and other miscellaneous adventures made life enjoyable during some of the downtrodden times.

I owe a special debt of thanks to my parents, Lee and Jan, who have always given me support and encouragement for all of my endeavors. I thank them for all they have done in their efforts to "raise me right", for being my role models, and for always allowing me to follow my ambitions; whatever they may be.

Finally I would like to thank the love of my life, Susan, for her understanding, patience, and support even when my normally happy self seemed to go on vacation without me. Thanks for everything, I could not have made it without you!

Table of Contents

	Page
Preface	iii
List of Figures	viii
List of Tables	xiii
List of Symbols	xiv
List of Abbreviations	xv
Abstract	xvi
1. Introduction	1-1
1.1 Motivation	1-1
1.2 Problem Statement	1-3
1.3 Thesis Scope and Approach	1-4
1.4 Thesis Outline	1-5
2. Device Theory	2-1
2.1 Introduction	2-1
2.2 Brief History of Microcavity Devices	2-1
2.3 VCSEL Device Theory	2-2
2.4 Oxide Layers in Microcavity Devices	2-11
2.4.1 Advantages of Oxide Layers in Optoelectronic Devices	2-11
2.4.2 Oxide Growth Kinetics	2-14
2.5 Regression Analysis	2-19
2.6 Chapter 2 Summary	2-23

	Page
3. Modeling, Simulation, and Design	3-1
3.1 Introduction	3-1
3.2 Reflectance, Transmittance, and Absorptance Calculations	3-1
3.3 Reflectivity vs. Etch Depth Simulation	3-6
3.4 Regression Analysis and Curve Fitting Techniques	3-6
3.5 Design of Microcavity Test Structures	3-12
3.6 Chapter 3 Summary	3-22
4. Equipment for Device Fabrication and Characterization	4-1
4.1 Introduction	4-1
4.2 Molecular Beam Epitaxy Growth	4-2
4.3 MBE Reflectance System	4-4
4.4 Device Processing	4-6
4.4.1 Mask Alignment	4-6
4.4.2 Metal Deposition	4-6
4.4.3 Mesa Definition and Plasma Etching Reflectance System	4-7
4.5 Oxidation System	4-7
4.6 Reflectance Measurements	4-10
4.7 Focused Ion Beam Scanning Electron Microscope System	4-13
4.8 Selective Etching Techniques	4-14
4.9 Chapter 4 Summary	4-15
5. Results and Analysis	5-1
5.1 Introduction	5-1
5.2 Initial Experiments	5-1
5.2.1 Wet Chemical Mesa Definition Etch Study	5-2
5.2.2 Initial Oxidation System Evaluation	5-3
5.3 Sample Growth and Analysis	5-9

	Page
5.4 Aluminum Oxide Refractive Index Values	5-15
5.5 Selective Etching of Oxidized Layers	5-21
5.6 Chapter 5 Summary	5-27
6. Contributions, Conclusions and Suggestions for Further Research	6-1
6.1 Contributions and Conclusions	6-1
6.2 Further Research	6-1
Appendix A. VCSEL Fabrication	A-1
A.1 VCSEL Fabrication Process	A-1
Appendix B. Oxidation System Operation Guide	B-1
B.1 Oxidation System "How To" Manual	B-1
Appendix C. MATLAB Simulations	C-1
C.1 MATLAB Simulations of Existing AFRL Samples	C-1
References	BIB-1
Vita	VITA-1

List of Figures

Figure		Page
1.1.	Schematic of a typical VCSEL structure	1-2
1.2.	Importance of information superiority as related to Joint Vision 2010 [5]. . .	1-3
2.1.	Comparison of emission orientation between; (a) edge emitting lasers (EELs) and (b) vertical cavity surface emitting lasers (VCSEL)	2-3
2.2.	Distributed Bragg Reflector (DBR) using alternating high- and low-index layers [3].	2-7
2.3.	Power reflectance as a function of number of quarter-wave pairs (N_p) for a DBR structure (GaAs and AlAs quarter-wave layers) on a GaAs substrate designed for λ_{Bragg} equal to 700nm for normally incident light.	2-8
2.4.	Semiconductor band-to-band recombination processes [43].	2-10
2.5.	Calculated power reflectance spectrum for a 980nm etalon structure composed of alternating layers of GaAs and AlAs on a GaAs substrate containing a 1.5- λ microcavity composed of AlAs; $N_{P-Top} = 18.5$ and $N_{P-Bottom} = 18$	2-12
2.6.	Comparison of power reflectance for etalon structures composed of GaAs/AlAs DBRs (solid line) and GaAs/AlO DBRs (dashed line)	2-13
2.7.	Comparison of optical losses for small geometry VCSEL devices: (a) oxide-apertured device (b) etched air post device, after [52].	2-14
2.8.	Comparison of the number of high/low quarter-wave pairs (periods), N_p , needed to achieve 99% power reflectance (structure designed for λ_{Bragg} of 700nm).	2-15
2.9.	Monolithically grown oxide-aperture VCSEL device schematic after oxidation [52].	2-17
2.10.	Threshold current and threshold current density for an oxide-confined VCSEL device as a function of oxide aperture radius [18].	2-18
2.11.	Al mole fraction and temperature-dependence of oxidation rate;	2-20
3.1.	Calculated power reflectance spectra for AFRL sample G2 – 2651 (normal incidence).	3-3

Figure		Page
3.2.	Calculated power transmittance spectra for AFRL sample <i>G2</i> – 2651 (normal incidence).	3-4
3.3.	Calculated power absorptance spectra for AFRL sample <i>G2</i> – 2651 (normal incidence).	3-5
3.4.	Calculated axial standing wave electric field intensity pattern for AFRL Sample <i>G2</i> – 2651.	3-7
3.5.	Calculated power reflectance as a function of wavelength and layer thickness ($\pm 10\%$) for the microcavity (AlAs) region for AFRL sample <i>G2</i> – 2651 (Fabry-Perot etalon structure).	3-8
3.6.	Calculated power reflectance as a function of wavelength and layer thickness variation ($\pm 10\%$) for the high (GaAs) quarter-wave layer in AFRL sample <i>G2</i> – 2651. Minimal shift in the F-P dip is observed.	3-9
3.7.	Calculated power reflectance as a function of wavelength and layer thickness variation ($\pm 10\%$) for the low (AlAs) quarter-wave layer in AFRL sample <i>G2</i> – 2651. Minimal shift in the F-P dip is observed.	3-10
3.8.	Calculated power reflectance as a function of etch depth for a 20-period GaAs-AlAs DBR on a GaAs substrate designed for $\lambda_{Bragg} = 800\text{nm}$ as seen in response to normally-incident 800nm light.	3-11
3.9.	Calculated and measured reflectance spectra for AFRL sample <i>G2</i> – 2477.	3-13
3.10.	Progression of regression analysis for AFRL sample <i>G2</i> – 2477 for iterations 1-10;	3-14
3.11.	Calculated and measured reflectance spectra for AFRL sample <i>G2</i> – 2477 (28-period DBR structure @ 980 nm) after regression analysis and change of physical layer thickness values.	3-15
3.12.	Calculated power reflectance spectra for AFRL sample <i>G2</i> – 2652.	3-17
3.13.	Calculated power reflectance spectra for AFRL sample <i>G2</i> – 2658.	3-19
3.14.	Calculated power reflectance spectra for AFRL sample <i>G2</i> – 2663. Sample is evaluated for both pre- and post-oxidation.	3-20
3.15.	Calculated standing wave pattern (electric field intensity) and refractive index profile for AFRL sample <i>G2</i> – 2663. Inset shows zoomed in view of InGaAs quantum well region and the overlap with the standing wave pattern.	3-21

Figure		Page
4.1.	Photograph of the Air Force Research Laboratory's Varian Gen II molecular beam epitaxy system used to grow my test structures.	4-2
4.2.	Schematic of the Air Force Research Laboratory's Varian Gen II molecular beam epitaxy system used to grow my test structures.	4-3
4.3.	Schematic of MBE reflectance measuring system used to calibrate epitaxial growth rates immediately following a process run [33].	4-4
4.4.	Measured reflectance spectrum for sample <i>G2</i> – 2651 (3- λ thick AlAs cavity with GaAs/AlAs DBR mirror layers) as taken immediately after MBE growth.	4-5
4.5.	Microscope view of features patterned using MJB-3 mask aligner after a subsequent mesa etch using the ICP system (AFRL sample <i>G2</i> – 2658 patterned with VCSEL Mask 02).	4-6
4.6.	Schematic of the ICP etch chamber in-situ reflectance measurement system [33].	4-8
4.7.	Data collected from the ICP laser reflectometry system (during ICP mesa etch of AFRL sample <i>G2</i> – 2651). The measurement wavelength is 760nm.	4-9
4.8.	Mesa etch profile comparison for wet and dry etching techniques.	4-9
4.9.	Schematic of AFRL's custom-built AFRL oxidation system [18].	4-11
4.10.	Photograph of the custom-built AFRL low-pressure oxidation system [18].	4-12
4.11.	Schematic of small-spot reflectance measurement system.	4-13
4.12.	Photograph of AFRL FEI 620 dual beam FIB/SEM workstation	4-14
5.1.	Microscope images of AFRL sample <i>G2</i> – 2612C1 showing (a) sample etched for 1:15 min in a sulfuric acid solution and (b) the same sample after 1:45 min sulfuric acid solution etch.	5-4
5.2.	Microscope images of samples <i>G2</i> – 2612C2 and <i>G2</i> – 2612C3 after citric acid etch.	5-5
5.3.	Microscope images of AFRL sample <i>G2</i> – 2612C4 after sulfuric acid solution etch.	5-6
5.4.	Microscope images of AFRL sample <i>G2</i> – 2477 (28-period DBR) with (a) gold contact ring and (b) Metal contact ring removed via Technostrip and BOE etch.	5-7
5.5.	Microscope images of AFRL sample <i>G2</i> – 2477 (28-period DBR) after oxidation.	5-8

Figure	Page
5.6. SEM micrographs of AFRL sample <i>G2</i> – 2612 <i>C</i> 5 and AFRL sample <i>G2</i> – 2612 <i>C</i> 4.	5-10
5.7. SEM micrographs of AFRL sample <i>G2</i> – 2612 (#4 and #5) after FIB milling.	5-11
5.8. Measured MBE reflectometry system power reflectance for AFRL sample <i>G2</i> – 2651 (etalon structure with GaAs/AlAs DBR layers and a 3λ -thick AlAs microcavity)	5-12
5.9. Measured MBE reflectometry system power reflectance for AFRL sample <i>G2</i> – 2651 compared to initial calculated power reflectance values. (etalon structure with GaAs/AlAs DBR layers and a 3λ -thick AlAs microcavity).	5-13
5.10. Measured MBE reflectometry system power reflectance for AFRL sample <i>G2</i> – 2651 (etalon structure with GaAs/AlAs DBR layers and a 3λ -thick AlAs microcavity) compared to calculated power reflectance values after adjusting layers via regression analysis fitting technique.	5-14
5.11. Measured power reflectance and calculated power reflectance after regression fit for AFRL sample <i>G2</i> – 2652 (2λ -thick GaAs microcavity etalon).	5-16
5.12. Post-oxidation microscope images of AFRL sample <i>G2</i> – 2651 showing deleterious effects of layer shrinkage (3λ -thick AlAs microcavity etalon).	5-18
5.13. Post-oxidation micrographs of AFRL sample <i>G2</i> – 2651 showing induced stress and layer delamination as a result of the oxidation process (3λ -thick AlAs microcavity etalon).	5-19
5.14. Measured post-oxidation power reflectance spectrum for AFRL sample <i>G2</i> – 2652 (2λ -thick GaAs microcavity etalon).	5-20
5.15. Index of refraction for aluminum oxide converted through oxidation in the AFRL custom-built oxidation system @ 400°C.	5-22
5.16. Comparison of previous AFRL AlO (dotted line) dispersion file and my extracted Cauchy parameter fit model (solid line) to measured data.	5-23
5.17. Comparison of calculated reflectance spectrum for AFRL sample 2658 to measured data. The figure shows a comparison of reflectance calculations between a model using my extracted Cauchy parameter fit and one calculated using the previous AFRL dispersion curve [29].	5-24

Figure	Page
5.18. Example of tunable etalon structure designed around a central Bragg wavelength of 980nm. Modulation of the air gap inside the microcavity shifts the location of the Fabry-Perot dip as a function of air gap thickness.	5-25
5.19. AFRL sample <i>G2</i> – 2652 <i>Aii</i> after 30 sec HF:H ₂ O (2:10) etch.	5-28
5.20. SEM micrograph of AFRL sample <i>G2</i> – 2652 <i>Aii</i> after 30 sec HF:H ₂ O (2:10) etch.	5-29
5.21. SEM micrographs of AFRL sample <i>G2</i> – 2652 <i>Aiv</i> after 60 seconds AZ400K etch.	5-30
5.22. SEM micrographs of AFRL sample <i>G2</i> – 2652 <i>Ai</i> after 30 sec BOE etch. . .	5-31
5.23. Microscope image of AFRL sample <i>G2</i> – 2658 after oxidation.	5-32
5.24. Micrographs of mesa structures on sample <i>G2</i> – 2658 <i>C3i</i> after 60 sec BOE etch.	5-33
5.25. Micrographs of alignment marks on sample <i>G2</i> – 2658 <i>C3i</i> after 60 sec BOE etch.	5-34
C.1. Pre- and post- oxidation MATLAB simulation for AFRL sample <i>G2</i> – 2379. Growth starting at substrate: GaAs(3000Å); AlAs(834Å)/GaAs(695Å), repeat 8 times; AlAs(834Å); GaAs(300Å); GaAs(780Å); AlAs(411Å)/GaAs(218Å), repeat 8 times	C-1
C.2. Pre- and post- oxidation MATLAB simulation for AFRL sample <i>G2</i> – 2406. Growth starting at substrate: GaAs(1000Å); AlAs(834Å)/GaAs(695Å), repeat 30 times; GaAs(695Å)	C-2
C.3. Pre- and post- oxidation MATLAB simulation for AFRL sample <i>G2</i> – 2476. Growth starting at substrate: GaAs(3000Å); AlAs(827Å)/GaAs(687Å), repeat 28 times	C-3
C.4. Pre- and post- oxidation MATLAB simulation for AFRL sample <i>G2</i> – 2478. Growth starting at substrate: GaAs(1000Å); AlAs(834Å)/GaAs(695Å), repeat 30 times; GaAs(695Å)	C-4
C.5. Pre- and post- oxidation MATLAB simulation for AFRL sample <i>G2</i> – 2612. Growth starting at substrate: AlAs(837Å)/GaAs(696Å), repeat 12 times; AlAs(5026Å); GaAs(696Å)/AlAs(837Å), repeat 10 times; GaAs(696Å)	C-5

List of Tables

Table	Page
3.1.	GaAs/AlAs Fabry-Perot Etalon (Sample G2-2651) 3-2
3.2.	DBR structure with λ_{Bragg} equal 800 nm used in calculation of power reflectance as a function of etch depth 3-6
3.3.	28 Period GaAs/AlAs DBR structure (AFRL Sample G2 – 2477) 3-12
3.4.	Pre- and Post-Regression Analysis Thickness values for AFRL Sample G2–2477 3-12
3.5.	Physical Layer Description for Fabry-Perot Etalon Structure with a 2λ -thick GaAs microcavity (AFRL sample G2-2652) 3-16
3.6.	Oxidation Test Structure 1 Physical Description (Sample G2-2658) 3-18
3.7.	Oxidation Test Structure 2 Physical Description(Sample G2-2663) 3-22
4.1.	Chronology of Completed Oxidation Runs 4-10
5.1.	Layer structure for AFRL Sample G2 – 2612 (Etalon with $\frac{3\lambda}{2}$ -thick AlAs microcavity) 5-2
5.2.	Etchants used in wet chemical mesa definition study on AFRL sample G2–2612) 5-2
5.3.	Pre- and Post-Regression Analysis Thickness Values (Sample G2 – 2651) . . 5-15
5.4.	Pre- and Post-Regression Analysis Thickness Values (Sample G2 – 2652, etalon structure with a 2λ -thick GaAs microcavity) 5-15
5.5.	Pre- and Post-Oxidation Step-Height Measurements (Sample G2 – 2658) . . 5-17
5.6.	Etchants Evaluated for their Ability to Selectively Etch AlO Sacrificial Layers 5-26

List of Symbols

Symbol		Page
h	Planck's Constant (J-s)	2-1
ν	Frequency (Hz)	2-1
λ_{Bragg}	Bragg Wavelength (nm)	2-4
d_l	Physical Layer Thickness (nm)	2-4
c_o	Speed of Light ($\frac{m}{sec}$)	2-4
ν_{phase}	Phase Velocity ($\frac{m}{sec}$)	2-4
n	Real Index of Refraction (unitless)	2-4
κ	Extinction Coefficient (unitless)	2-4
α	Absorption Coefficient (cm^{-1})	2-5
L	Cavity Length (μm)	2-5
$\Delta\lambda_{stopband}$	Stop Band (nm)	2-6
n_{eff}	Effective Index of Refraction (unitless)	2-6
E_g	Band-gap Energy (eV)	2-9
N_p	Number of High/Low Quarter Wave Pairs (unitless)	2-15
I_{th}	Threshold Current (A)	2-16
J_{th}	Threshold Current Density ($\frac{A}{cm^2}$)	2-16
λ_{th}	Threshold Lasing Wavelength (nm)	2-16
k	Boltzmann's Constant (J/K)	2-19
T	Temperature (K)	2-19

List of Abbreviations

Abbreviation		Page
VCSEL	Vertical Cavity Surface Emitting Laser	1-1
DBR	Distributed Bragg Reflector	1-1
VLSI	Very Large Scale Integration	1-3
GaAs	Gallium Arsenide	1-3
AlGaAs	Aluminum Gallium Arsenide	1-4
AlAs	Aluminum Arsenide	1-4
AlO	Aluminum Oxide	1-4
AFRL	Air Force Research Laboratory	1-4
CW	Continuous Wave	2-2
EEL	Edge Emitting Laser	2-2
MBE	Molecular Beam Epitaxy	2-2
MOVPE	Metal-Organic Vapor Phase Epitaxy	2-2
AFIT	Air Force Institute of Technology	2-6
QW	Quantum Well	2-11
LED	Light Emitting Diode	2-14
ICP	Inductively Coupled Plasma	3-6
CCD	Charge Coupled Device	4-10
InGaAs	Indium Gallium Arsenide	4-13
IR	Infrared	4-13
MEMS	Microelectromechanical Systems	4-14
BOE	Buffered Oxide Etch	4-15
DI	Deionized	4-15
FIB	Focused Ion Beam	5-9
SEM	Scanning Electron Microscope	5-9

Abstract

The advancement of optoelectronic devices and systems will play a vital role in the Air Force's ability to maintain information dominance. Optical communication and computing systems will be required to meet the information transfer and processing needs of the 21st century and beyond. Microcavity devices, such as vertical-cavity surface-emitting lasers (VCSELs), serve as an enabling technology to implement and integrate photonic devices and optoelectronic systems. It is important to understand the optical and mechanical properties of materials utilized within microcavity devices. Only then is it possible to accurately model and analyze device structures prior to expensive epitaxial growth by molecular beam epitaxy. Microcavity structures incorporating high aluminum content $Al_xGa_{1-x}As$ layers are designed, grown, processed, and calibrated. The processing of these devices includes the conversion of high aluminum-content $Al_xGa_{1-x}As$ layers to native aluminum oxide layers through the process of thermal oxidation. This selective conversion of microcavity layers provides for the necessary electrical and optical confinement required to produce ultra-low threshold VCSELs and a plethora of related micro-photonic devices. The optical properties of hydrolyzed aluminum oxide layers within a monolithically grown microcavity structure are experimentally determined. Also examined is the mechanically-induced oxide layer stress, a result of volumetric layer shrinkage. Additional mechanical properties of GaAs/AlAs distributed Bragg reflector and multilayer Fabry-Perot etalon structures are explored through the process of wet chemical etching. A suitable wet chemical etching procedure to define mesa structures as well as a procedure to selectively etch converted aluminum oxide layers within a monolithically grown microcavity structure is developed. An etch rate of 13.3 nm per second was determined for a buffered oxide etch solution. This research provides the foundation for future III-V MEMS technology development.

Optical and Etching Studies of Native Aluminum Oxide Layers for Use in Microcavity Photonic Devices

1. Introduction

1.1 Motivation

Optics is the key to the information age. Current and future Air Force systems will rely heavily on the ability to transmit and receive vast amounts of data in near real time. Advanced optoelectronic and micro-photonic devices such as the vertical cavity surface emitting laser (VCSEL) and related microcavity structures are critical components of evolving military information technology, space, and communication systems. These devices are under development for use in a variety of systems including: high-speed optical data links, free-space optical interconnects, integrated photonic switching elements, and environmental sensing systems. A typical VCSEL structure is shown in Figure 1.1. These devices, which have diameters as small as 20 μm , consist of a microcavity region surround by two highly reflective distributed Bragg reflector (DBR) mirror structures. Future military air and space systems will certainly include advanced micro-optical information processing and communication sub-systems containing millions of tiny microcavity lasers, detectors, and related sensors. Increased understanding, characterization, and further development of these devices is necessary to ensure America's information dominance in the 21st century and beyond. Figure 1.2 illustrates the important nature of information dominance and how it serves as the foundation of Joint Vision 2010. The pillars of military operation are rooted in the technological innovations that lead to information superiority.

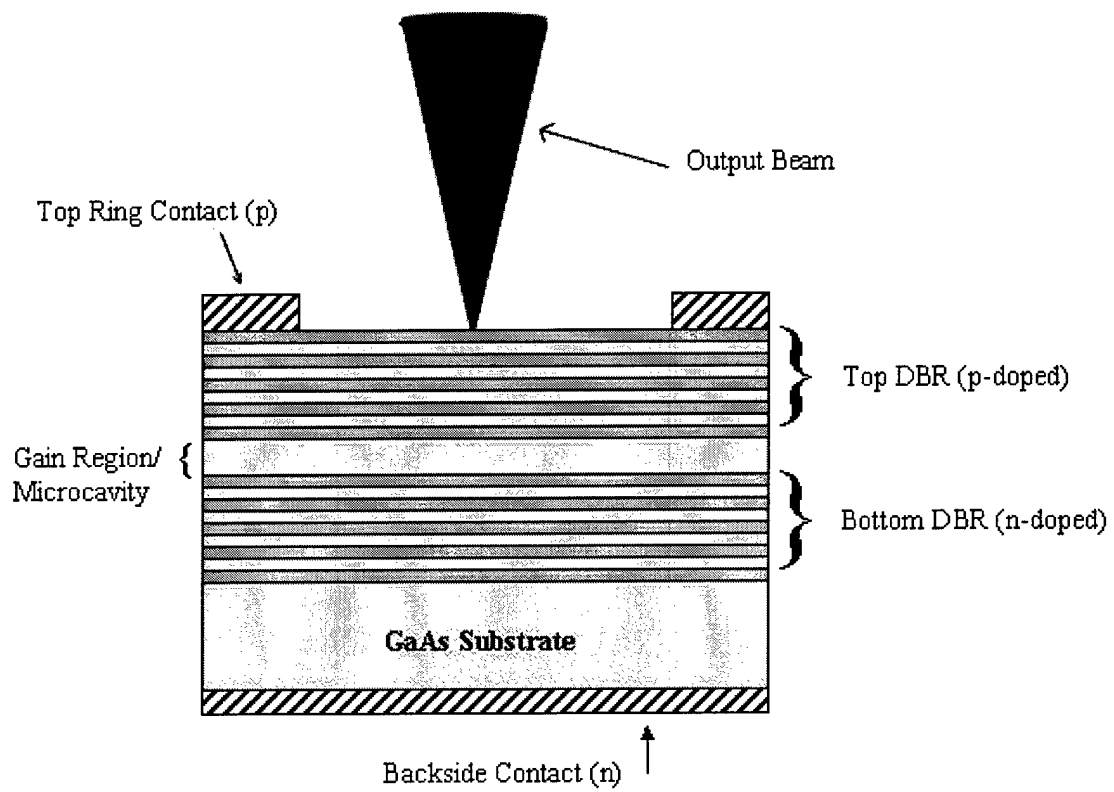


Figure 1.1 Schematic of a typical VCSEL structure

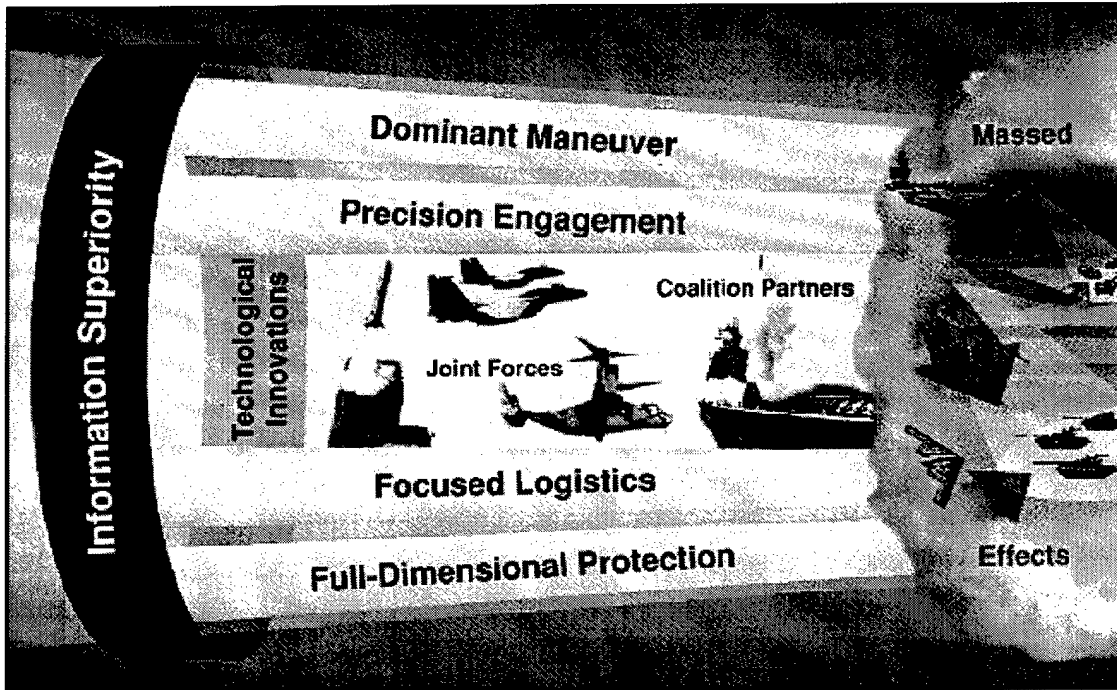


Figure 1.2 Importance of information superiority as related to Joint Vision 2010 [5].

1.2 Problem Statement

The evolving optoelectronic industry is today where the electronics industry was in the 1960's. Currently, only a relatively small number of devices can be integrated into a single package. Advances in VCSEL technology promise the very large scale integration (VLSI) of tens of thousands of optoelectronic devices on a single substrate. This large scale integration of devices will reduce power and processing requirements of signal and image processing systems by as much as 1000 times [36]. The monolithic integration of VCSEL devices with detector arrays allows for high-performance, three-dimensionally-based, optoelectronic signal processors for military battlefield information processing systems [36].

The formation of a robust native oxide (SiO_2) in silicon processing allowed for the growth and dense integration of silicon VLSI systems. The preferential attributes of SiO_2 are its high material density, low interface state density, mechanical stability, and robust insulating properties [27]. Researchers in III-V compound semiconductors such as gallium arsenide (GaAs) have been

pursuing a similar material for decades. An advantage of GaAs material is its high electron mobility. The juxtaposition of high electron mobility and the ability to grow monolithic lattice-matched material layers make GaAs an ideal substrate for the integration of high-speed photonic devices. Thorough research has been conducted on the addition of aluminum to GaAs to form the ternary compound aluminum gallium arsenide (AlGaAs) which is generally written as $Al_xGa_{1-x}As$, where $0.0 \leq x \leq 1.0$ represents the mole fraction of aluminum arsenide (AlAs) material contained in the compound. This compound can be grown over the entire compositional range of x on a GaAs substrate with a lattice mismatch of only 0.1 percent [47]. Oxides of Ga and As are unstable and difficult to control. It is therefore necessary to find an alternative to using oxides of Ga and As for the creation of large scale III-V systems.

Researchers at the University of Illinois discovered a phase of aluminum oxide (AlO) in contrast to Ga or As oxides, which exhibited mechanical stability and a low refractive index [11]. This new oxide has significantly impacted the development of optoelectronic devices. The oxide has been used extensively in index-guiding [28] and buried current aperture photonic or optoelectronic devices [38] and will be discussed further in Chapter 2. The selective oxidation of AlAs or $Al_xGa_{1-x}As$ layers within a VCSEL device (converting the AlAs or $Al_xGa_{1-x}As$ to AlO or AlGaO) is rapidly becoming the critical step by which to realize ultra low threshold laser operation.

Currently the optical parameters of AlAs after conversion to AlO are not well understood and this limits the ability of the Air Force Research Laboratory (AFRL) and other organizations to design, grow, and characterize highly efficient electro-optical micro-systems.

1.3 Thesis Scope and Approach

In this thesis I experimentally and theoretically investigate the optical and mechanical material properties of hydrolyzed aluminum oxide (henceforth called "native oxide") and I use this

acquired knowledge to recommend ways to optimize the performance of microcavity devices that contain native oxide layers.

I first perform detailed thin-film optical measurements on various semiconductor and native oxide distributed Bragg reflectors (DBRs) and related multilayer structures by analyzing data obtained through reflection and transmission experiments. This data is used to determine the optical properties of the aluminum oxide material and is fed into optical thin film models to analyze the effects of layer thickness and relative placement of layers on the overall performance of multilayer Fabry-Perot etalon and VCSEL devices. The VCSEL modeling includes calculation of transmittance, reflectance, absorbtance, and electric field intensity (i.e. standing wave pattern). Finally, initial efforts to characterize a selective aluminum oxide etchant for epitaxially grown microcavity structures are conducted and analyzed. These studies support the development of both integrated micro-optical devices and fabrication techniques for the realization of a III-V microelectromechanical systems (MEMS) technology.

1.4 Thesis Outline

In Chapter 2, I discuss relevant theoretical material and microcavity device information, VCSEL component structures, and relative material property parameters. In Chapter 3, I outline my numerical model formalism and simulation methods. I describe pertinent experimental equipment and procedures, and my design methodology in Chapter 4. Chapter 5 follows with the results obtained through experimental and theoretical modeling of devices and the analysis of these results. Chapter 6 contains my conclusions, a summary of my contributions and lessons learned, and my suggestions for further research.

2. Device Theory

2.1 Introduction

In this chapter I examine the history and background of microcavity device structures with a focus on vertical cavity surface emitting lasers (VCSELs). I explain the theory behind VCSEL operation and discuss how the selective conversion of AlAs layers to aluminum oxide (AlO) layers enhances the performance and reliability of VCSELs while simultaneously decreasing their manufacturing complexity. I conclude with an explanation of regression analysis techniques I used to analyze the optical properties of AlO layers via measurements on oxide containing microcavity structures.

2.2 Brief History of Microcavity Devices

The VCSEL, along with all other types of lasers, owes its genesis to the work of Albert Einstein and his concept of stimulated emission. Einstein built upon the work of Max Planck who postulated in 1900 that energy is transmitted in small, discrete units, which he called quanta [20]. Planck also theorized that the energy, E , of an incident photon could be quantified such that

$$E = h\nu \quad (\text{J}) \quad (2.1)$$

where h is Planck's constant and ν is the frequency of the photon.

This was a radical departure from Maxwell's generally accepted theory of the era that energy was transmitted in waves. Einstein's idea was that a photon of appropriate frequency could stimulate an excited atom to emit another identical photon thus causing stimulated emission. Einstein's ideas were realized in 1958 when American physicists Schawlow and Townes filed for the first laser patent [44]. Maiman demonstrated the first lasing action device in 1960. Work continued on semiconductor laser diodes throughout the next two decades. Hayashi and Panish from Bell

Laboratories designed the first semiconductor laser that operated in continuous wave (CW) mode at room temperature in 1971. The surface emitting laser structure that eventually led to the development of the VCSEL was then pioneered by Iga et al. in the late 1970's at the Tokyo Institute of Technology [24]. The 1980's saw improvements in the lifetime of semiconductor laser diodes, as well as a decrease in physical size.

Current VCSEL research is focused on the development of low threshold devices that operate in thermally abusive environments, have extended device lifetimes, and turn on with low threshold currents. VCSELs offer many advantages over the edge-emitting lasers (EEL) currently used in commercial systems such as compact disk (CD) and digital video disk (DVD) players. Figure 2.1 shows the change in optical cavity orientation between the VCSEL and EEL. The EEL emits light parallel to the surface of the wafer while the VCSEL's surface-normal orientation and circularly symmetric Gaussian beam are better suited for high coupling efficiency into an optical fiber. EEL's require extensive post-processing before the devices can be tested for functionality, whereas the VCSEL can be tested on-wafer. The VCSEL also naturally lends itself to array applications which include wavelength division multiplexing, local area networks, and high-speed optical interconnects. Large 2-D VCSEL arrays emitting at equally spaced wavelengths have been proposed and demonstrated [6]. Figure 2.1 also shows the dramatic size difference between the gain length in EELs ($100-1000\lambda$) and VCSELs (1λ), where λ is the emission wavelength. The small geometry of the VCSEL is ideally suited for high-density arrays since the devices require very small ($\sim 100\mu A$) operating currents.

2.3 VCSEL Device Theory

VCSEL devices are grown using molecular beam epitaxy (MBE) or metal-organic vapor phase epitaxy (MOVPE). Both methods offer the precise thickness control requirements necessary for lasing operation. Alternating layers of high and low index of refraction material are used to create

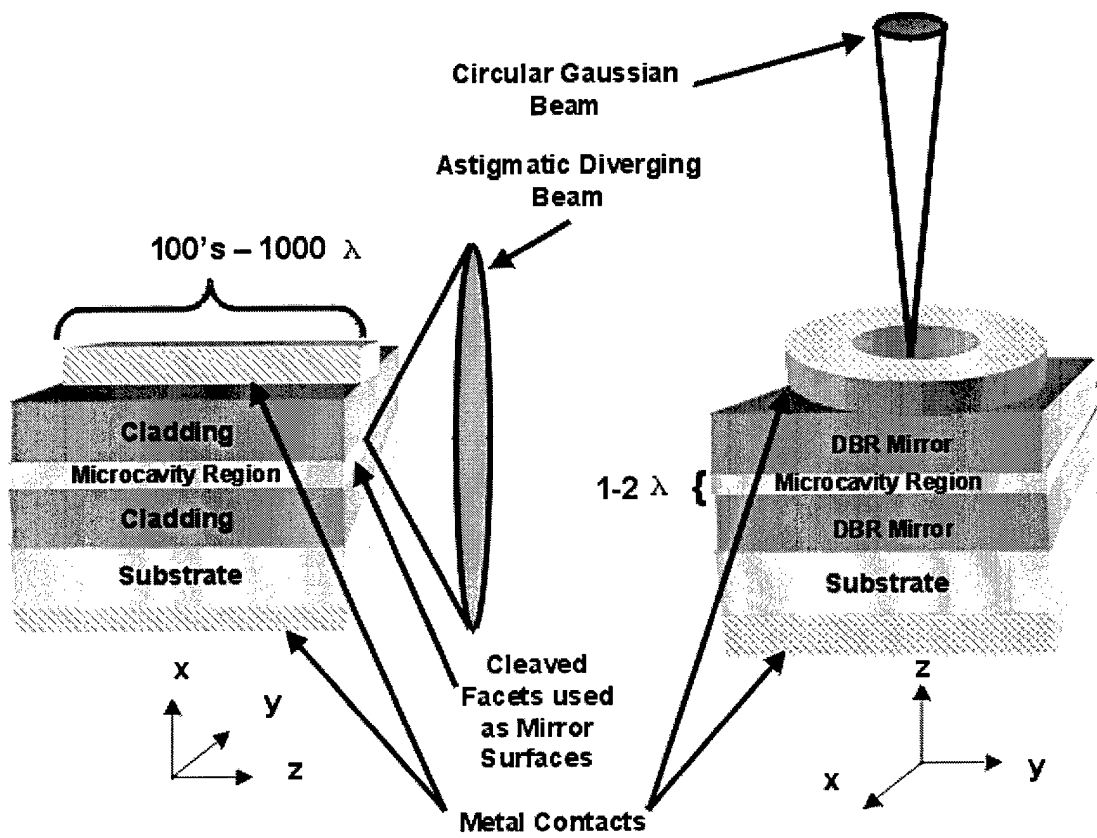


Figure 2.1 Comparison of emission orientation between; (a) edge emitting lasers (EELs) and (b) vertical cavity surface emitting lasers (VCSEL)

the high reflectivity mirrors, known as distributed Bragg reflectors (DBRs), necessary for the onset of lasing. A quantum well active region is placed inside the microcavity and will typically have a thickness of 40-100 Å. This thickness provides a single pass gain of less than 1%. In order to ensure that the cavity losses are less than the single pass gain, the mirror reflectivities must typically be greater than 99%. Figure 1.1 shows a typical VCSEL device structure consisting of a microcavity, or active region, and two coplanar reflective surfaces (mirrors). The DBR mirrors and microcavity region are designed to resonate light at a specific frequency known as the design or Bragg wavelength (λ_{Bragg}). The DBR mirror layers are designed as quarter-wave layers such that light propagating at λ_{Bragg} constructively interferes and leads to the onset of lasing. The physical thickness, d_l , of a quarter-wave DBR layer is

$$d_l = \lambda_{Bragg} / 4n_l \quad (nm) \quad (2.2)$$

where n_l is the complex wavelength-dependent index of refraction given by

$$n_l = n + i\kappa \quad (\text{unitless}) \quad (2.3)$$

where n is the real part of the index of refraction, κ is the imaginary part, and i is $\sqrt{-1}$. The parameter, n_l , can also be defined by

$$n_l \equiv \frac{c_o}{v_{phase}} \quad (\text{unitless}) \quad (2.4)$$

where c_o is the speed of light in a vacuum and v_{phase} is the phase velocity. The phase velocity is the speed of light in a medium with index n_l .

The real part of the index of refraction, n , is a measure of how much the velocity of the light is reduced upon entering a particular material. The imaginary part of the index of refraction, κ ,

is also known as the extinction coefficient. The extinction coefficient describes how absorptive a material is. If κ goes to zero, the light wave will not lose energy as it travels through the material and the material is then said to be transparent.

When photons of light are incident on an absorbing media, they are absorbed according to Beer's law given by

$$I = I_o e^{-\alpha x} \quad \left(\frac{W}{m^2} \right) \quad (2.5)$$

where I is the intensity of the observed light, I_o is the intensity of the incident light, x is the distance traveled, and α is the absorption coefficient given by

$$\alpha = \frac{4\pi\kappa}{\lambda_o} \quad (cm^{-1}) \quad (2.6)$$

where λ_o is the wavelength of the incident light in cm and κ is defined as

$$\kappa = \frac{\alpha\lambda_o}{4\pi} \quad (\text{unitless if } \alpha \text{ in } cm^{-1} \text{ and } \lambda \text{ in cm}) \quad (2.7)$$

It is important to note that both α and κ are dispersive quantities (functions of λ).

The optical microcavity of a VCSEL is designed such that it will resonate light at a specific wavelength, $\frac{\lambda_o}{n}$ or λ . In order to satisfy the resonance condition, the cavity length, L , must satisfy

$$nL = m \frac{\lambda}{2} \quad (\mu m \text{ if } \lambda \text{ in } \mu m) \quad (2.8)$$

where L is the length of the cavity and m is a positive integer.

VCSEL structures incorporate DBR mirror pairs that are designed to be highly reflective over a range of wavelengths. The wavelength range over which the device is highly reflective is known as the stop band, $\Delta\lambda_{stopband}$, and is given by [52]

$$\Delta\lambda_{stopband} \approx \frac{2\lambda_{Bragg}\Delta n}{\pi n_{eff}} \quad (\text{nm}) \quad (2.9)$$

where Δn is the absolute value of the difference in the real refractive index of the high and low layers ($|n_{high} - n_{low}|$) and n_{eff} is defined as the effective refractive index of the medium such that

$$n_{eff} = \frac{2}{\frac{1}{n_{high}} + \frac{1}{n_{low}}} \quad (\text{unitless}) \quad (2.10)$$

Figure 2.2 shows constructive interference resulting from a DBR designed at λ_{Bragg} and comprised of alternating high- and low-index quarter-wave layers.

The overall power reflectance of a DBR stack increases as a function of the number of high-low pairs and as a function of the difference in refractive index between the high and low index layers. Figure 2.3 shows the calculated power reflectance for a DBR structure constructed of GaAs (high) and AlAs (low) quarter-wave layers, designed at λ_{Bragg} equal to 700nm and on a GaAs substrate, as a function of the number of high/low pairs, N_p , for normally incident light at 700nm. The figure shows that to achieve a power reflectance of 0.99 (99%) the DBR structure must contain 12 pairs of alternating high- and low-index material. The reflectance values are calculated using the standard 2×2 matrix approach using MATLAB code developed at the Air Force Institute of Technology (AFIT) [37] [41].

Semiconductor diode lasers, as well as all other lasers, work on the principle of stimulated emission. I now briefly examine stimulated emission, spontaneous emission, and absorption as they apply to VCSEL devices. Recombination events inside a semiconductor material can be either radiative or non-radiative. Non-radiative recombination disperses energy from the annihilation of

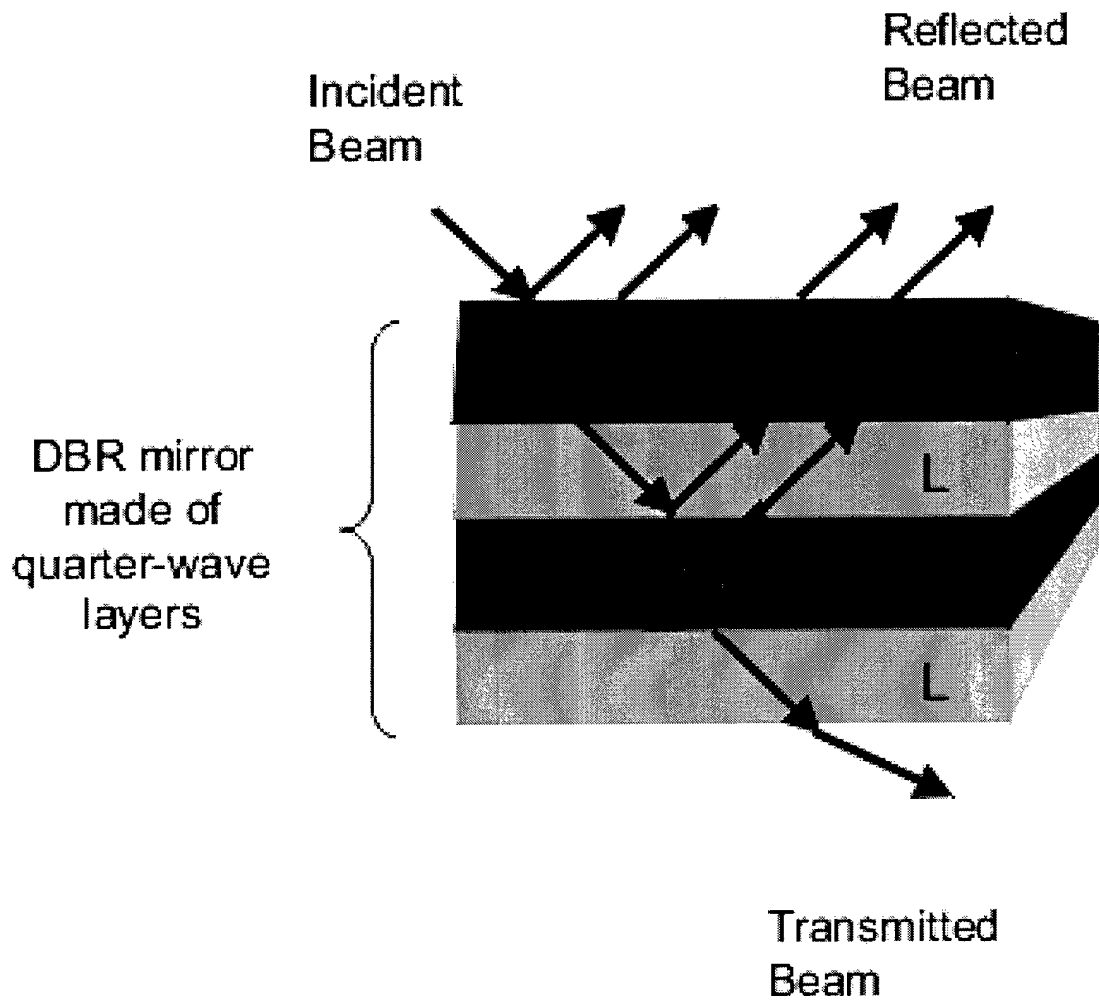


Figure 2.2 Distributed Bragg Reflector (DBR) using alternating high- and low-index layers [3].

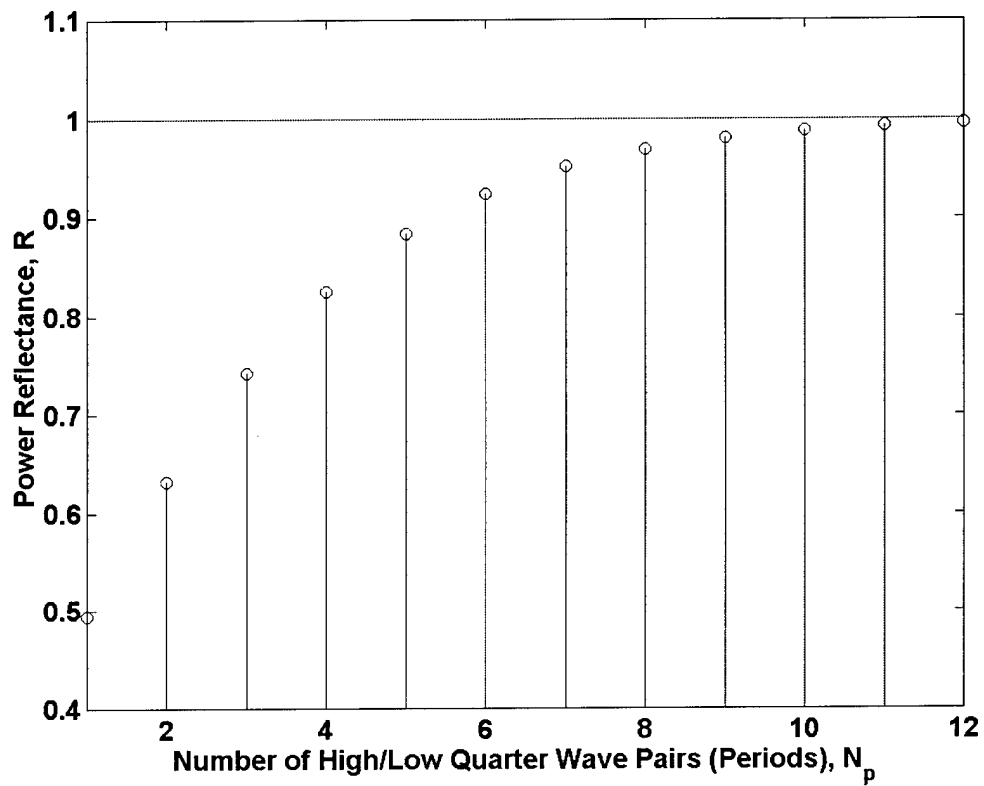


Figure 2.3 Power reflectance as a function of number of quarter-wave pairs (N_p) for a DBR structure (GaAs and AlAs quarter-wave layers) on a GaAs substrate designed for λ_{Bragg} equal to 700nm for normally incident light.

an electron in the form of lattice vibrations. Lattice vibrations of this nature are also known as phonons. Energy stored in the form of phonons is then converted into heat and dissipated from the structure through the surrounding material. If a semiconductor material is illuminated with light of energy greater than the band gap energy, E_g , it will absorb the light. This absorption process excites electrons from the valence band to the conduction band. The transition process creates a hole in the valence band. The electron will eventually return to the valence band after a certain period of time and emit a photon of wavelength λ . The wavelength of the emitted photon will be related to E_g by [43]

$$\lambda = \frac{hc}{E_g} \approx \frac{1.24}{E_g} \quad (\mu m \text{ if } E_g \text{ in eV}) \quad (2.11)$$

This process is known as spontaneous emission. A non-equilibrium state is created when energy is imparted to the system. This energy obtained from incident photons or by injecting minority carriers into the active region may create a population inversion within the device. The state of population inversion implies that there are more electrons in the conduction band than in the valence band. The high concentration of carriers in the conduction band allows for the process of stimulated emission to begin. A photon with wavelength λ incident on the non-equilibrium semiconductor will stimulate emission of another photon with wavelength λ . The interaction will result in a synchronized vibration of a dipole that is formed by the polarization of an atom under light incidence with the frequency of the emitted light. The semiconductor band-to-band recombination processes are shown in Figure 2.4 [43].

The operation of a VCSEL can be broken into the processes shown in Figure 2.4. The flow of carriers into the active region generates photons as a byproduct of recombination. Photons are then transmitted out of the optical cavity [52]. Charles Fabry and Alfred Perot developed an optical resonator for use as an interferometer [43]. A VCSEL device utilizes this type of Fabry-Perot (FP) etalon structure to select the wavelengths that will be transmitted. Typical VCSEL designs

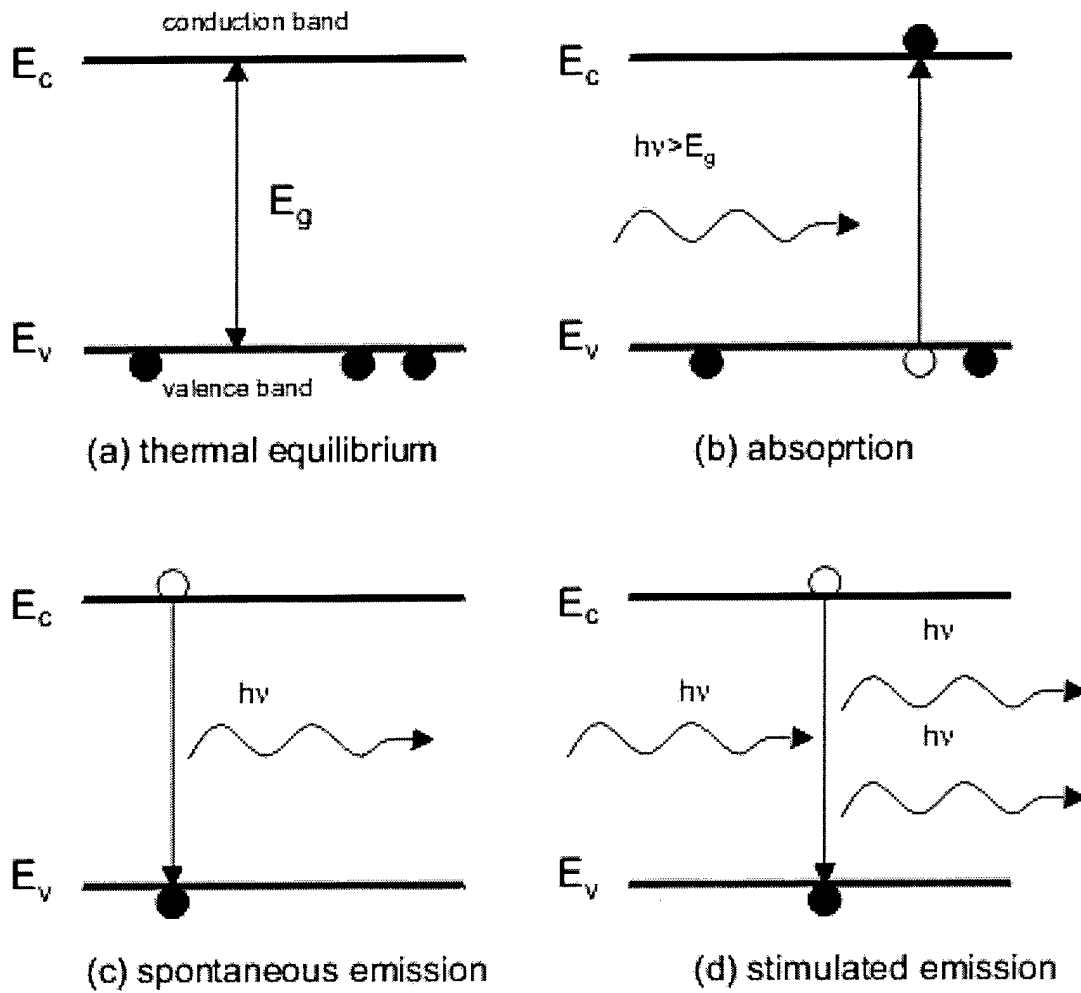


Figure 2.4 Semiconductor band-to-band recombination processes [43].

use a microcavity utilizing one or multiple quantum wells (QW) for their active region. Carriers are generated within the microcavity region through an applied electric field or by pumping the device optically. This excitation causes electrons to jump from the conduction band to the valence band. As the electron moves from the conduction band to the valence band it emits a photon whose wavelength corresponds roughly to the energy gap of the QW material. The photon then makes multiple passes through the microcavity region and induces similar band-to-band transitions. The direction and phase of the emitted photon is coherent with the one that initially caused the transition. The lasing process then proceeds. VCSEL devices can be designed to transmit light out of both the top and the bottom of the structure depending on fabrication steps taken to prohibit light transmission.

The output light from a VCSEL device is selected by creating an etalon structure which transmits the desired wavelength that corresponds to the location of the Fabry-Perot dip in the reflectance spectrum. An example of the calculated power reflectance spectrum and Fabry-Perot dip for a VCSEL is presented in Figure 2.5. The VCSEL depicted in Figure 2.5 consists of DBR mirrors created using GaAs and AlAs layers. The microcavity for the device is optically 1.5λ long and is designed to emit light at a wavelength of λ_{Bragg} equal to 980nm.

2.4 Oxide Layers in Microcavity Devices

2.4.1 Advantages of Oxide Layers in Optoelectronic Devices. The first attempt of wet oxidation of AlAs films was reported in 1979. The subsequent decade of research focused on aluminum containing semiconductor materials (e.g. AlGaAs, AlInAs, AlInGaP, etc.) and it was found that oxidation of these materials above 300°C produced a mechanically stable oxide. This oxide also had the benefit of reduced index of refraction [11]. Devices that incorporate a buried oxide confinement aperture under a dielectric DBR have displayed record low threshold current [53] and voltage [9] as well as record high power conversion efficiency [31].

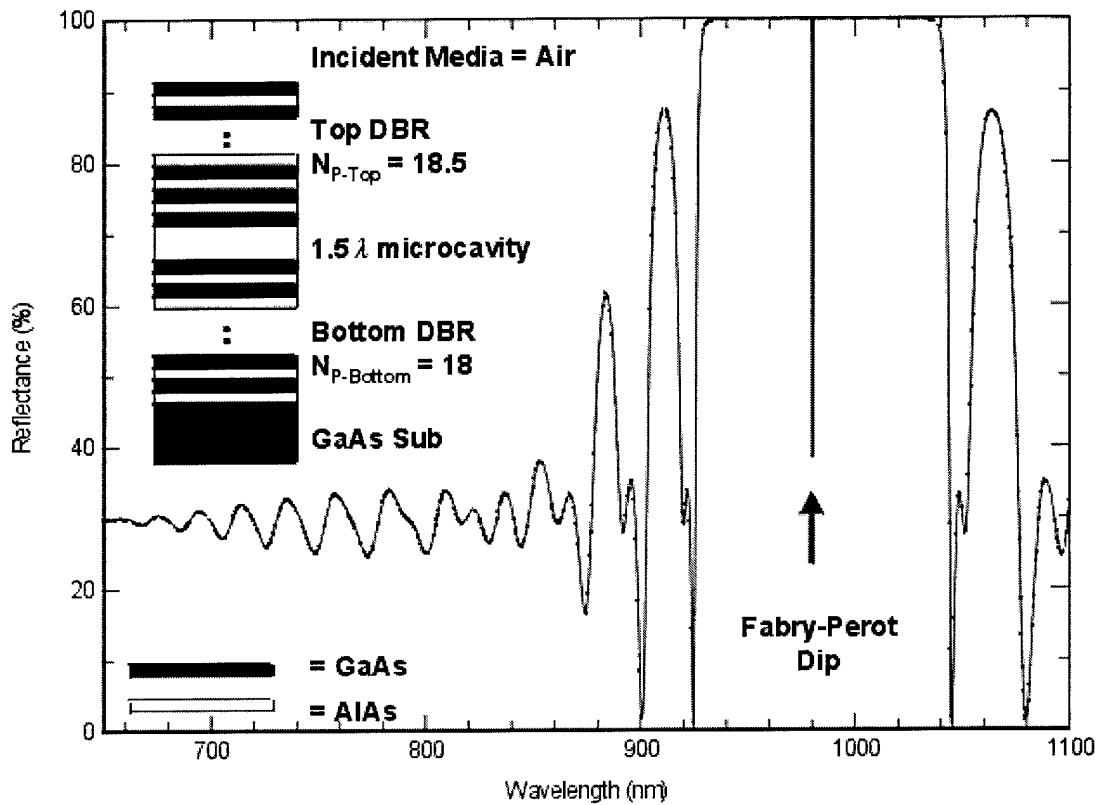


Figure 2.5 Calculated power reflectance spectrum for a 980nm etalon structure composed of alternating layers of GaAs and AlAs on a GaAs substrate containing a 1.5λ microcavity composed of AlAs; $N_{P-Top} = 18.5$ and $N_{P-Bottom} = 18$.

Equation 2.9 defines the width of the stop band for a VCSEL device. It is obvious that by increasing Δn while decreasing n_{eff} , the stop band of the device can be increased. This effect is clearly demonstrated in Figure 2.6 where the high reflectance stop band of the oxide mirror device (GaAs/AlO DBR mirror layers and a 1λ AlO cavity) is achieved using only 2 high/low layer pairs on the bottom DBR mirror and 2.5 high/low layer pairs on the top DBR mirror. The high reflectivity bandwidth is much larger than a similar GaAs/AlAs (GaAs/AlAs DBR mirror layers and a $1-\lambda$ thick AlAs cavity) device which requires 12 high/low layer pairs on the bottom DBR and 12.5 high/low layer pairs on the top DBR. Both devices have $\lambda_{Bragg} = 900$ nm.

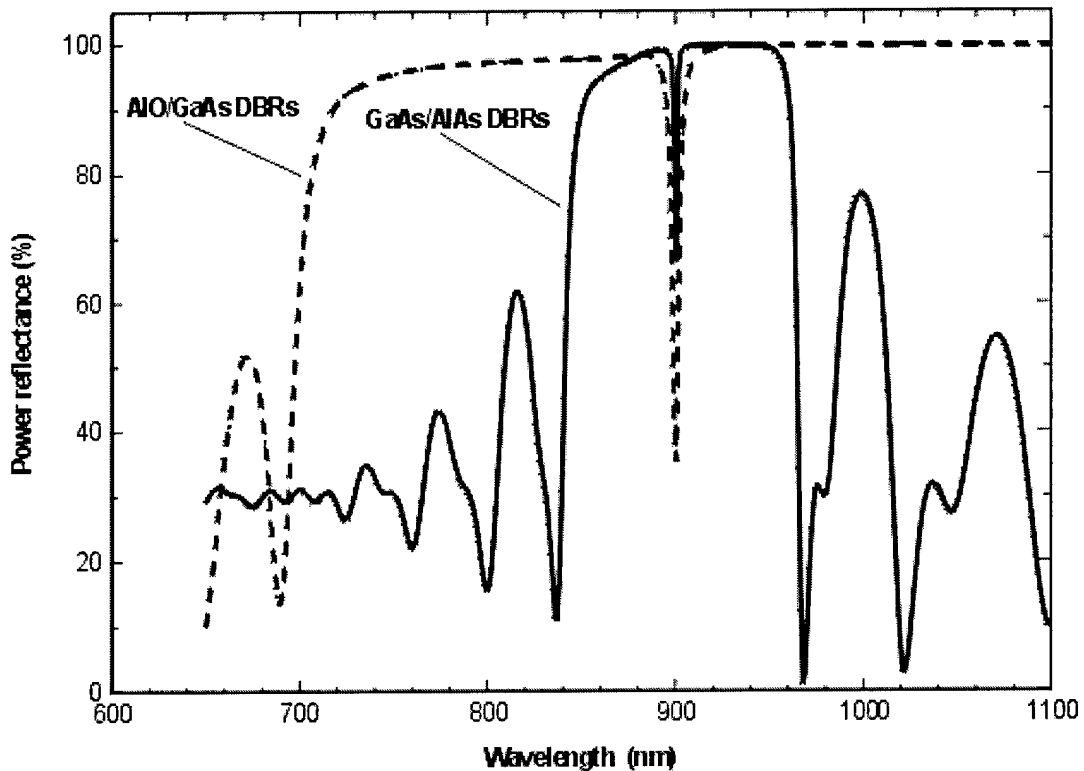


Figure 2.6 Comparison of power reflectance for etalon structures composed of GaAs/AlAs DBRs (solid line) and GaAs/AlO DBRs (dashed line)

Smaller VCSEL geometries lead to devices that operate with lower threshold currents. The small geometry device is much more susceptible to optical losses that occur as a result of diffraction of light out of the waveguided region and through the guiding of light into higher order transverse

and radiation modes from the dielectric aperture or etched air post [49]. If the losses from these mechanisms become too significant, the threshold gain for the device may become too large for the quantum well gain layers to compensate. This condition results in a device that cannot provide enough gain and the VCSEL will function only as a light emitting diode (LED). Studies have shown that the losses from dielectrically apertured devices are less than those experienced in an etched air post device [49]. Figure 2.7 shows the modal guiding and scattering for an oxide-apertured VCSEL and an etched air post VCSEL.

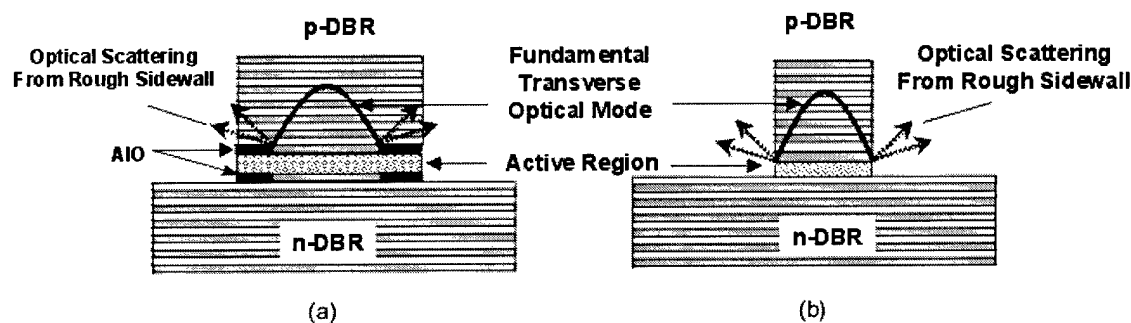
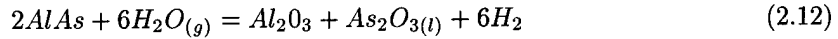


Figure 2.7 Comparison of optical losses for small geometry VCSEL devices: (a) oxide-apertured device (b) etched air post device, after [52].

2.4.2 Oxide Growth Kinetics. The conversion of AlAs (or AlGaAs) semiconductor material to AlO (or AlGaO) through the process of oxidation, is performed by introducing water vapor via inert gas transportation at an elevated temperature to an exposed AlAs (or AlGaAs) surface. The oxidation state of the AlAs is made more positive through the oxidation process [8]. Steam transported to the sample in the form of water vapor is already in the -2 oxidation state. The oxidation state of an atom of an element in a compound is the difference between the number of electrons an atom of that element has and the number of electrons an atom of the element has in the particular compound. The agent for removing electrons from the AlAs (or AlGaAs) material is the H^+ (i.e. H^+ has an oxidation state of +1) from the water vapor source. A simplified example of a possible oxidizing process that occurs in an AlAs semiconductor layer is [30]



As previously discussed, a distinct advantage of using DBR structures that contain converted oxide layers is the reduction in the number of H-L quarter-wave pairs needed for high reflectance mirrors. Figure 2.8 shows the effect on DBR power reflectance of converting high aluminum content AIAs layers to AlO via the thermal oxidation process. A reduction in the number of required DBR mirror pairs, N_p , increases manufacturability of VCSEL devices by decreasing the complexity of the structure while simultaneously decreasing the amount of time needed to grow the device. A drawback to this technique is the amount of time needed to oxidize the device. Oxidation time varies as a function of VCSEL mesa diameter and desired oxide aperture diameter.

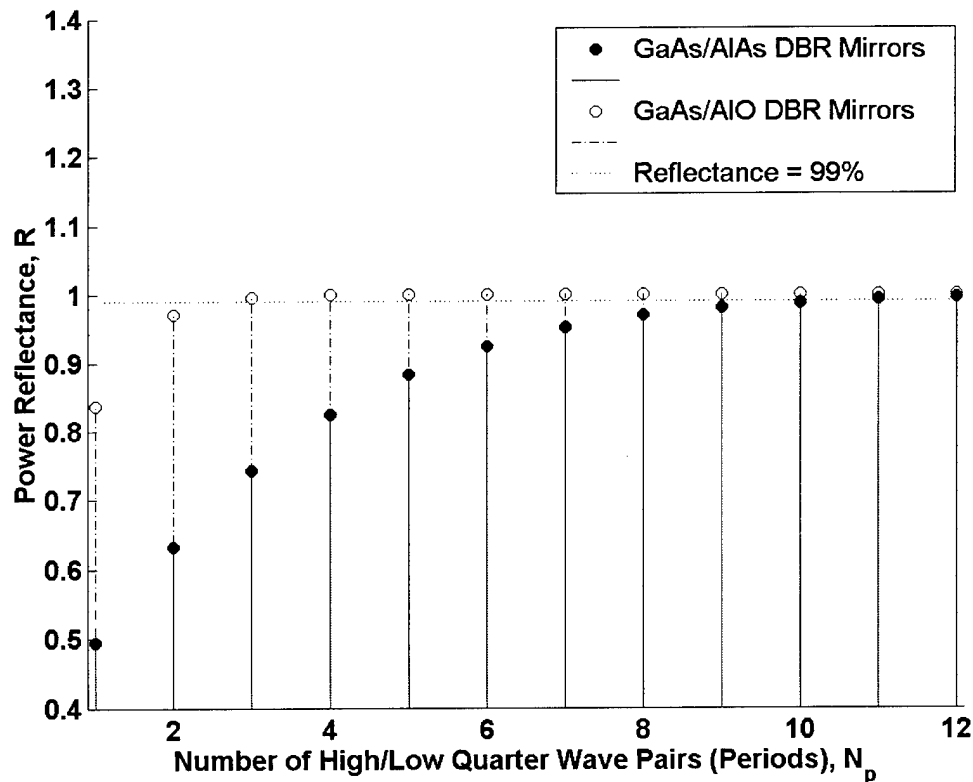


Figure 2.8 Comparison of the number of high/low quarter-wave pairs (periods), N_p , needed to achieve 99% power reflectance (structure designed for λ_{Bragg} of 700nm).

Early oxidation studies were reported as successful [8]. Further work, however, must be completed in order to ensure that the process is controllable and reproducible. Initial efforts in oxidation of AlAs films were performed at a low ambient temperature ($\sim 100^\circ\text{C}$). Retention of arsenic-oxide compounds at this low temperature resulted in a net volume expansion of the converted layer [50]. Oxidations performed at higher temperatures ($\sim 450^\circ\text{C}$) result in an overall volumetric contraction of the converted layer due to As depletion [11].

A schematic of an oxide confined VCSEL structure is shown in Figure 2.9. The figure shows a VCSEL with two native oxide "current apertures." The aperture layers are placed directly above and below the microcavity region. This placement provides index guiding as well as current confinement for low-threshold operation. The restriction of current flow through the oxide apertures is shown in Figure 2.9. The use of oxide layers as current apertures greatly improves device efficiency since almost all of the injected current contributes to light generation within the apertures. A small portion of the AlGaAs DBR layers is also oxidized (with a much slower rate than AlAs). Figure 2.10 shows the reduction in threshold current, I_{th} , and threshold current density, J_{th} , as a function of the radius of the oxide aperture. Figure 2.10 also shows the change in lasing wavelength, λ_{th} , as the aperture width is decreased.

The standard oxidation model for conversion of AlAs to AlO is in the form of the Deal-Grove Model [12]

$$\frac{d_{ox}^2 - d_i^2}{B} + \frac{d_{ox} - d_i}{\frac{B}{A}} = \Delta t \quad (2.13)$$

where d_{ox} is oxide thickness (μm), d_i is initial oxide thickness (μm), Δt is oxidation time, A and B are temperature-dependent fitting parameters of the form [19]

$$A(T) = A_o e^{-\frac{E_a A}{kT}}, \text{ and } B(T) = B_o e^{-\frac{E_a B}{kT}} \quad (2.14)$$

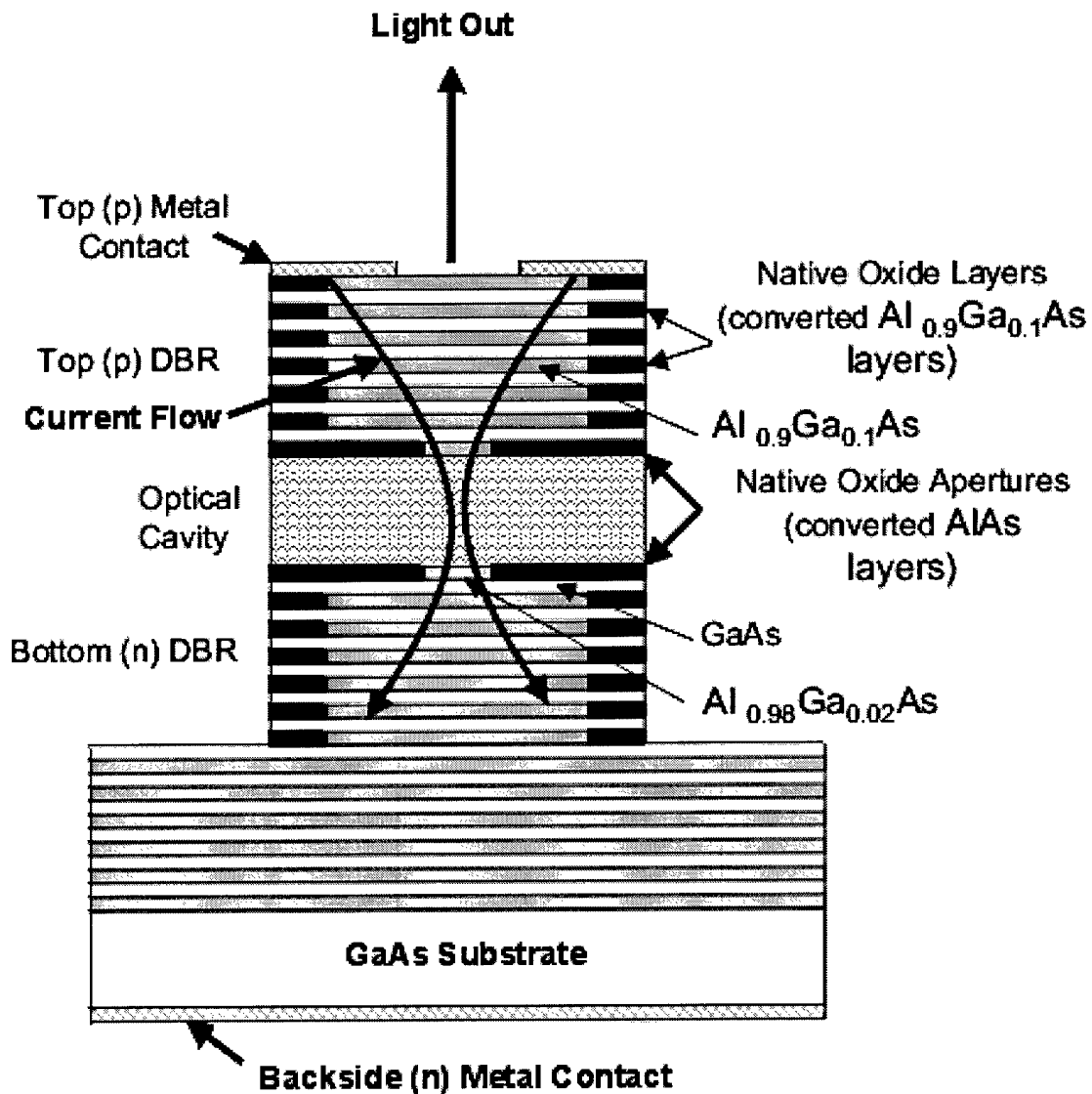


Figure 2.9 Monolithically grown oxide-aperture VCSEL device schematic after oxidation [52].

The figure demonstrates how increased oxidation rate of $Al_{0.98}Ga_{0.02}As$ forms a current confinement layer directly above and below the optical cavity of the device. The DBR mirror layers are composed of $Al_{0.9}Ga_{0.1}As$. These layers will oxidize to some extent. This reduction in index provides for index guiding within the structure while still allowing current to flow through the DBR structures. This type of device has been used to achieve ultra-low threshold VCSELs.

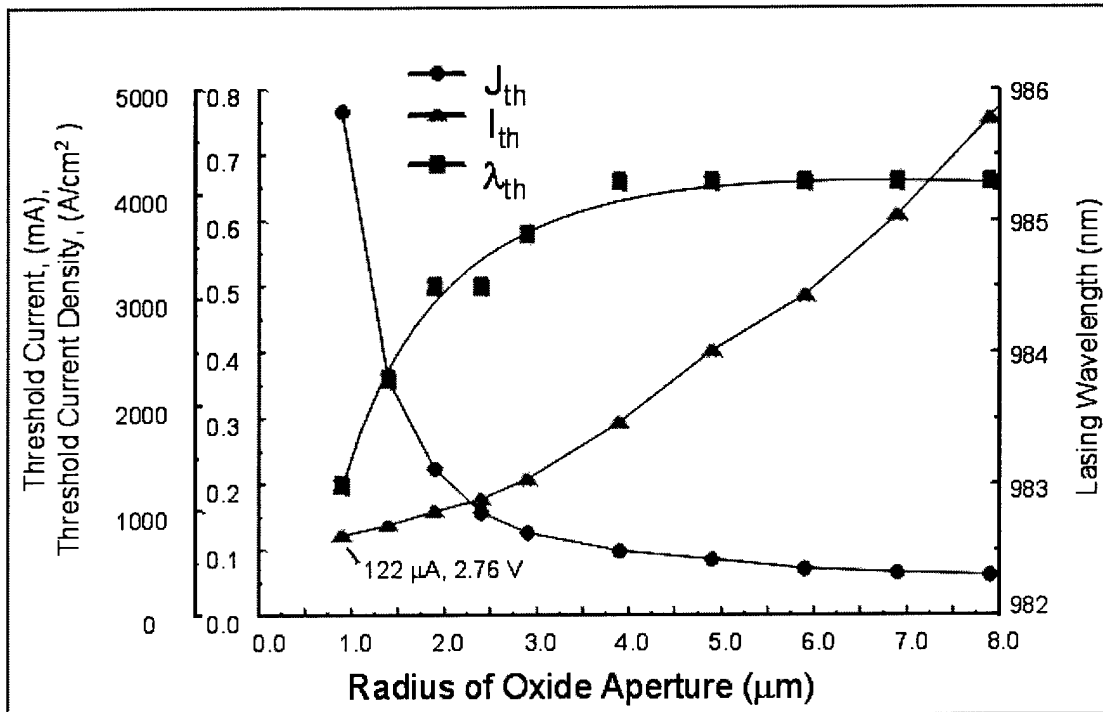


Figure 2.10 Threshold current and threshold current density for an oxide-confined VCSEL device as a function of oxide aperture radius [18].

k is Boltzmann's constant, and T is temperature in Kelvin. E_{aA} and E_{aB} are activation energies which relate the amount of energy needed to produce a chemical reaction for a given temperature.

Data was collected on several samples processed at AFRL in their custom-designed oxidation system (the system is discussed in detail in Chapter 4 and is shown in Figure 4.9). A nonlinear least-squares fit of the oxidation data yields [19]: $A_o = 7.86 \times 10^{-6}$ (μm); $B_o = 1.07 \times 10^8$ ($\mu\text{m}^2\text{-min}$); $E_{aA} = -0.846$ (eV); and $E_{aB} = 0.912$ (eV).

Figure 2.11 shows the temperature- and aluminum mole fraction-dependence of the oxidation rate. Figure 2.11a shows the strong compositional dependence of the oxidation rate on the mole fraction of AlAs contained within a material. The oxidation rate experiences a growth increase of greater than 2 orders of magnitude as x is increased from 0.84 to 1.0. Figure 2.11b shows the influence of layer thickness on the rate of oxidation. Layer thicknesses greater than 60 nm exhibit a near constant oxidation rate while layers thinner than ~ 50 nm experience a notable decrease in oxidation rate with layer thickness. Figure 2.11c displays the oxidation rate dependence on temperature. An increase in temperature exponentially increases the oxidation rate for a given AlAs mole fraction. This implies that the lateral oxidation rate of $\text{Al}_x\text{Ga}_{1-x}\text{As}$ is reaction rate limited, or limited by the arrival rate of the oxidizing agent. This differs from a reaction that is limited by the diffusion of the reactant species through the oxide to the reaction interface [52]. Figure 2.11d shows experimental data collected at AFRL which illustrates the oxidation rate dependence on oxidation temperature.

2.5 Regression Analysis

Research efforts often require fitting model parameters to the collected data. I am interested in extracting the refractive index values of AlO layers from power reflectance measurements of AlO-containing multi-layer DBR microcavity structures. A popular technique for fitting is to minimize the sum-of-squares errors through the use of the Levenberg-Marquardt (LM) algorithm [4]. Herein

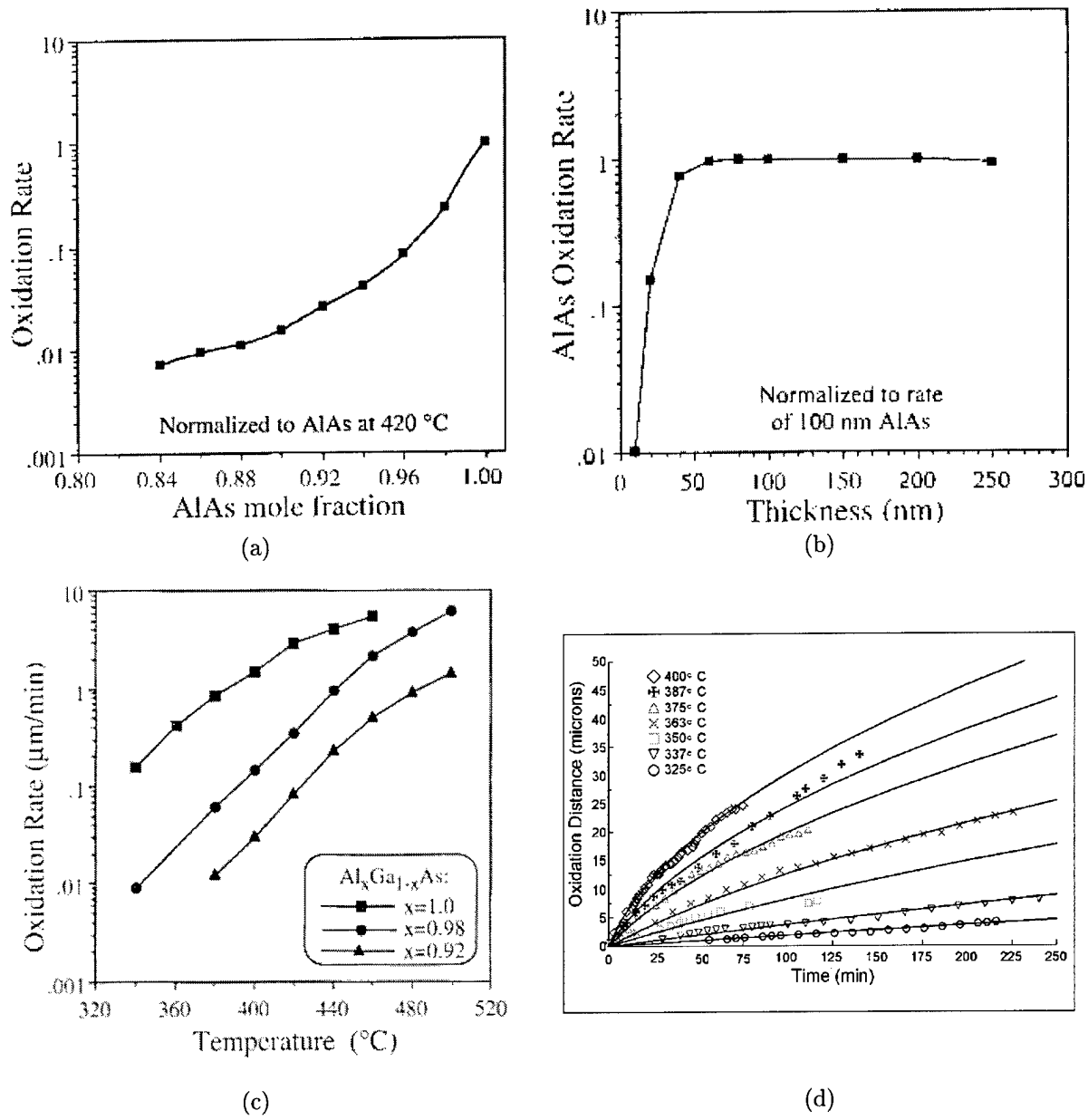


Figure 2.11 Al mole fraction and temperature-dependence of oxidation rate; a) mole fraction dependence of oxidation rate for AlGaAs @ 420 °C [52]; b) oxidation rate dependence on oxidizing layer thickness [52] shown for AlAs layer; c) oxidation rate vs. temperature for various $\text{Al}_x\text{Ga}_{1-x}\text{As}$ layers [52]; d) lateral oxidation distance as a function of time for an AlAs test structure various temperatures [19]

I discuss the LM algorithm and show how the modified LM algorithm can be efficiently used to minimize the sum-of-squares error between model parameters and collected data. The LM algorithm is used to perform regression analysis on collected data to fit model parameters to the physical parameters of a structure. The fitting routines are used to extract physical layer thickness values from collected data. The physical layer thickness values are then used to determine the optical parameters of the structure.

The sum-of-squares error is given by [4]

$$E = \frac{1}{2} \sum_n (\epsilon^n)^2 = \frac{1}{2} \|\epsilon\|^2 \quad (\text{unitless}) \quad (2.15)$$

where ϵ^n is the error for the n^{th} pattern and ϵ is a vector with elements ϵ^n .

If there is a point in weight space defined as w_{old} , the next move is to another point in that same space defined as w_{new} . Each measured data point, or feature, corresponds to a point in feature space. In my experiments, the two axes of feature space correspond to wavelength and power reflectance at that particular wavelength. These features can be placed into a vector r . Weight space is defined by a vector whose points all satisfy the following equation

$$w \cdot r = 0 \quad (2.16)$$

If the displacement between w_{old} and w_{new} is small then the error vector ϵ can be expanded into a first order Taylor series given by [4]

$$\epsilon(w_{new}) = \epsilon(w_{old}) + Z((w_{new}) - (w_{old})) \quad (2.17)$$

where the matrix Z is defined as

$$(Z_{ni}) \equiv \frac{\partial \epsilon^n}{\partial w_i} \quad (2.18)$$

where n and i are used to define the individual matrix elements in Z .

The sum-of-squares error function can then be written as

$$E = \frac{1}{2} \| \epsilon(w_{old}) + Z(w_{new} - w_{old}) \|^2 \quad (2.19)$$

to minimize this error with respect to the new weights, w_{new} becomes [4]

$$w_{new} = w_{old} - (Z^T Z)^{-1} Z^T \epsilon(w_{old}) \quad (2.20)$$

The elements of the Hessian matrix for the sum-of-squares error function takes the form [4]

$$(H)_{ik} = \frac{\partial^2 E}{\partial w_i \partial w_k} = \sum_n \left[\frac{\partial \epsilon^n}{\partial w_i} \frac{\partial \epsilon^n}{\partial w_k} + \epsilon^n \frac{\partial^2 \epsilon^n}{\partial w_i \partial w_k} \right] \quad (2.21)$$

By neglecting the second term in Equation 2.21, an approximation for the Hessian matrix can be written as

$$H = Z^T Z \quad (2.22)$$

For nonlinear networks, Equation 2.22 is exact at the global minimum of the error function. The approximation to the Hessian matrix is relatively simple to calculate by using back-propagation techniques to calculate first derivatives with respect to network weights [4].

The Levenberg-Marquardt algorithm seeks to minimize the error function while keeping the step size $w_{new} - w_{old}$ small enough to ensure the validity of a linear approximation [32].

The Levenberg-Marquardt algorithm addresses the problem of minimizing the sum-of-squares error by using a modified error function of the form [39]

$$E^* = \frac{1}{2} \| \epsilon(w_{old}) + Z(w_{new} - w_{old}) \|^2 + \xi \| w_{new} - w_{old} \|^2 \quad (2.23)$$

where the parameter ξ modulates the step size.

Next, to minimize the modified error function with respect to w_{new} , w_{new} becomes

$$w_{new} = w_{old} - (Z^T Z + \xi I)^{-1} Z^T \epsilon(w_{old}) \quad (2.24)$$

where I is the unity matrix. An initial value for ξ is chosen and is then varied throughout the optimization process. The modified sum-of-squares error is monitored after each iteration in the process. If the value of the sum-of-squares error is decreased, the value for ξ is also decreased (typically by a factor of 10 [4]). If the sum-of-squares error is increased at the next iteration, the value for ξ is likewise increased. The weight factors are adjusted at each step in the process until the overall value for the sum-of-squares error is decreased. The user can specify the value for the change in the sum-of-squares error to which the process is deemed insensitive to change and thus the algorithm iteration is terminated.

2.6 Chapter 2 Summary

In Chapter 2 I reviewed background and theoretical information on oxidation and microcavity devices, focusing on VCSELs. The optical properties of multilayer Fabry-Perot etalon structures were discussed along with the material properties of AlAs layers converted to AlO. A brief introduction to the Levenberg-Marquardt algorithm was also given to facilitate understanding of the method I used to extract material values from measured data, using theoretical values as a baseline. In Chapter 3 I first present my modeling formalism. I use my models to simulate the performance of

selected multilayer DBR and etalon structures. With the goal of learning more about AIO materials applied to multilayer structures, I then use my modeling tools to design multilayer test structures.

3. Modeling, Simulation, and Design

3.1 Introduction

In this chapter, I discuss my modeling, simulation, and design of microcavity structures containing selectively oxidized AlO layers. I describe the mathematical formalism and give example simulation results. Next, I use my models to design test structures for the purpose of analyzing microcavity devices. I developed and used several modeling tools to simulate the performance of the optical devices prior to their growth by molecular beam epitaxy (MBE) growth and as part of the post-processing analysis. A custom designed *MATLAB*[®] toolbox was created to calculate power reflectance values of several device structures [41]. A commercial package called *FilmWizard*[®] [45] was also used to calculate power reflectance, transmittance, and absorptance as well as to fit measured data to the theoretical model (as discussed in Chapter 2). Finally in this chapter I examine how I used my modeling and simulation tools to design the microcavity test structures from which I extract the optical material parameters of selectively oxidized AlO layers.

3.2 Reflectance, Transmittance, and Absorptance Calculations

Layer structures were designed using *FilmWizard*[®] and *MATLAB*[®]. Index values for GaAs, AlAs, and $Al_xGa_{1-x}As$ were taken from several sources [1] [25] [15]. The values for n and k were fed into the computer models in order to determine the expected reflectance, transmittance, and absorptance spectrum for each structure prior to epitaxial growth of the actual structures. Reflectance, transmittance, and absorptance are related by

$$R + T + A = 1.0 \quad (\text{unitless}) \quad (3.1)$$

where R is the amount of optical power reflected by the structure, T is the amount of optical power that is transmitted through the structure and A is the amount of optical power absorbed by the structure.

A full description of the matrix method for calculating power reflectance, transmittance, and absorptance is found in literature [54]. To demonstrate the matrix method for the calculation of power reflectance I evaluate a distributed Bragg reflector (DBR) structure consisting of alternating high and low quarter-wave layers with optical thickness [54]

$$n_1 d_1 = n_2 d_2 = \frac{1}{4} \lambda_{Bragg} \quad (3.2)$$

where n_1 and n_2 are the real refractive indices and d_1 and d_2 are the physical layer thicknesses. If n_o is the refractive index of the incident medium and n_s is the index of the substrate material, the reflectance at normal incidence can be found using [54]

$$R = \left[\frac{1 - \left(\frac{n_s}{n_o}\right) \left(\frac{n_1}{n_2}\right)^{2N}}{1 + \left(\frac{n_s}{n_o}\right) \left(\frac{n_1}{n_2}\right)^{2N}} \right]^2 \quad (3.3)$$

where N is the number of high-low quarter-wave pairs (periods) in the structure.

Several MBE calibration runs were required to adjust growth parameters until target thicknesses could be accurately grown. The first calibration growth is shown below in Table 3.1

Table 3.1 GaAs/AlAs Fabry-Perot Etalon (Sample G2-2651)

Layer (Starting at Sub)	Doping	Thickness (Å)	Note
GaAs	(u)	∞	Substrate
AlAs	Si	837	Bottom DBR
GaAs	Si	696	Repeat 12 Times
AlAs	(u)	10053	3 λ microcavity @ 980nm
GaAs	C	696	Top DBR
AlAs	C	837	Repeat 10 Times
GaAs	C	696	Extra $\frac{1}{4}$ λ layer

Reflectance, transmittance, and absorptance calculations as a function of wavelength and at normal incidence are shown in Figure 3.1, Figure 3.2, and Figure 3.3 respectively. For sample *G2 - 2651* the Fabry-Perot dip is clearly seen at 980 nm in Figure 3.1.

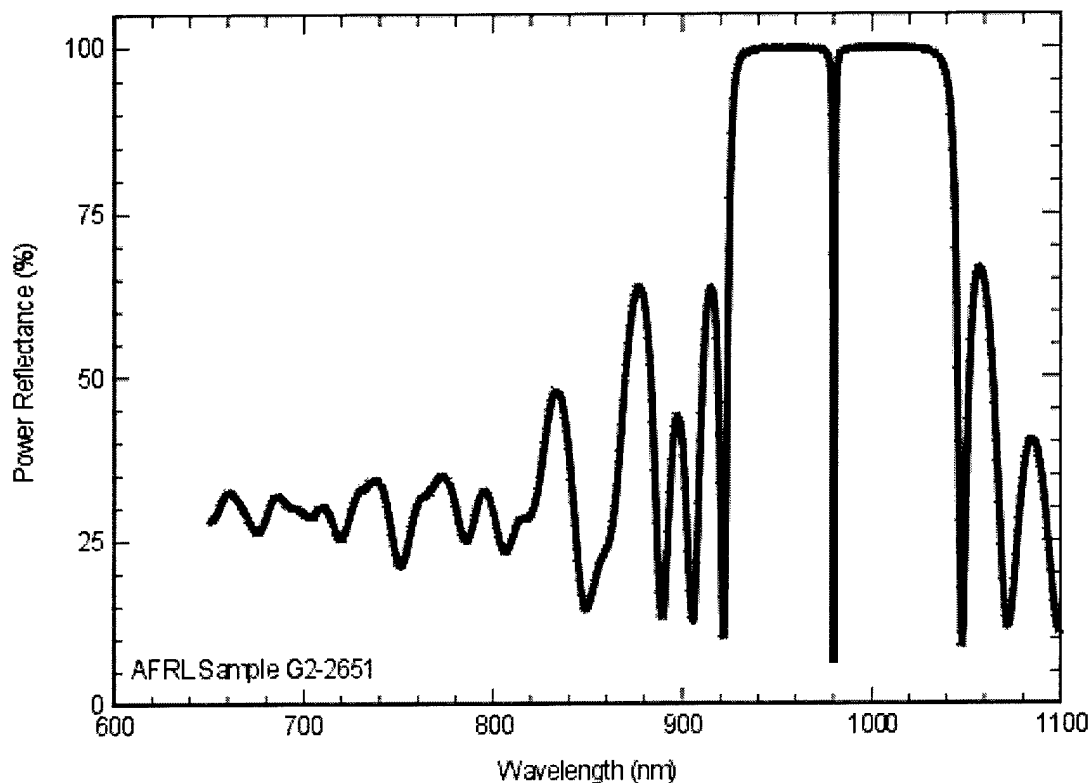


Figure 3.1 Calculated power reflectance spectra for AFRL sample *G2 - 2651* (normal incidence).

The standing wave pattern of the electric field intensity within a structure can also be calculated [54]. It has been shown that the optimal position to place an oxidized layer is at the standing wave null (or node) of the electric field intensity inside the structure [40]. This concept is explored further in Chapter 4. An example of the standing wave pattern within sample *G2 - 2651* is shown in Figure 3.4.

The models were used to examine power reflectance dependence on layer thickness values. The MBE calibration runs were designed to place particular emphasis on certain material layer structures so that proper growth rates could be determined. For example, the structure in Table 3.1

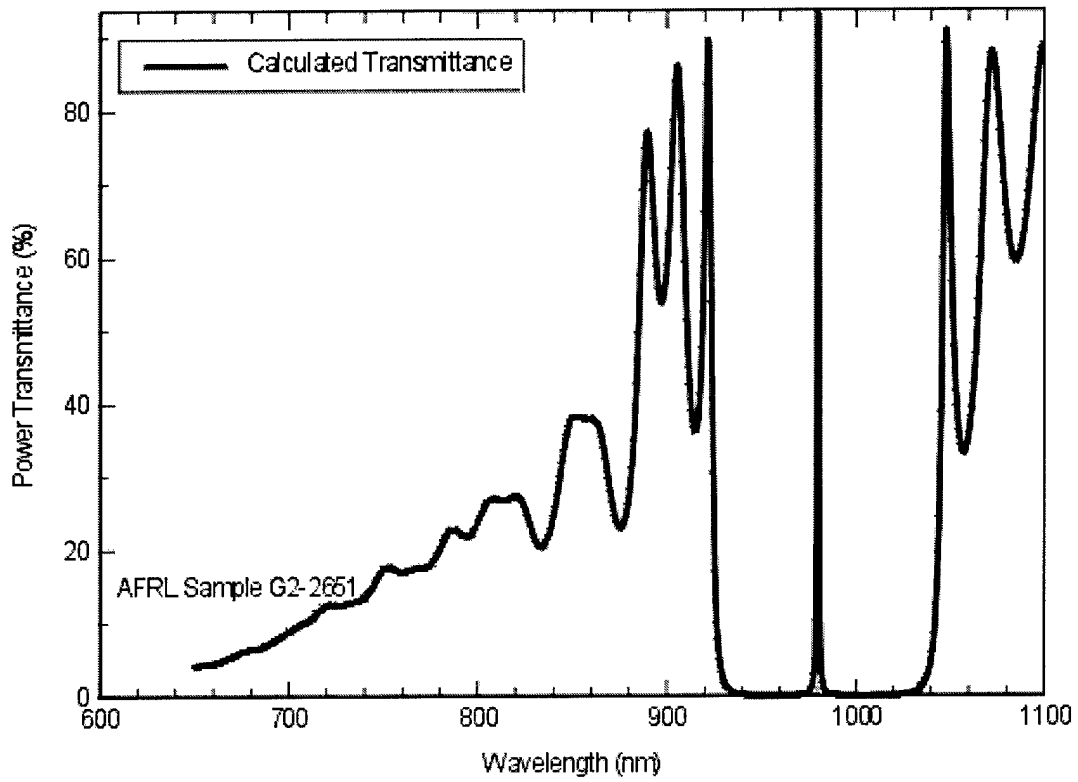


Figure 3.2 Calculated power transmittance spectra for AFRL sample G2 – 2651 (normal incidence).

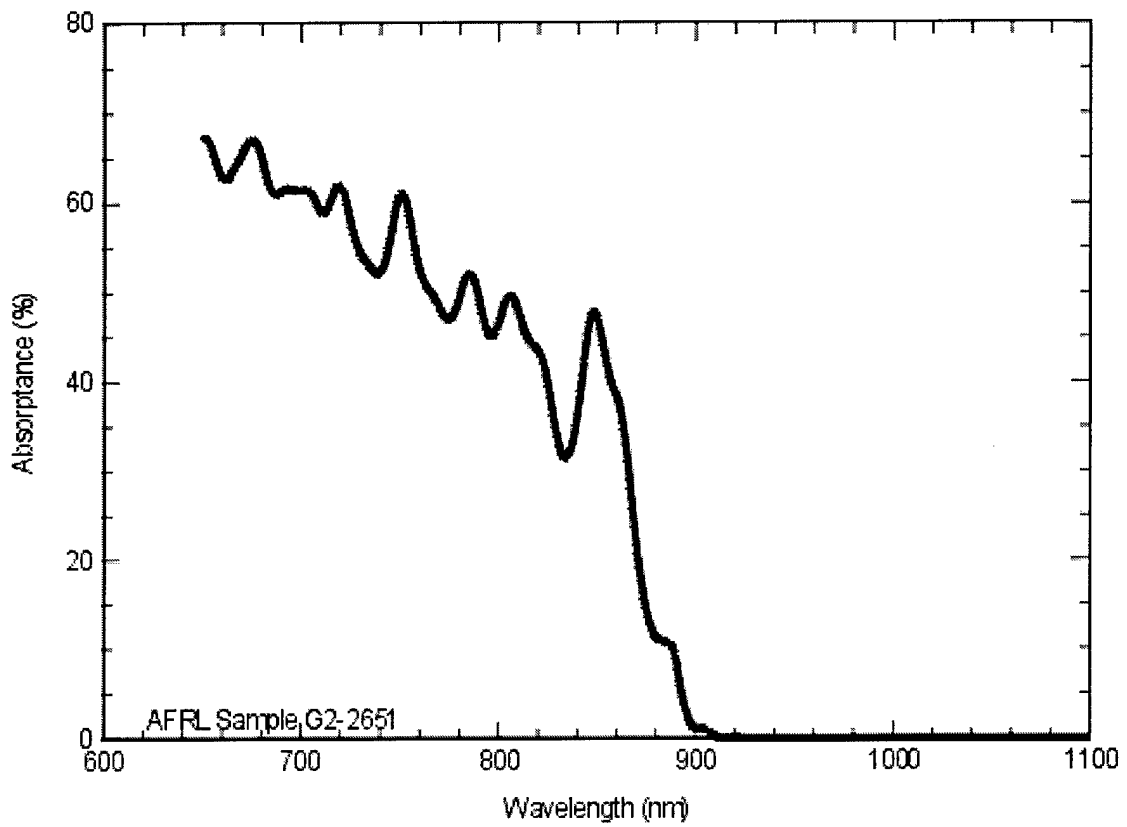


Figure 3.3 Calculated power absorbance spectra for AFRL sample G2-2651 (normal incidence).

was designed to place emphasis on the growth rate of the 3λ thick microcavity. Figure 3.5 shows the dependence of the Fabry-Perot dip feature as a function of cavity layer thickness change. The graph shows calculated power reflectance as a function of wavelength and of microcavity layer thickness variation. Figure 3.6 shows the change in Fabry-Perot resonance as a function of high-index (GaAs) layer thickness change. Figure 3.7 shows the same effect as the low-index (AlAs) layer is allowed to vary in thickness. All plots show a $\pm 10\%$ deviation from the originally calculated thickness values. Figure 3.5 shows the largest deviation in the location of the Fabry-Perot dip as a function of layer thickness change.

3.3 Reflectivity vs. Etch Depth Simulation

The modeling of power reflectance versus etch depth was completed for each of the MBE-grown samples. This data was used to etch the samples in the Plasma-therm inductively coupled plasma (ICP) etching system. I discuss the system details in Chapter 4.

Calculated power reflectance as a function of etch depth for the DBR structure shown in Table 3.2 are shown in Figure 3.8.

Table 3.2 DBR structure with λ_{Bragg} equal 800 nm used in calculation of power reflectance as a function of etch depth

Layer	Doping	Thickness (\AA)	Note
GaAs Substrate	(u)	∞	
AlAs	(u)	622	/-GaAs/AlAs DBR, Repeat—
GaAs	(u)	543	—20 Times—/

3.4 Regression Analysis and Curve Fitting Techniques

Measured reflectance data as a function of incident wavelength was collected for a variety of samples. Collected data from the MBE reflectance system (described in Chapter 4) can be seen in Figure 3.9. AFRL sample G2 – 2477 was grown as a 28 period GaAs/AlAs DBR structure as outlined in Table 3.3. My calculated power reflectance values for the sample are also shown

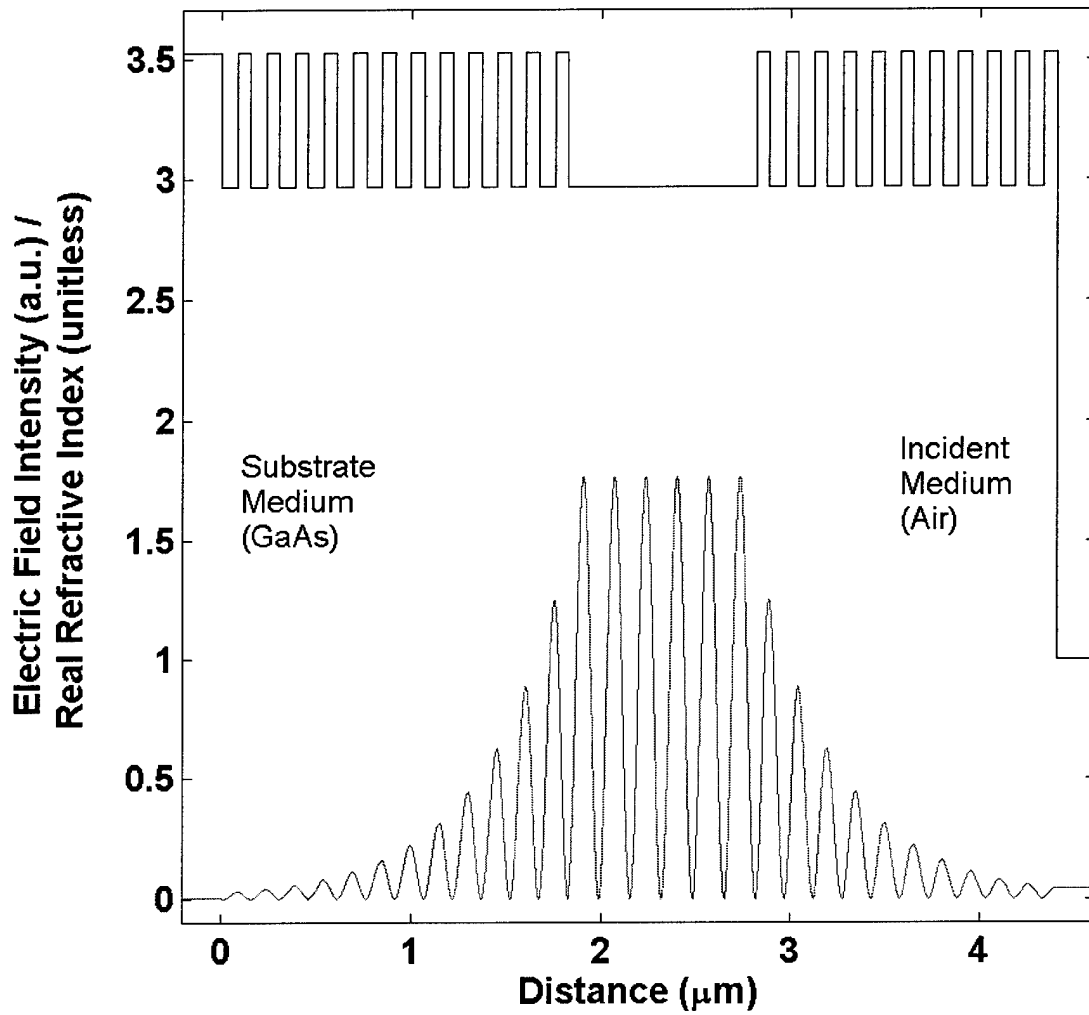


Figure 3.4 Calculated axial standing wave electric field intensity pattern for AFRL Sample G2-2651.

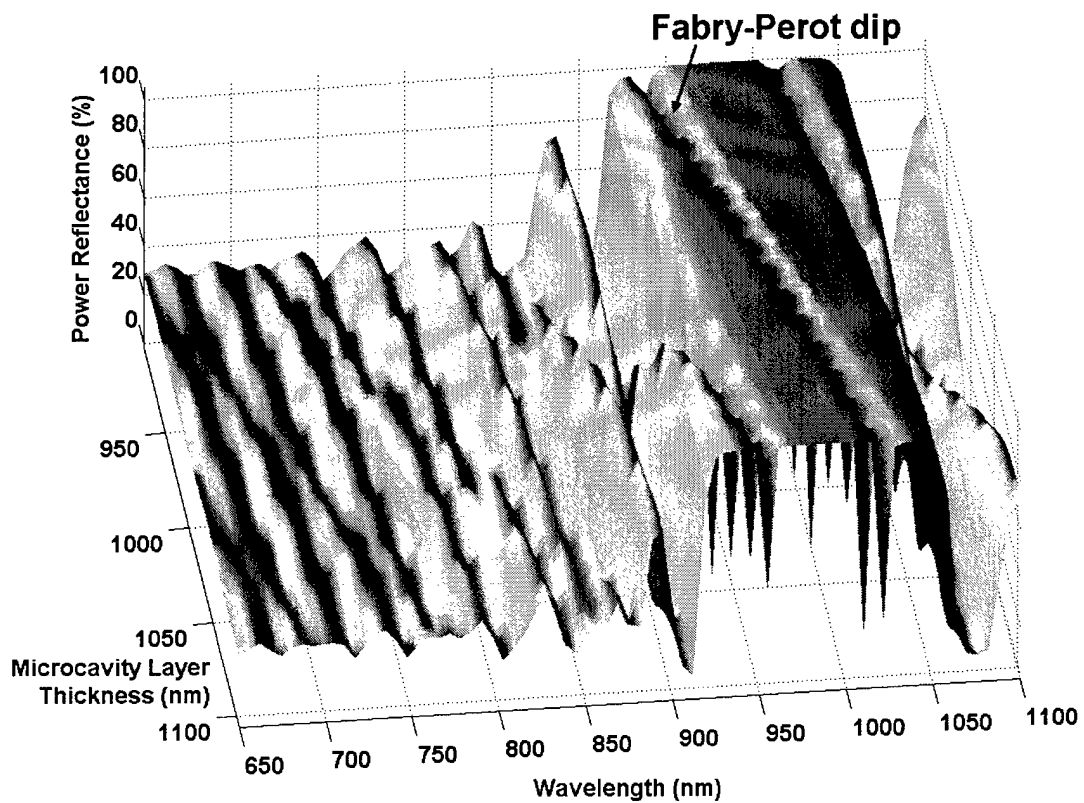


Figure 3.5 Calculated power reflectance as a function of wavelength and layer thickness ($\pm 10\%$) for the microcavity (AlAs) region for AFRL sample G2 – 2651 (Fabry-Perot etalon structure). Note strong sensitivity of the F-P dip wavelength to physical thickness of the microcavity layer. This dependent F-P shift is utilized to accurately calibrate MBE growth rates.

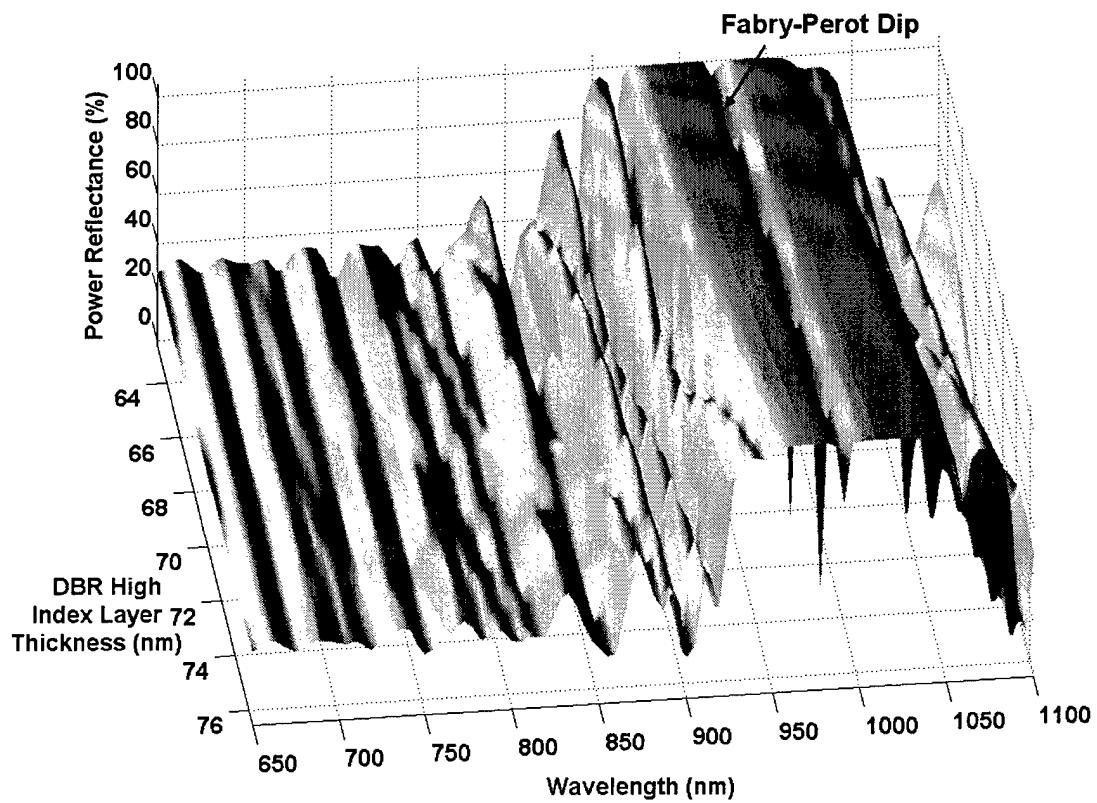


Figure 3.6 Calculated power reflectance as a function of wavelength and layer thickness variation ($\pm 10\%$) for the high (GaAs) quarter-wave layer in AFRL sample *G2* – 2651. Minimal shift in the F-P dip is observed.

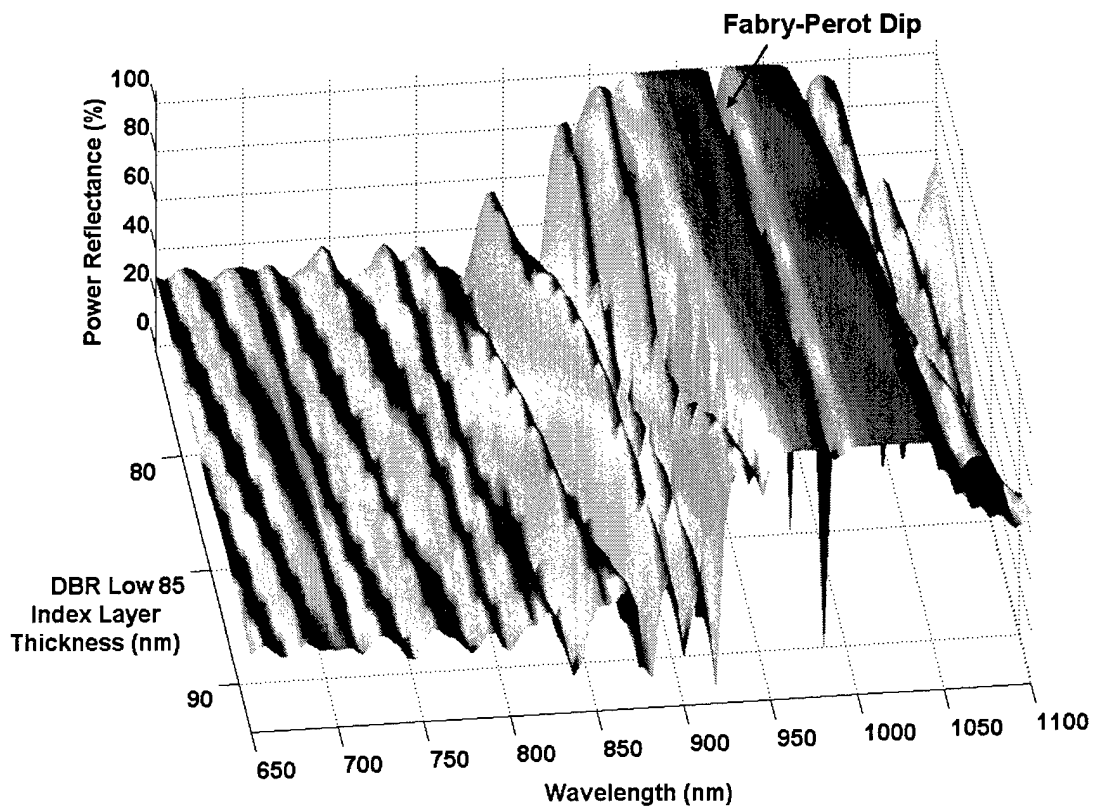


Figure 3.7 Calculated power reflectance as a function of wavelength and layer thickness variation ($\pm 10\%$) for the low (AlAs) quarter-wave layer in AFRL sample G2 - 2651. Minimal shift in the F-P dip is observed.

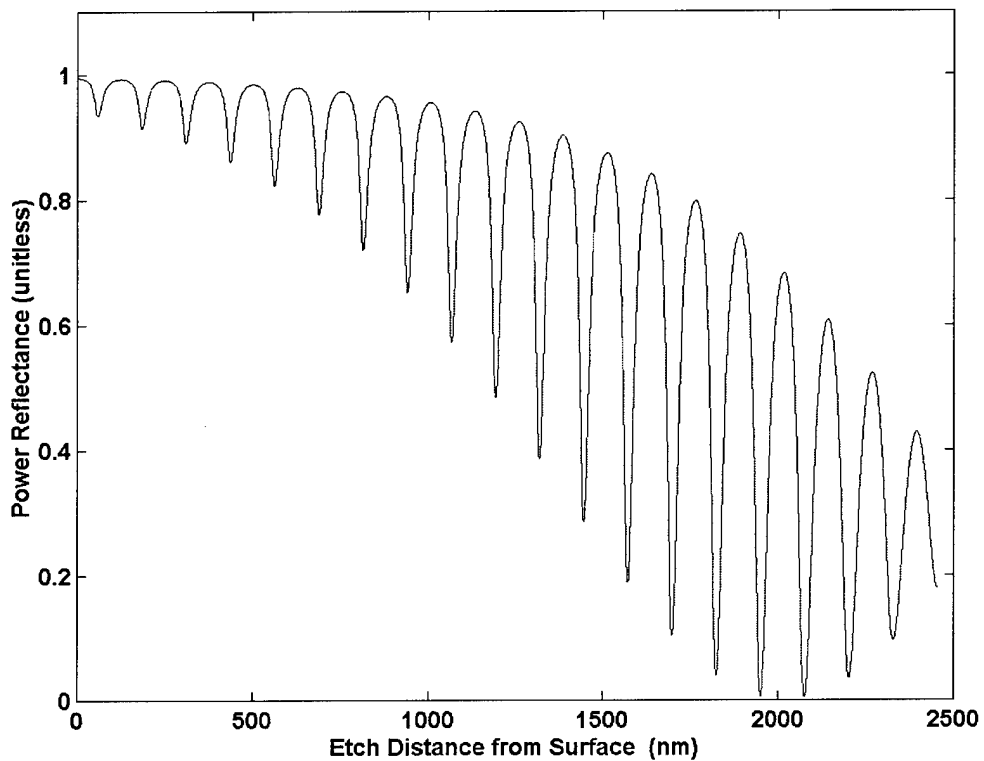


Figure 3.8 Calculated power reflectance as a function of etch depth for a 20-period GaAs-AlAs DBR on a GaAs substrate designed for $\lambda_{Bragg} = 800\text{nm}$ as seen in response to normally-incident 800nm light.

in Figure 3.9. There is a notable offset between calculated and measured values. This offset is due to layer thickness variations between the calculated model and the actual grown sample. The measured data is entered into regression analysis software (*FilmWizard*[®]) for analysis.

Table 3.3 28 Period GaAs/AlAs DBR structure (AFRL Sample G2 – 2477)

Layer	Doping	Thickness (Å)	Note
GaAs Substrate	(u)	∞	
AlAs	(u)	827	/-GaAs/AlAs DBR, Repeat—
GaAs	(u)	687	—28 Times—/

The reflectance data was used as the target values for regression analysis. Figure 3.10 shows the progress of the *FilmWizard*[®] software which uses a modified Levenberg-Marquardt algorithm. The original and fit values of layer thickness are shown in Table 3.4.

Table 3.4 Pre- and Post-Regression Analysis Thickness values for AFRL Sample G2 – 2477

Layer	Original Thickness (Å)	Fit Thickness (Å)	% Change
GaAs Substrate	(u)	∞	
AlAs	827	909	+12.6
GaAs	687	658	-4.2

Figure 3.11 shows the resultant calculated DBR reflectance spectrum after regression analysis. The extracted layer thickness values (see Table 3.4) dramatically improve the fit to measured data. The new layer thicknesses are then used to determine the actual epitaxial growth rates for AFRL's MBE system. The individual layer growth rates are then adjusted for subsequent MBE growths of DBR and microcavity structures.

3.5 Design of Microcavity Test Structures

In this section I discuss my design process for creating microcavity test structures. I first designed a multilayer Fabry-Perot etalon based on the regression analysis of AFRL sample G2 – 2651. The layer structure for my design, AFRL sample G2 – 2652, is shown in Table 3.5.

AFRL sample G2 – 2652 is a multilayer Fabry-Perot etalon structure composed of GaAs/AlAs DBRs surrounding a 2λ thick microcavity region. Calculated power reflectance as a function of

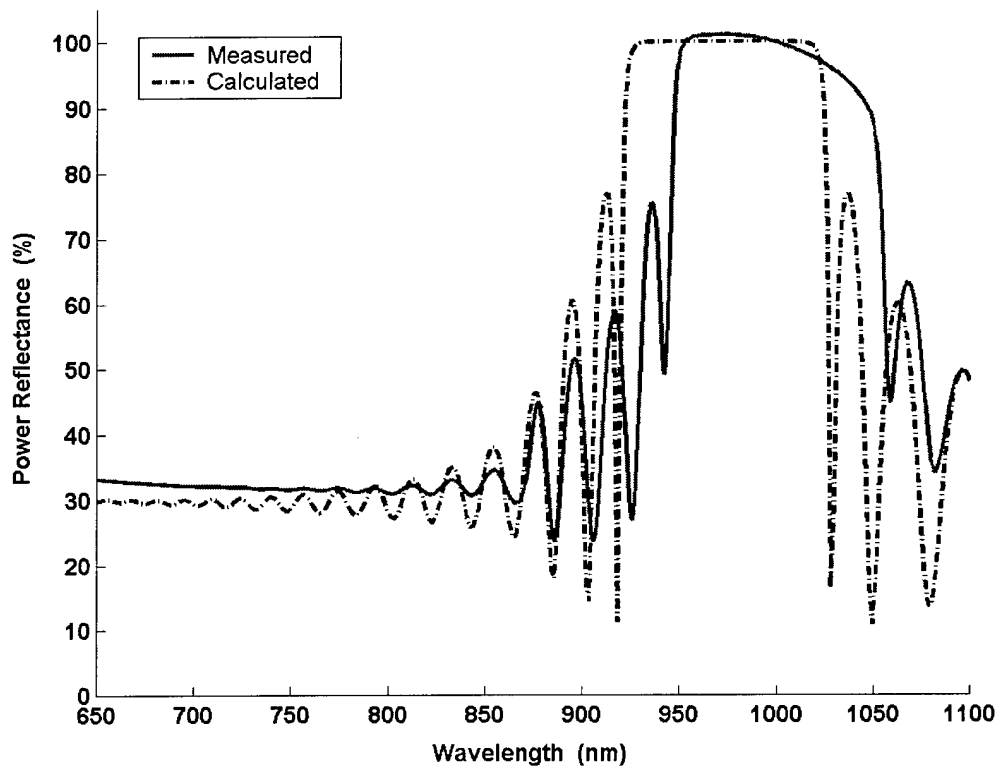


Figure 3.9 Calculated and measured reflectance spectra for AFRL sample *G2* – 2477. Figure shows offset between measured and calculated reflectance spectra. Offset is due to layer thickness variations from designed structure. Measured data is used to calibrate future MBE growth runs.

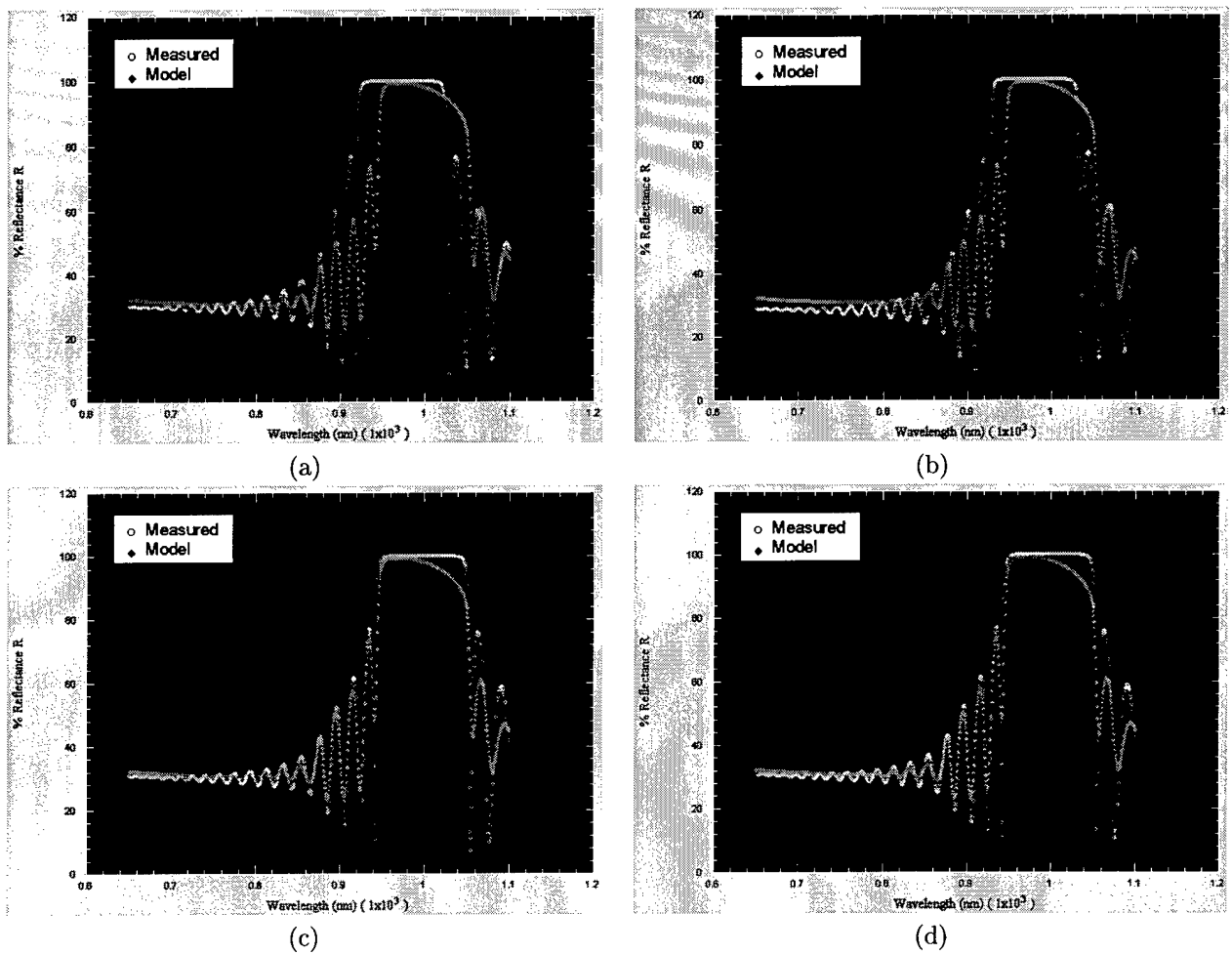


Figure 3.10 Progression of regression analysis for AFRL sample *G2 – 2477* for iterations 1-10; (a) iteration 1, RMSE = 17.109; (b) iteration 2, root mean squared error (RMSE) = 14.108; (c) iteration 3, RMSE = 8.822; (d) iteration 10, RMSE = 6.820. Progression shows reduction of overall RMSE as a function of iteration number. Analysis becomes insensitive to change after 10 iterations.

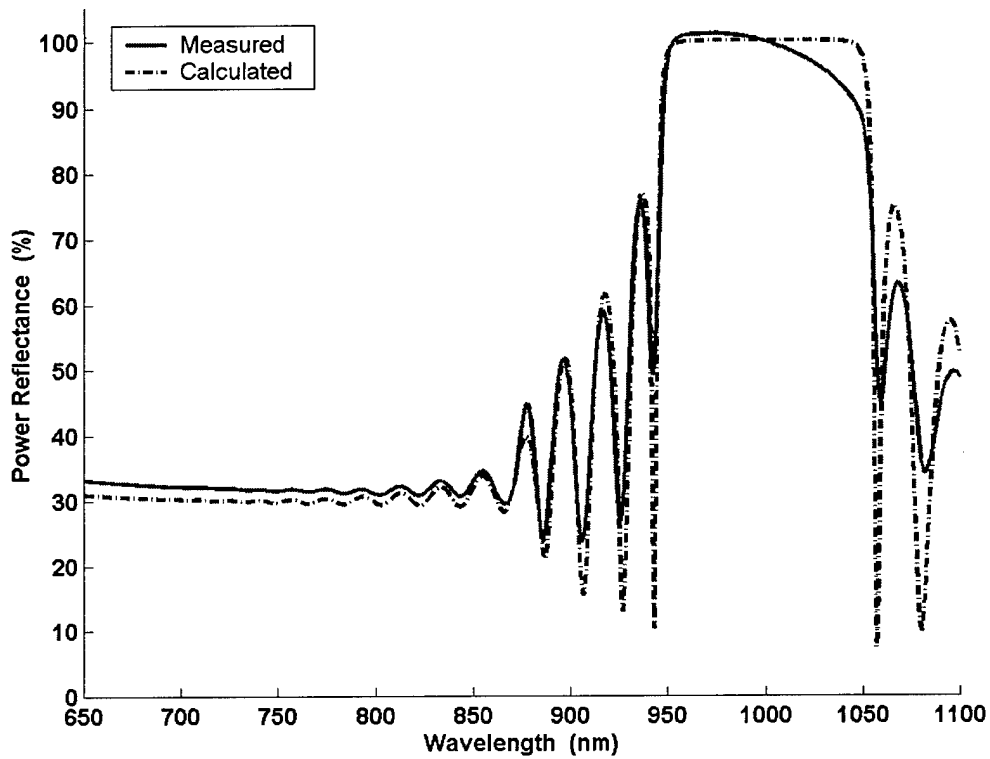


Figure 3.11 Calculated and measured reflectance spectra for AFRL sample G2-2477 (28-period DBR structure @ 980 nm) after regression analysis and change of physical layer thickness values. Adjustment of layer thickness values clearly yields a better fit to the measured data. Fit values are then used in conjunction with actual growth times to determine adjusted growth rates. This method improves overall growth accuracy and ultimately leads to improved device performance.

Table 3.5 Physical Layer Description for Fabry-Perot Etalon Structure with a 2λ -thick GaAs microcavity (AFRL sample G2-2652)

Layer	Doping	Thickness (Å)	Note
GaAs Substrate	(u)	∞	
AlAs	Si	838	/-Bot DBR, Repeat-
GaAs	Si	696	-11 Times-/
AlAs	Si	838	Extra $\frac{1}{4}\lambda$ layer
GaAs	(u)	5568	2λ microcavity @ 980nm
AlAs	C	838	/-Top DBR, Repeat-
GaAs	C	696	-10 Times-/

wavelength for both pre- and post-oxidation of this sample is shown in Figure 3.12. A constant index value of 1.55 for AlO layers, independent of wavelength, was used to model the structure after oxidation. Typical reported values for the refractive index of AlO are between 1.55 and 1.75 [10].

The data from samples *G2* - 2651 and *G2* - 2652 provided the growth rate information necessary to calibrate the MBE machine. I designed test microcavity structures for the purpose of extracting the optical parameters of native oxide layers. The aim was to design structures with power reflectances that are a sensitive function of the parameters of one or more AlO layers. One design limitation is the fact that I must be able to visually observe the oxidation from above the sample. This limits the number of DBRs that can be placed above the AlAs layers that are oxidized. AFRL's custom-designed oxidation system uses an integrated viewport and microscope to monitor the oxidation progress. The viewport is used to visually monitor oxidation length in real time. Highly reflective layers above the converted AlO layer inhibit the ability to monitor the extent of oxidation in an *in-situ* manner. If the layers are too reflective, other methods such as focused ion beam milling must be employed to investigate the extent of oxidation. The use of a focused ion beam system for etching studies is discussed in Chapter 5. Using the knowledge acquired from the previous growths, I designed a structure that was both sensitive to variations in AlO layer parameters and that included a minimal number of upper DBR periods. The test structure I designed is shown in Table 3.6. Calculated pre- and post-oxidation power reflectance spectra are shown in Figure 3.13. The structure was designed so that the microcavity region ($Al_{0.98}Ga_{0.02}As$)

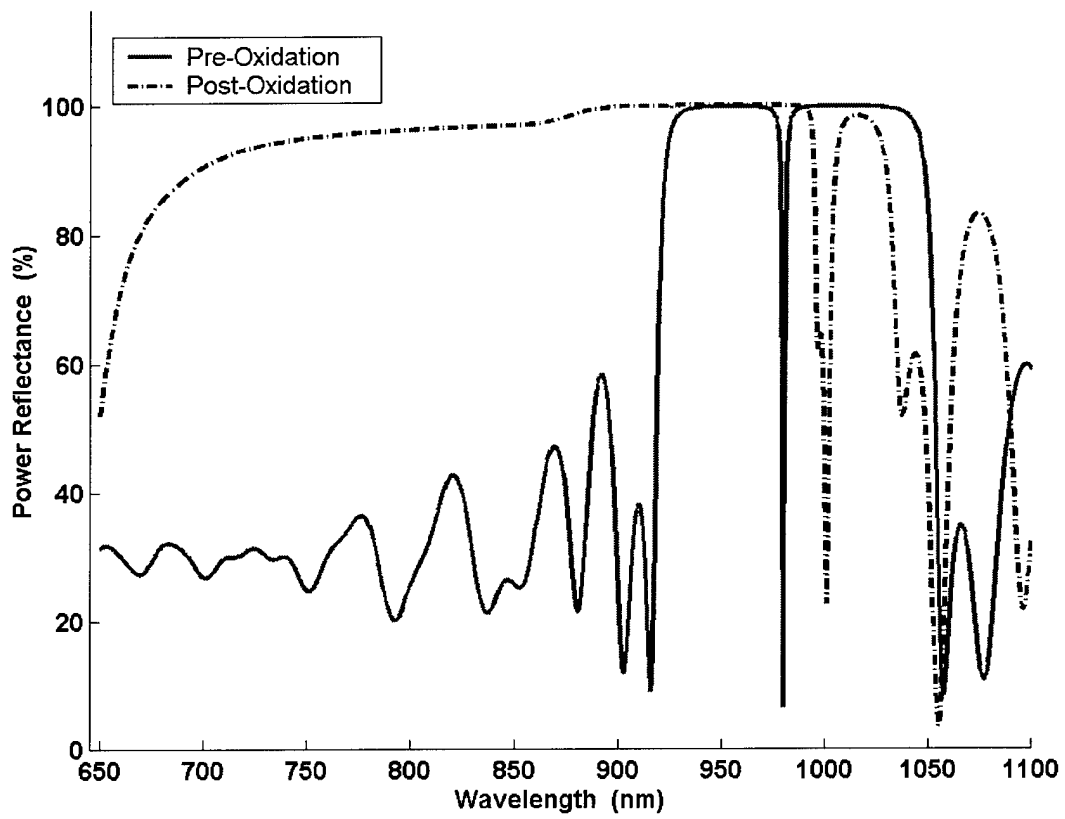


Figure 3.12 Calculated power reflectance spectra for AFRL sample G2 – 2652. Sample is evaluated for both pre- and post-oxidation. Assumed layer shrinkage is 12% [48].

would oxidize completely while the DBR layers ($Al_{0.9}Ga_{0.1}As$) would undergo negligible oxidation (see Figure 2.11 for AlGaAs oxidation rate dependence as a function of mole fraction of AlAs). The oxidation of the $Al_{0.98}Ga_{0.02}As$ microcavity will show the sensitivity of the Fabry-Perot dip as a function of optical thickness. Optical thickness parameters include both physical layer thickness and index of refraction making this an ideal power reflectance measurement structure from which to extract optical parameter information.

Table 3.6 Oxidation Test Structure 1 Physical Description (Sample G2-2658)

Layer	Doping	Thickness (Å)	Note
GaAs Substrate	(u)	∞	
$Al_{0.9}Ga_{0.1}As$	Si	817	/-Bot DBR, Repeat-
GaAs	Si	702	-10 Times-/-
$Al_{0.98}Ga_{0.02}As$	(u)	6221	1 λ microcavity @ 980nm
GaAs	C	702	
$Al_{0.9}Ga_{0.1}As$	C	817	
GaAs	C	702	

A second test structure is shown in Table 3.7. The VCSEL test structure contains a an $Al_{0.98}Ga_{0.02}As$ layer within the 1- λ thick microcavity that can be completely oxidized (designed for this thickness after oxidation with an assumed volumetric shrinkage of 6.7% after oxidation [51]). The microcavity also contains three InGaAs quantum well (QW) layers. The QW layers are placed at an antinode (peak) of the standing wave pattern inside the microcavity as shown in Figure 3.15. I designed the VCSEL structure for emission at 975nm. My calculated pre- and post-oxidation power reflectance spectra are shown in Figure 3.14.

The $Al_{0.98}Ga_{0.02}As$ layer is converted to AlGaO using techniques described in Chapter 4. The addition of Ga to the layer mitigates mechanical stability and reduces residual strain surrounding the oxidized layers. This structure will be analyzed for both optical properties and etch selectivity. The structure will also be useful for future research on tunable III-V MEMS devices [35].

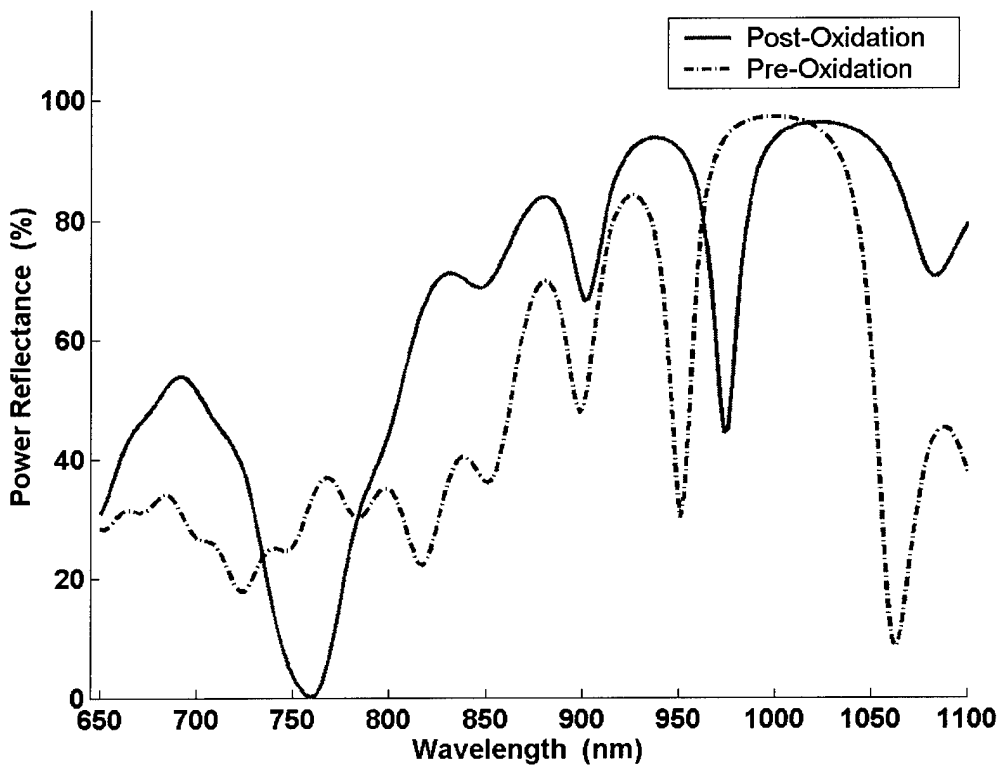


Figure 3.13 Calculated power reflectance spectra for AFRL sample *G2* – 2658. Sample is evaluated for both pre- and post-oxidation with an assumed volumetric shrinkage of 6.7% [51].

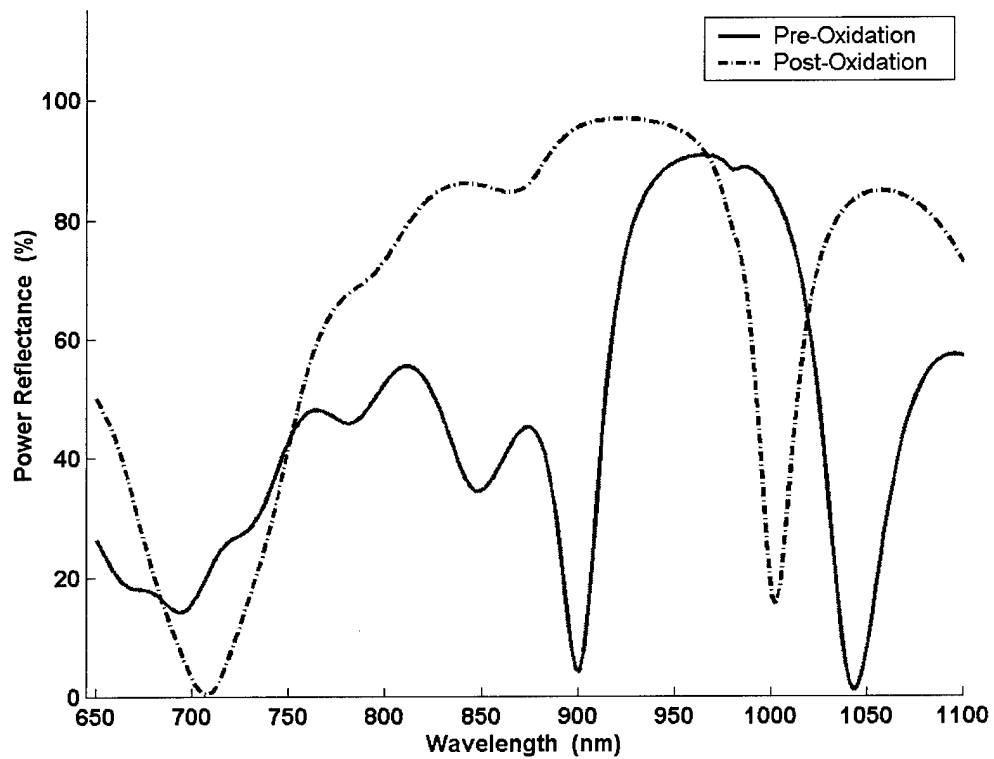


Figure 3.14 Calculated power reflectance spectra for AFRL sample G2 – 2663. Sample is evaluated for both pre- and post-oxidation.

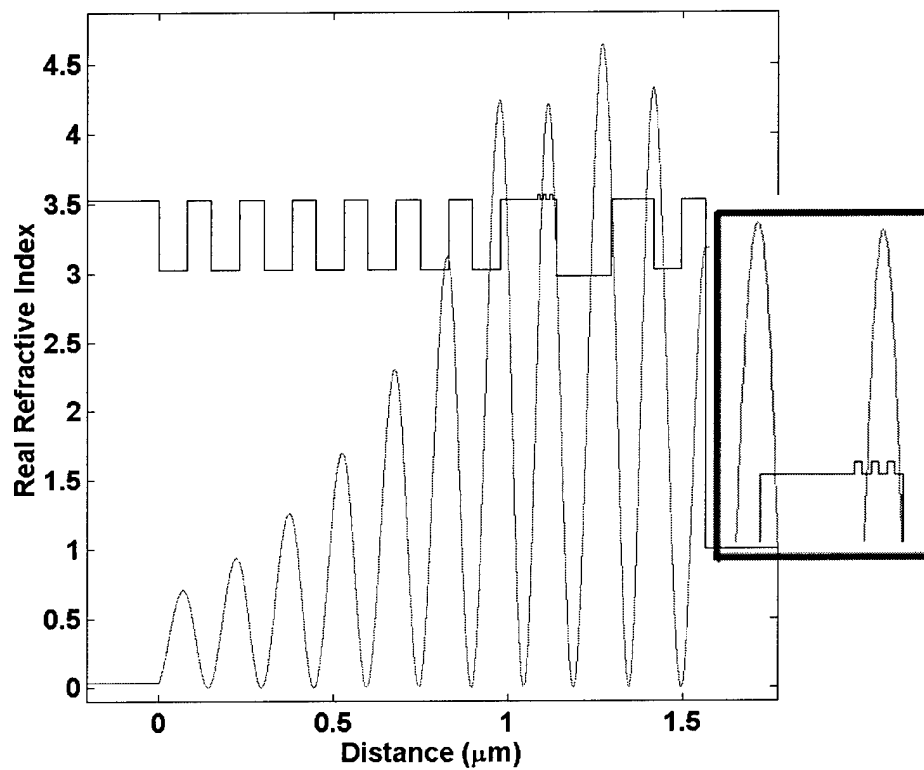


Figure 3.15 Calculated standing wave pattern (electric field intensity) and refractive index profile for AFRL sample G2 – 2663. Inset shows zoomed in view of InGaAs quantum well region and the overlap with the standing wave pattern.

Table 3.7 Oxidation Test Structure 2 Physical Description(Sample G2-2663)

Layer	Doping	Thickness (Å)	Note
GaAs Substrate	(u)	∞	
$Al_{0.9}Ga_{0.1}As$	Si	812	/-Bot DBR, Repeat-
GaAs	Si	691	--6 Times--/
$Al_{0.9}Ga_{0.1}As$	Si	812	Extra $\frac{1}{4}\lambda$ layer
GaAs	Si	1049	GaAs Spacer Layer
$In_{0.2}Ga_{0.8}As$	(u)	80	QW Layer
GaAs	(u)	100	GaAs Spacer Layer
$In_{0.2}Ga_{0.8}As$	(u)	80	QW Layer
GaAs	(u)	100	GaAs Spacer Layer
$In_{0.2}Ga_{0.8}As$	(u)	80	QW Layer
GaAs	(u)	100	GaAs Spacer Layer
$Al_{0.98}Ga_{0.02}As$	(u)	1500	Layer Converted to AlO inside μ -cavity
GaAs	(u)	500	GaAs Spacer Layer
$Al_{0.9}Ga_{0.1}As$	C	812	
GaAs	C	691	

3.6 Chapter 3 Summary

In Chapter 3 I evaluated several different modeling tools and procedures used to design and grow microcavity test structures containing AlO layers. The use of modeling and simulation is an ideal way to design devices when a large variety of variables or alternate designs exist. These efforts save time and money necessary for the actual growth and processing of devices and can be used to effectively evaluate a structure's expected performance prior to growth and fabrication. I evaluate test methods and describe the procedures I used to fabricate and characterize the actual microcavity test devices in the next chapter .

4. Equipment for Device Fabrication and Characterization

4.1 Introduction

In this chapter I discuss the equipment and procedures I used to fabricate and characterize microcavity test structures for the purpose of determining optical parameters and characteristics of AlO layers. I examine device growth, processing, post-processing, and measurement techniques in detail. This chapter concludes with an explanation of the steps I used to perform selective etching of native oxide layers for the purpose of initiating research development of a III-V MEMS technology at AFIT; specifically aimed at the fabrication of tunable VCSEL devices.

I performed my work at AFRL Sensors Directorate (SN) facility. The facility houses a class 100 clean room laboratory. The clean room has the capability to grow, process, and characterize a wide range of photonic and electrical device structures. In order to prepare for thesis research in a clean room environment, I worked with Dr Stewart Feld [17] and processed selectively-oxidized 980nm VCSEL devices which incorporated InGaAs quantum well structures in the active region. These devices were grown on-site by using the Varian Gen II MBE machine. This work led to the creation of a VCSEL fabrication recipe for AFRL's low-threshold oxide-apertured device. The processing steps are found in Appendix A and are referenced several times throughout the processing sections of this thesis.

I used the methods in the following sections to grow and process DBR and microcavity test samples for evaluations. Large-scale oxidation runs (for geometries $\geq 50\mu m$) were performed for the first time using the custom-built AFRL oxidation system. I also performed preliminary studies on horizontal selective etching of native oxide layers within an optical structure for the first time at AFRL.

4.2 Molecular Beam Epitaxy Growth

The MBE process creates crystalline epitaxial layers under ultra high vacuum conditions. Beams of differing flux density and chemical composition impinge upon a heated single crystal substrate using precise shuttering techniques. Each constituent element is separately contained and heated in its own crucible. Temperature is then used to precisely control the compositional make-up of the epitaxial film. Studies have demonstrated that the kinetically dominated MBE process is prescribed by the surface chemical dependence of the sticking coefficient of the group III elements [2]. That is to say that the stoichiometric growth of III-V epitaxial layers can be tightly controlled by the flux density of the group III elements. A photograph of the AFRL MBE machine can be found in Figure 4.1 and a system schematic is shown in Figure 4.2. Further details on MBE operating principles and the advantages of using MBE over other growth techniques can be found in the literature [21] [26] [52].

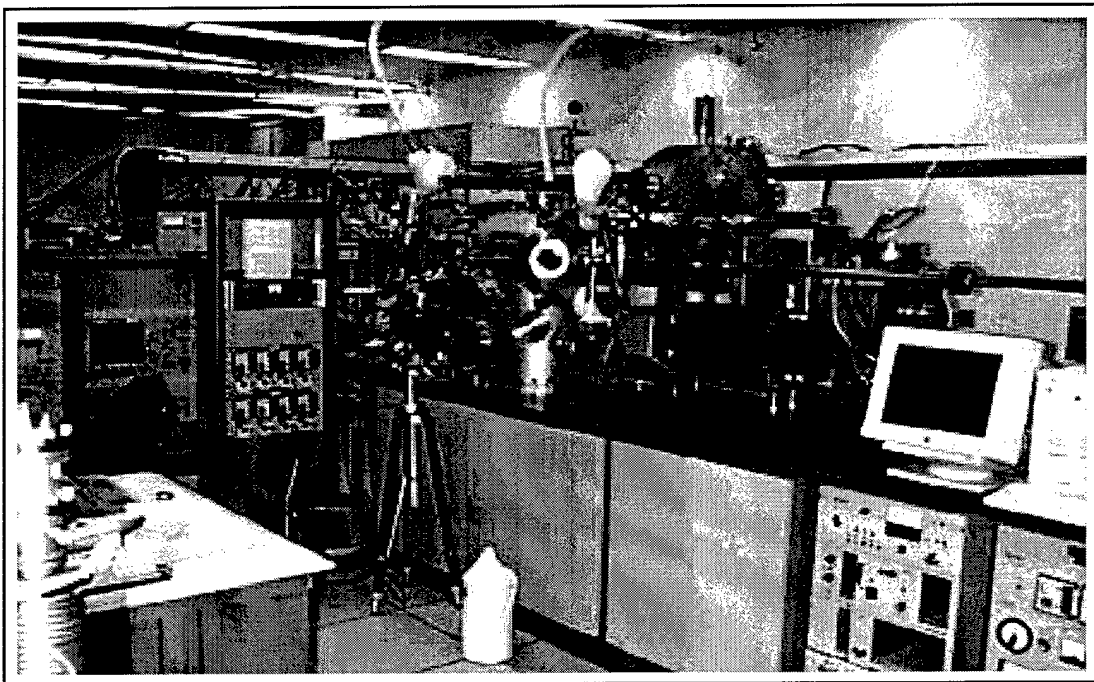


Figure 4.1 Photograph of the Air Force Research Laboratory's Varian Gen II molecular beam epitaxy system used to grow my test structures.

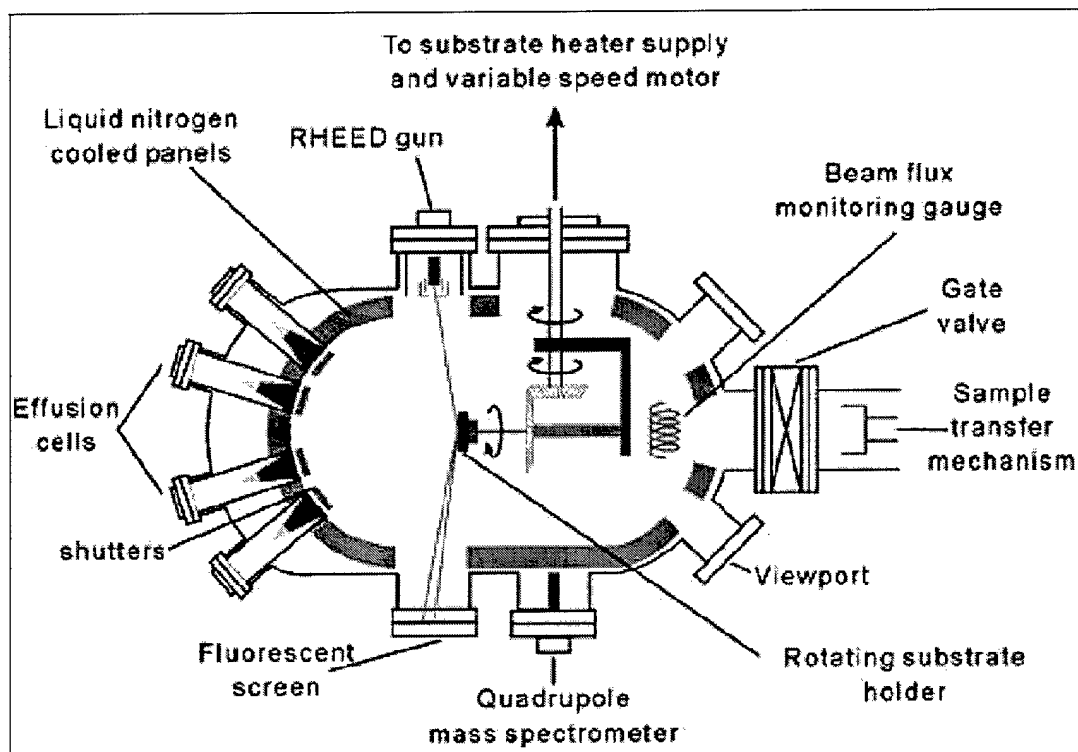


Figure 4.2 Schematic of the Air Force Research Laboratory's Varian Gen II molecular beam epitaxy system used to grow my test structures.

4.3 MBE Reflectance System

Once a structure's theoretical optical response has been verified through modeling, it is then physically grown in the MBE machine. Proper growth can then be validated through the use of a reflectance monitoring system that is an integrated part of the MBE equipment. A schematic for AFRL's in-situ reflectance system is shown in Figure 4.3. The system uses a white light source with a fiber optic coupling cable to illuminate wafers inside the MBE's wafer preparation chamber. Light is then collected by a second fiber and fed into a computer that contains a spectrometer card. The computer analyzes the signal at the individual wavelengths and displays a graph of the results. A wafer coated with a thin layer of gold ($\sim 2000\text{-}5000 \text{ \AA}$; also located inside the MBE preparation chamber) is used as a reference for the reflection measurements. Data was collected after each MBE growth. An example spectrum obtained through this MBE system reflectance monitoring system for sample G2-2651, as detailed in Table 3.1, is shown in Figure 4.4.

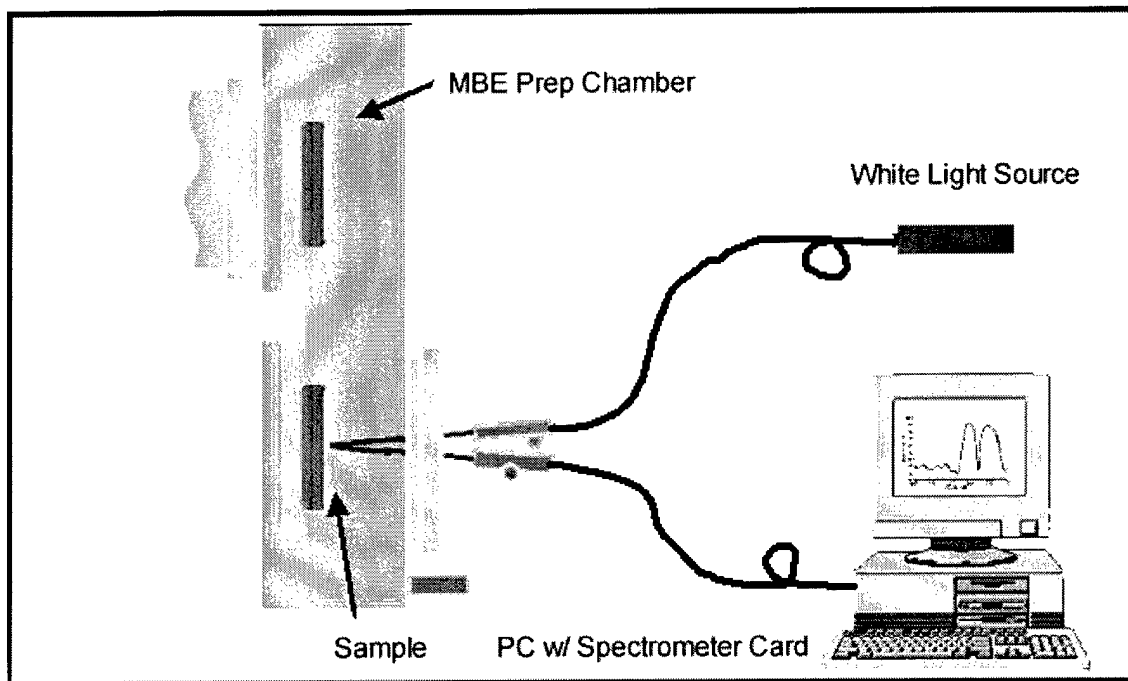


Figure 4.3 Schematic of MBE reflectance measuring system used to calibrate epitaxial growth rates immediately following a process run [33].

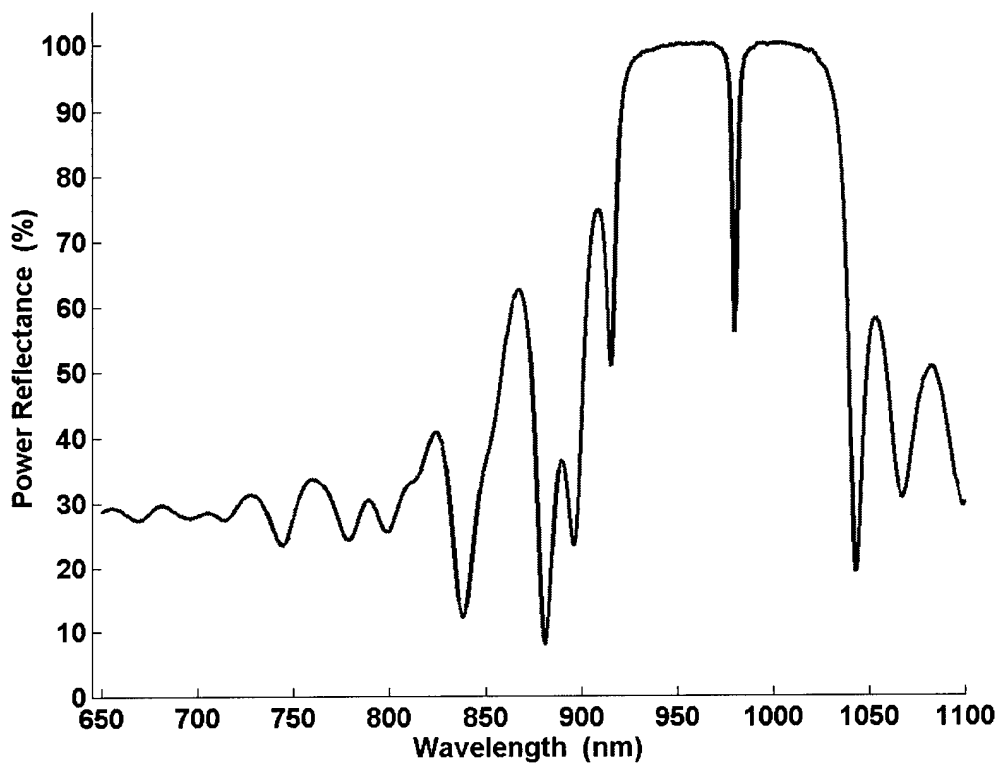


Figure 4.4 Measured reflectance spectrum for sample *G2* – 2651 ($3\text{-}\lambda$ thick AlAs cavity with GaAs/AlAs DBR mirror layers) as taken immediately after MBE growth.

4.4 Device Processing

4.4.1 Mask Alignment. An MJB-3 ultra-violet mask aligner is used to define device features. The MJB-3 system uses a contact mask and can process full wafers or smaller (e.g. $\frac{1}{4}$ wafer) samples. Figure 4.5 shows a photograph of the mask used to define the mesa structures (VCSEL Mask 02) used extensively in my research. The figure shows resist that has been patterned prior to etching in the inductively coupled plasma (ICP) etching system.

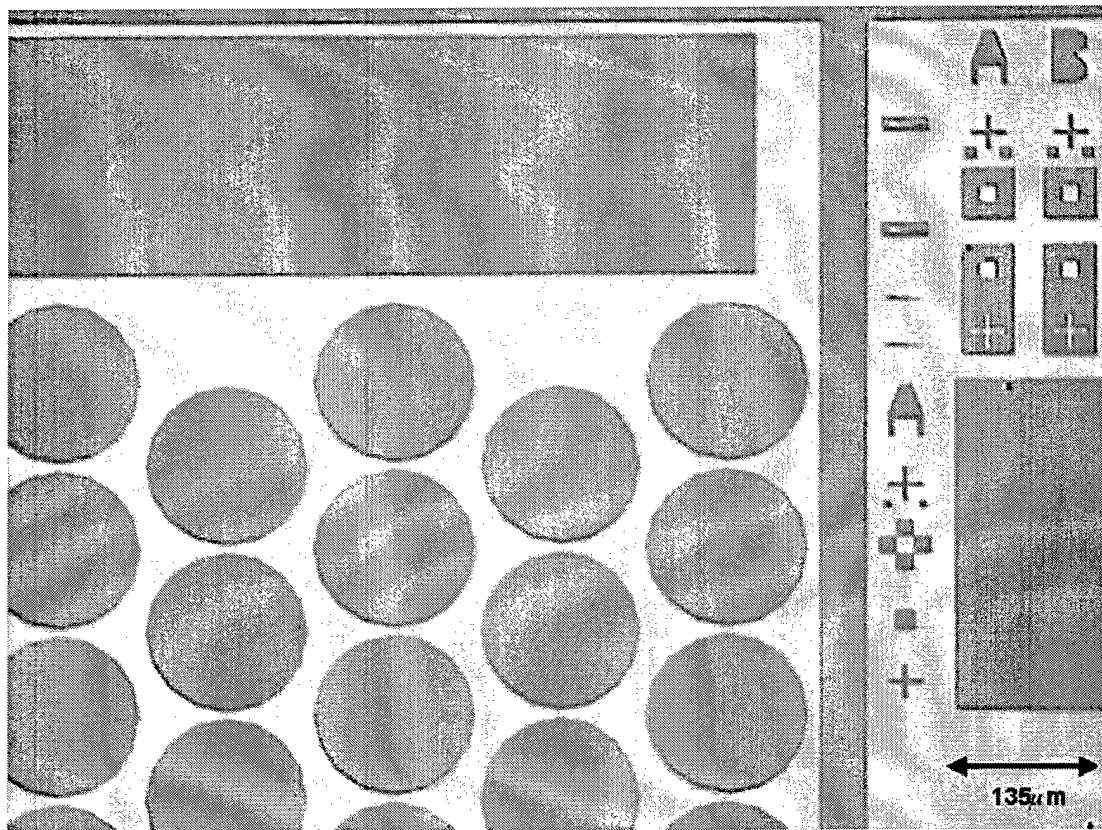


Figure 4.5 Microscope view of features patterned using MJB-3 mask aligner after a subsequent mesa etch using the ICP system (AFRL sample G2 – 2658 patterned with VCSEL Mask 02).

4.4.2 Metal Deposition. Once a structure has been grown, it must then be processed into individual devices. The first step in the VCSEL fabrication process is to deposit the p-ohmic metal layer (a combination of deposited titanium and gold layers). The metal is deposited using a

Temescal BJD 1800 electron-beam deposition system. A two-step resist patterning process is used (see Appendix A, Section A.1) in order to effectively "lift off" unwanted p-ohmic metal.

4.4.3 Mesa Definition and Plasma Etching Reflectance System. After excess metal has been removed, the mesa mask is used to pattern MicroPosit 1818 photoresist to define the individual device mesas. The device mesas are then etched in a Plasma Therm ICP etching system by flowing Cl_2 and BCl_3 in the presence of an applied RF field.

An in-situ laser reflectometry system is used to accurately measure the etch progress of the ICP system. The reflectance signal, as a function of time, is monitored and compared to a theoretical plot of reflectance as a function of etched distance. This technique can be effectively used to expose a portion or all of the desired structure with an accuracy of $\pm 100nm$ (depending on applied plasma power). A schematic for the laser reflectometry setup used to monitor etch progress is shown in Figure 4.6. Sample reflectance data from the ICP reflectance system is shown in Figure 4.7. The ICP systems offers an anisotropic etch that limits the negative effects of sidewall scattering due to surface roughness. Figure 4.8 shows a comparison of the anisotropic ICP etch versus an isotropic wet chemical etch performed at room temperature with $H_2SO_4:H_2O_2:H_2O$ (1:1:10).

4.5 Oxidation System

An oxidation system must exhibit repeatability and controllability. A custom oxidation system was built at the Air Force Research Laboratory to address this issue [19]. The custom built oxidation system is shown in Figure 4.9 and Figure 4.10. The system has an integrated view port which allows for in-situ monitoring of the oxidation process. The system is operated at low pressure (5 Torr) to inhibit the formation of moisture on the viewport. The sample is loaded onto a copper-plated thermal chuck. A vacuum is then pulled inside the sample oxidation chamber. The chuck is then heated to the desired oxidation temperature (350 - 450° C). A mechanical valve is then opened to the liquid H_2O source. The vacuum creates water vapor inside the source container.

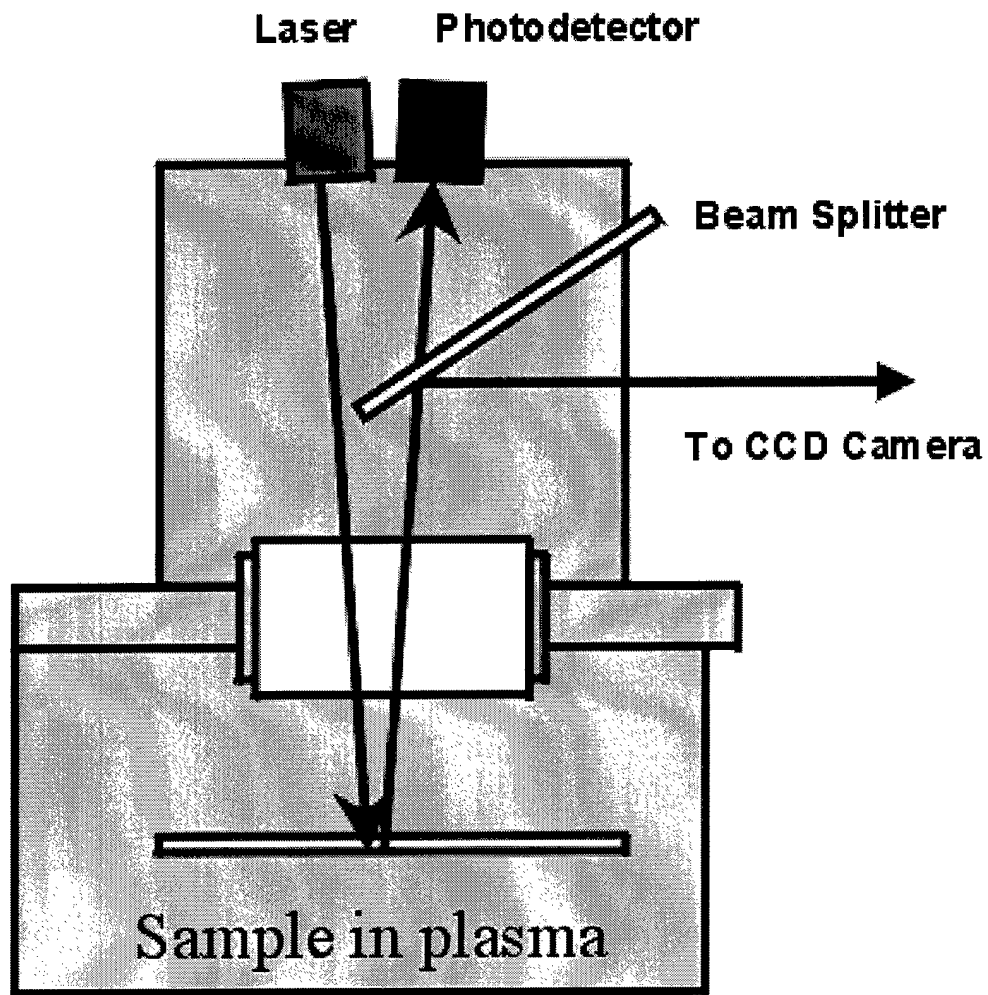


Figure 4.6 Schematic of the ICP etch chamber in-situ reflectance measurement system [33].

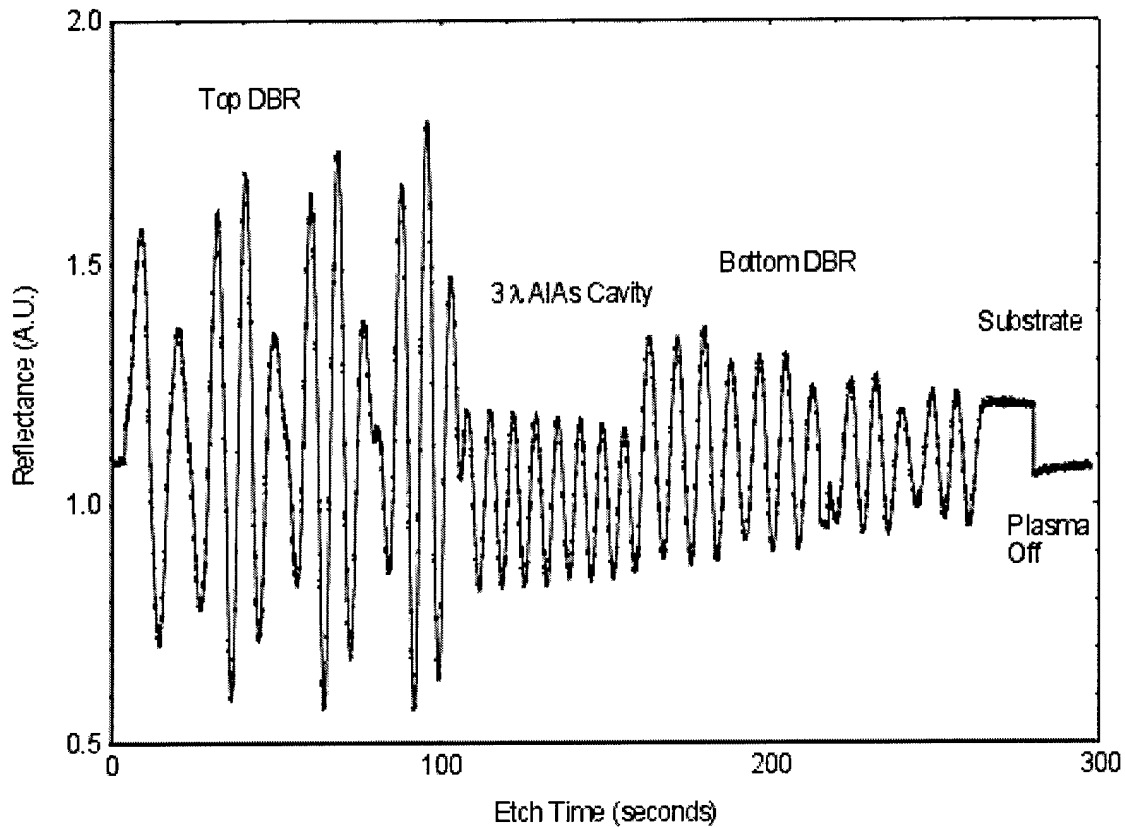


Figure 4.7 Data collected from the ICP laser reflectometry system (during ICP mesa etch of AFRL sample G2 – 2651). The measurement wavelength is 760nm.

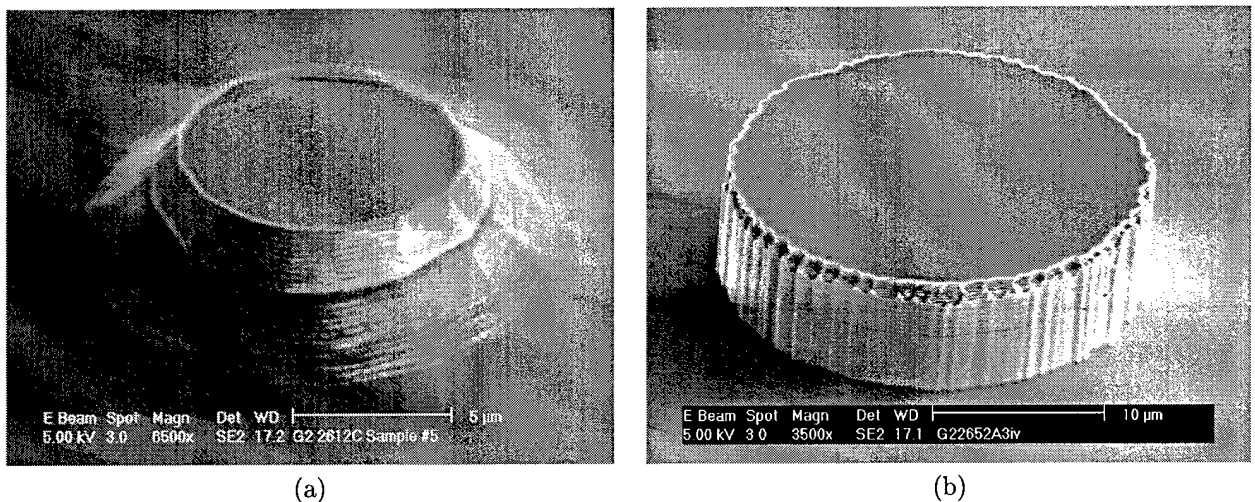


Figure 4.8 Mesa etch profile comparison for wet and dry etching techniques. Figure shows (a) isotropic wet etch using a sulfuric acid and H_2O_2 solution (AFRL sample G2 – 2612) and (b) results of an anisotropic etch performed by the AFRL ICP system while flowing Cl_3 and BCl_3 at a pressure of 10 Torr (AFRL sample G2 – 2652).

The water vapor flow is controlled using a vapor source mass flow controller. Vapor flow is set to 500 sccm and pressure inside the oxidation chamber is maintained at 5 Torr through the use of an adaptive pressure controller. The system was designed so that the chamber could be evacuated quickly once the desired oxidation time has been reached, thus halting the oxidizing reaction. Research has shown that it is necessary to restrict VCSEL aperture diameters to less than $10\mu\text{m}$ to achieve sub-mA threshold current [13]. The combination of optical in-situ monitoring and precise control lead to a process which is stable, repeatable, and accurate enough to create devices meeting the stringent aperture requirements of ultra-low threshold devices. Table 4.1 shows the results of completed oxidation runs.

Table 4.1 Chronology of Completed Oxidation Runs

Date	Sample ID	Ox Time hr:min	Temp ($^{\circ}\text{C}$)	Notes
13 Nov 00	G22547/G22551	5:12	375	Oxide Aperture VCSEL Devices
29 Dec 00	G22477b(E5)	8:37	400	DBR w/ metal, blocked oxidation
3 Jan 01	G22477b(E4)	5:21	400	DBR w/ metal removed
4 Jan 01	G22477b(E4)	10:36	400	Con't oxidation of sample (tot ox time 15:57)
5 Jan 01	G22477b(E4)	10:08	400	Con't oxidation of sample (tot ox time 25:05)
10 Jan 01	G22612C(#4)	8:42	400	Etalon structure, $\frac{3}{2}\lambda$ AlAs cavity, GaAs/AlAs DBRs
2 Feb 01	G22651/G22652	14:34	400	Etalons, GaAs & AlAs cavities w/ GaAs/AlAs DBRs
26 Feb 01	G22658	25:01	400	1λ $\text{Al}_{0.98}\text{Ga}_{0.02}\text{As}$ μ -cavity

4.6 Reflectance Measurements

Reflectance data was collected on oxidized samples using the system configuration shown in Figure 4.11. A white light source illuminates the sample after passing through a collimating lens, a chopper set to a rotation speed of 400 rps, a beam splitter, and a focusing objective. The objective's spot size was on the order of $70\mu\text{m}$. Light was then focused onto oxidized mesas using a charge coupled device (CCD) camera and corresponding monitor. The placement of the CCD camera in the image plane allows for imaging of the individual mesa structures ($\sim 130\mu\text{m}$ in diameter). The sample mount allowed for three dimensional positioning of the sample and thus the focused beam could be correctly positioned. The reflected light beam was sent back through the first focusing

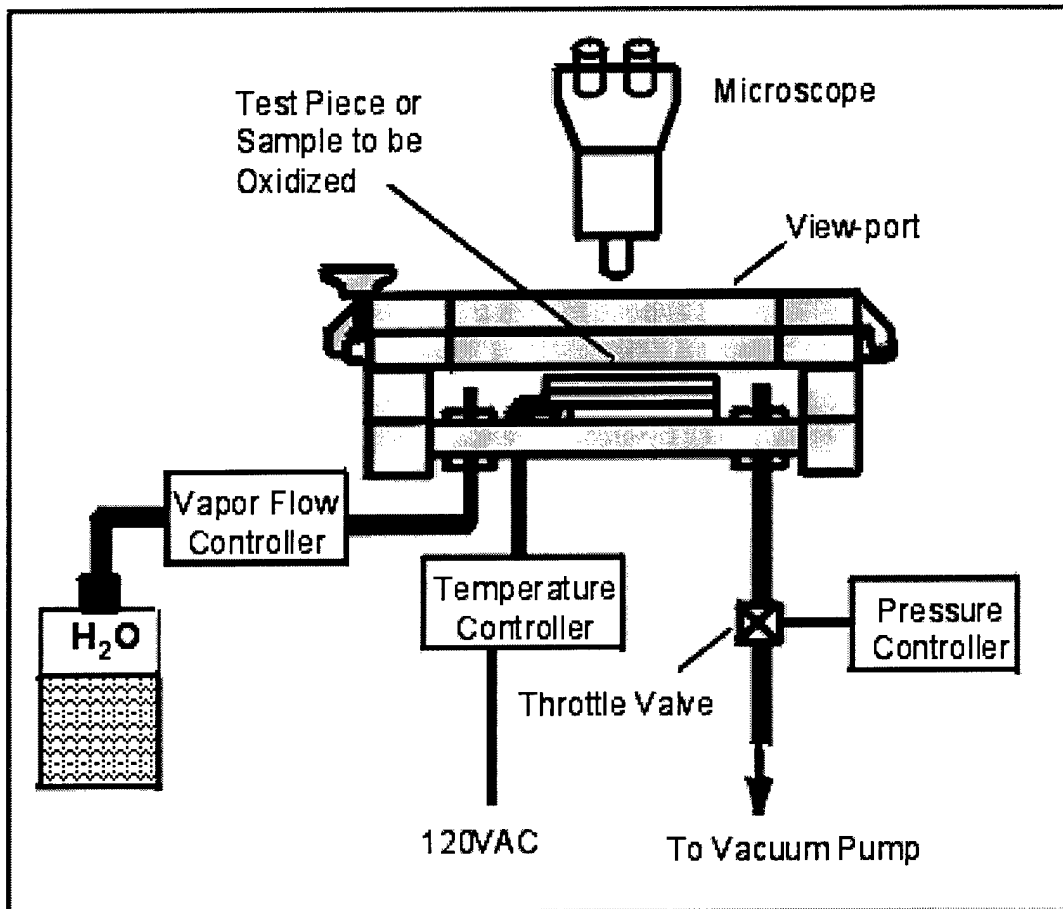


Figure 4.9 Schematic of AFRL's custom-built AFRL oxidation system [18].

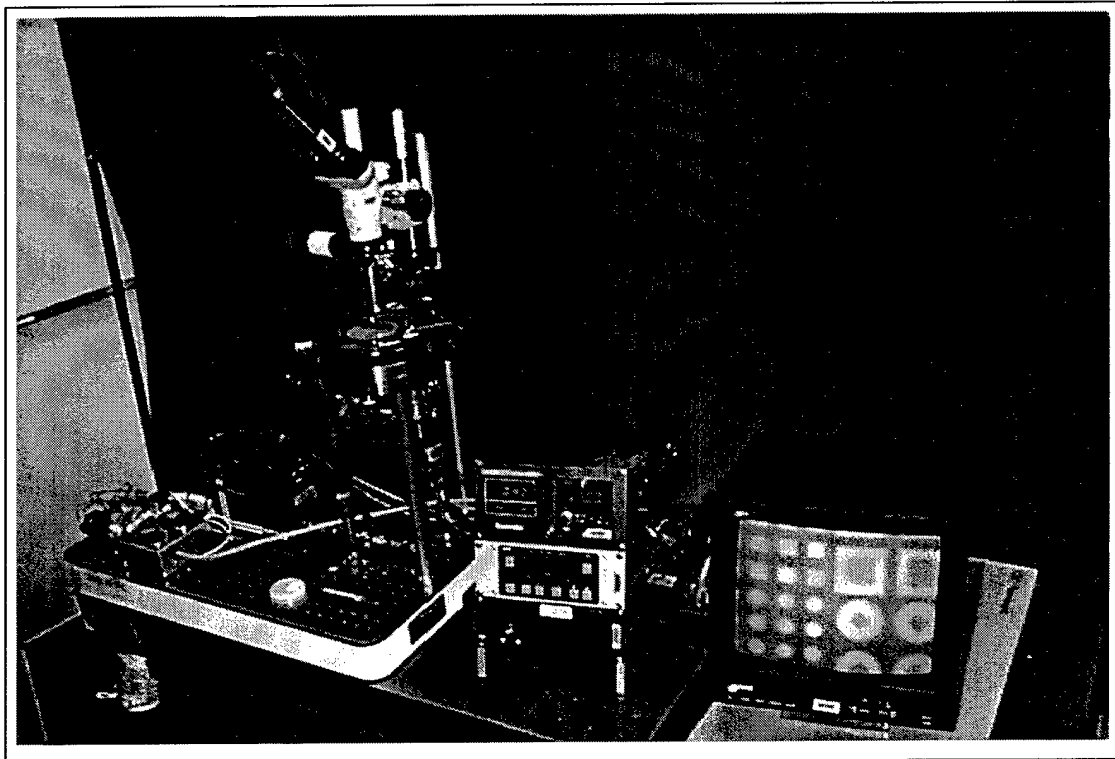


Figure 4.10 Photograph of the custom-built AFRL low-pressure oxidation system [18]. The monitor on the right displays an oxidation in progress for both square and round mesas. The CCD camera is equipped with a near-IR filter to enhance the contrast between oxidized and non-oxidized layers. The oxidized portion of the layers appear lighter in the image.

objective, resulting in a collimated output beam, and then reflected off the beam splitter for a second time. The beam splitter redirects reflected light toward a directional mirror. A second directional mirror sends the beam through an optical collecting element and into the grating of the SpectraPro 0.3 meter triple grating monochromator. The monochromator selects out an individual wavelength of light and sends the signal to an indium gallium arsenide (InGaAs) photodetector. The InGaAs photodetector offers a greater sensitivity in the infrared (IR) than a typical silicon photodetector whose range is usually between $0.3 \mu\text{m}$ and $1.0 \mu\text{m}$.

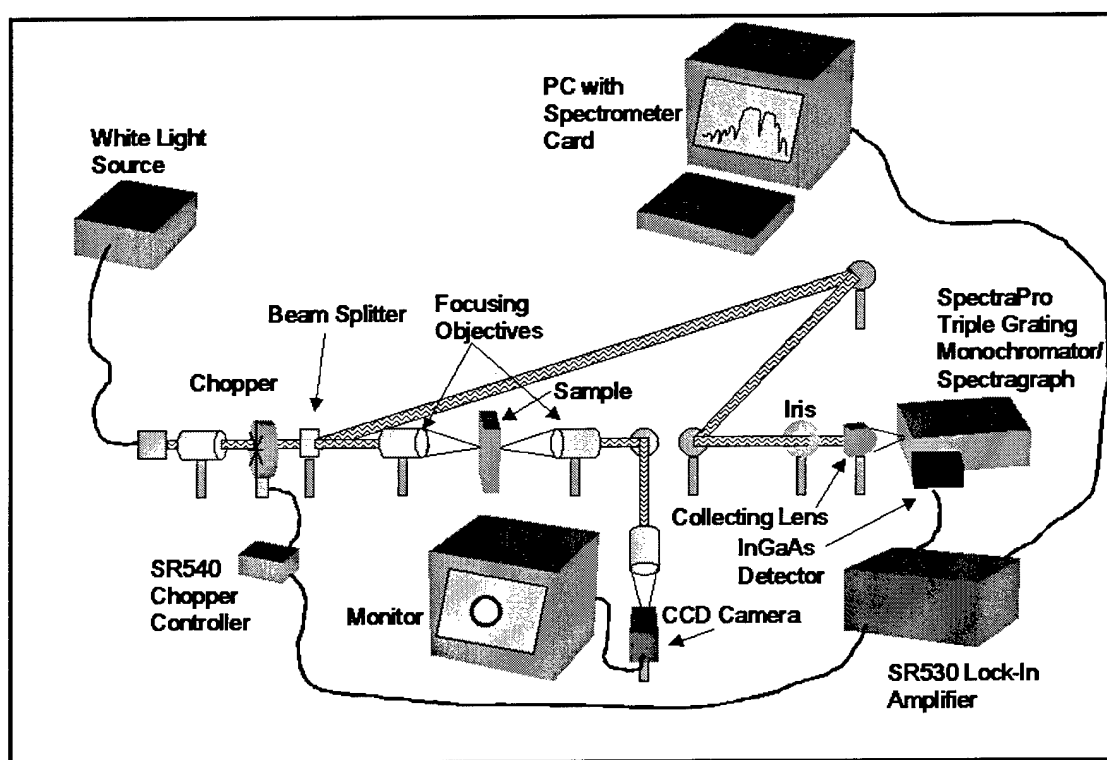


Figure 4.11 Schematic of small-spot reflectance measurement system.

4.7 Focused Ion Beam Scanning Electron Microscope System

I utilized AFRL's FEI 620 dual beam workstation to investigate the effects of oxidation-induced stress, delamination of oxidized layers, and overall growth layer uniformity. The system combines the milling capabilities of a focused ion beam (FIB) with the imaging capabilities of a

scanning electron microscope (SEM). This dual-chamber (FIB/SEM) approach is used to image a portion of the sample and then selectively mill (or remove) a portion of a selected sample feature. The system uses a gallium ion beam to bombard the sample surface. Etch depth and speed are determined using variable current settings. Figure 4.12 shows a photograph of the AFRL FIB/SEM system. This system also has the ability to deposit platinum over patterned features to allow for area protection during the milling process.

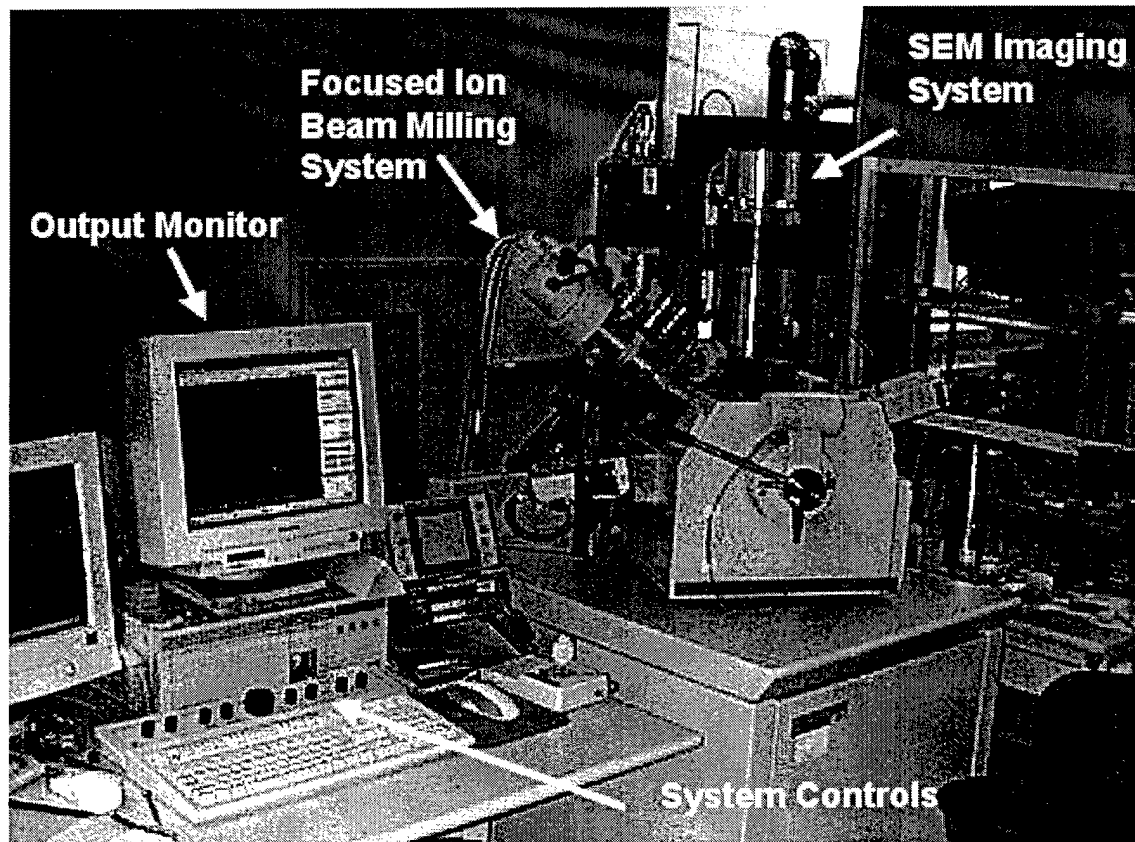


Figure 4.12 Photograph of AFRL FEI 620 dual beam FIB/SEM workstation

4.8 Selective Etching Techniques

Microelectromechanical systems (MEMS) are integrated electrical and mechanical systems on a microscopic scale. Silicon MEMS technology has found a wide range of uses in the automotive [14], medical [16], and aerospace [42] industries. Systems utilizing III-V compound material

MEMS technology have also found applications in the fields of mechanical engineering, microwave electronics, and optical communication systems [22]. Most of these systems are created using a bulk-micromachining process where areas of the top-layer material are removed through wet chemical etching or by reactive ion etching. A primary reason for the success and proliferation of silicon MEMS is the ability to grow a sacrificial layer that can be selectively removed during processing. It would be highly beneficial to incorporate such a layer in a monolithically grown VCSEL device. This selective removal of a layer will allow for applications such as tunable VCSEL lasers to become more manufacturable and robust [46]. Several chemicals were evaluated for their ability to selectively remove AlO layers from a monolithically grown structure, including: buffered oxide etch (BOE), AZ400K developer, and a solution of hydrofluoric acid and deionized (DI) H_2O . Each sample was placed in the etchant for a predetermined amount of time and then thoroughly rinsed using DI H_2O . The results of these studies are discussed and analyzed in Chapter 5.

4.9 Chapter 4 Summary

In this chapter I explained the techniques, equipment, and procedures I used to process and characterize microcavity test structures containing selectively oxidized AlAs layers. An overview of the fabrication steps was given along with a look at the optical bench setup used to measure and record power reflectance data. In Chapter 5 I analyze the results obtained through the use of this experimental equipment and experimental techniques.

5. Results and Analysis

5.1 Introduction

In this chapter I present and analyze the results of my laboratory experiments on oxidized AlAs and $Al_xGa_{1-x}As$ for multilayer device applications. I report the first results of large mesa ($> 100\mu m$) oxidation runs in the custom-built AFRL oxidation system [18]. I explain the methods and procedures I used to calculate a new dispersion file for native oxide material layers as processed in the AFRL laboratory. Finally, I analyze the results of my selective oxide native aluminum etch study.

5.2 Initial Experiments

"You wouldn't abandon a ship in a storm just because you couldn't control the winds"
-Sir Thomas Moore

As the quote suggests, there are sometimes forces which are beyond your control. Unfortunately there were several periods of time during my thesis where one or more pieces of vital equipment were non-operable due to mechanical failures. I briefly explain the processing steps I took to overcome these obstacles and the lessons I learned from each step.

Initial problems with the MBE system delayed my ability to have samples grown in the AFRL clean room. I examined current sample inventory to determine if there were suitable samples already grown which could be used for test and evaluation of the oxide system. I ran simulations on the existing DBR and microcavity wafer inventory to determine if any of the samples were viable for native oxide layer experimentation and examination. MATLAB simulations of the existing inventory can be found in Appendix C, Section C.1. These simulations were used to evaluate the effect of oxidation on several different types of structures (e.g. DBRs, etalons, etc.). The turbo pump on the inductively coupled plasma (ICP) etching system was also down due to mechanical failures. Thus I started by experimental research on non-optimal test structures.

5.2.1 *Wet Chemical Mesa Definition Etch Study.* I analyzed AFRL sample G2-2612 (see Table 5.1) for wet chemical etching alternatives to the plasma etching system for the purpose of mesa definition. The sample was processed using standard lithography and photoresist techniques (see Appendix A). I then cleaved the sample and etched each smaller piece as shown in Table 5.2.

Table 5.1 Layer structure for AFRL Sample G2-2612 (Etalon with $\frac{3\lambda}{2}$ -thick AlAs microcavity)

Layer (Starting at Sub)	Doping	Thickness (\AA)	Note
Gas	(u)	∞	Substrate
AlAs	(u)	837	/-GaAs/AlAs DBR, Repeat—
GaAs	(u)	696	—12 Times—/
AlAs	(u)	5026	AlAs microcavity
GaAs	(u)	696	/-GaAs/AlAs DBR, Repeat—
AlAs	(u)	837	—10 Times—/
GaAs	(u)	696	Extra $\frac{\lambda}{4}$ layer

Table 5.2 Etchants used in wet chemical mesa definition study on AFRL sample G2-2612)

Piece Id	Etchant	Solution Ratio	Etch Time min:sec	Rinse
G2-2612C1	$H_2SO_4:H_2O_2:H_2O$	1:1:10	1:45	30 sec DI H_2O
G2-2612C2	$C_6H_8O_7H_2O:H_2O_2:H_2O$	10:1	10:30	30 sec DI H_2O
G2-2612C3	$C_6H_8O_7H_2O:H_2O_2:H_2O$	10:1	20:00	30 sec DI H_2O
G2-2612C4	$H_2SO_4:H_2O_2:H_2O$	1:1:10	3:00	30 sec DI H_2O (24 hour delay)

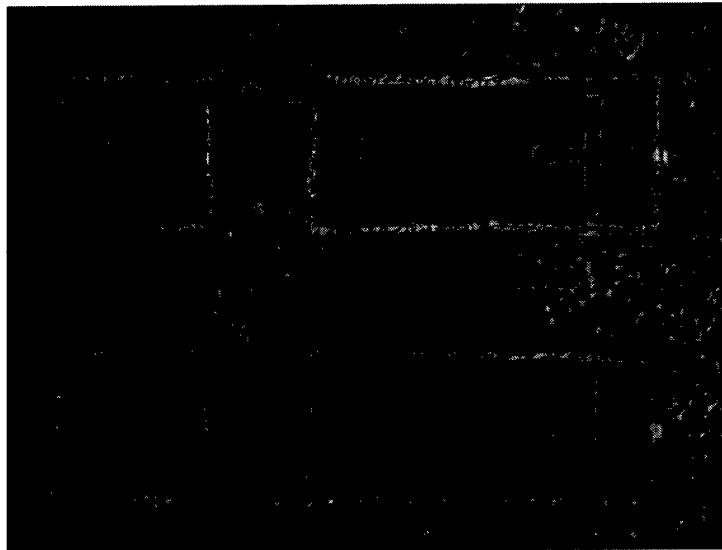
Results of the study varied from overly aggressive etchants which attacked the mask layer (MicroPosit 1818 photoresist) to etchants which failed to properly define the mesa structures. The first mixture of sulfuric (H_2SO_4), hydrogen peroxide (H_2O_2), and DI water mixture (for sample G2-2612C1) was tested one hour after chemical mixing. The etch proved to be too aggressive. Profilometry of the sample showed an extremely rough surface on the material backplane and noticeable degradation of the resist masking layer as the etched progressed. The results of the sulfuric acid solution etch are shown in Figure 5.1. I used profilometry to measure the step height and from the etch time deduced an etch rate of $22 \frac{nm}{sec}$.

The citric acid ($C_6H_8O_7H_2O$), hydrogen peroxide (H_2O_2), and water mixture (for samples G2-2612C2 and G2-21612C3) was observed to pit the wafer surface without noticeable etch mask

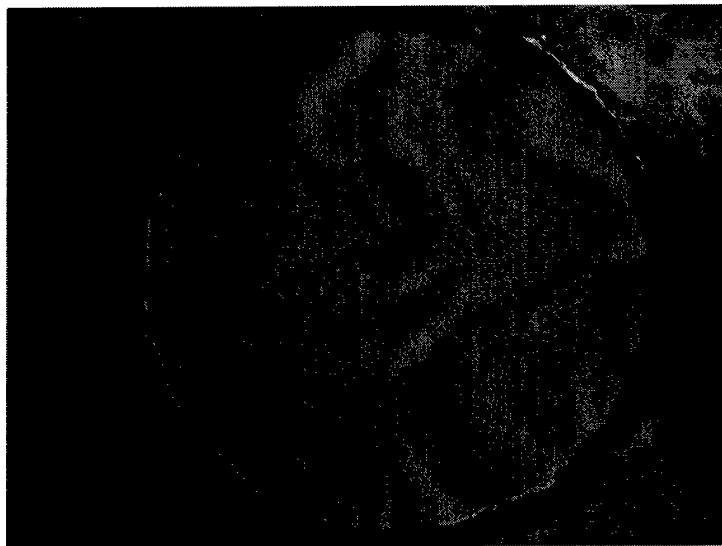
material degradation. I deduced an etch rate of $2.9 \frac{nm}{sec}$. Photographs of surface pitting for this sample are shown in Figure 5.2. The sulfuric acid solution etch was repeated after letting the solution sit for 4 hours. Dramatically improved results in surface uniformity and mask layer degradation were observed. I observed little to no degradation of the resist layer wafer uniformity. I determined an etch rate of $24.3 \frac{\mu m}{sec}$ for the sulfuric acid. Microscope images for AFRL sample G2-2612C4 are shown in Figure 5.3.

5.2.2 Initial Oxidation System Evaluation. I followed the wet etching study with an evaluation of the oxidation system. I completed trial runs to determine if large area mesa structures (diameter $> 135\mu m$) could be successfully completely oxidized using the custom built AFRL oxidation system. This is a first attempt to completely oxidize large area DBR and micocavity test structures.

The first sample analyzed (G2 - 2477) (see Table 3.3) was a 28-period DBR structure used in optical delay line research. The sample was patterned as shown in Figure 5.4a. Oxidation of this structure was inhibited by the gold contact ring deposited on the structure. The gold contact ring was removed by dipping the sample in TechnoStrip for 6 minutes followed by a 3 minute BOE (7:1 $NH_4F : HF$) etch. The sample with gold removed is shown in Figure 5.4b. I used the Tencor P-10 profilometer to determine that the surface of the mesa was flat and uniform after the metal strip. Attempts to oxidize this sample were unsuccessful as shown in Figure 5.5. Microscope images of the sample show non-uniform oxidation phase fronts as well as delamination effects due to volumetric layer shrinking as a result of the oxidation of the AlAs layers. Chemical processing to remove the gold contacts and possibly native oxide due to ambient oxide growth besmirched the oxidation process and led to poor overall results. The use of Technostrip to remove the gold contact ring may have passivated mesa sidewalls. Passivation would lead to uneven oxidation front progression rates.

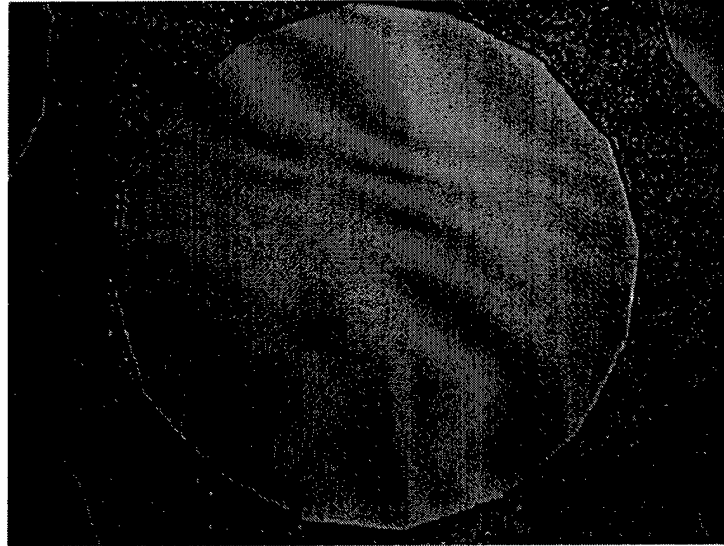


(a)

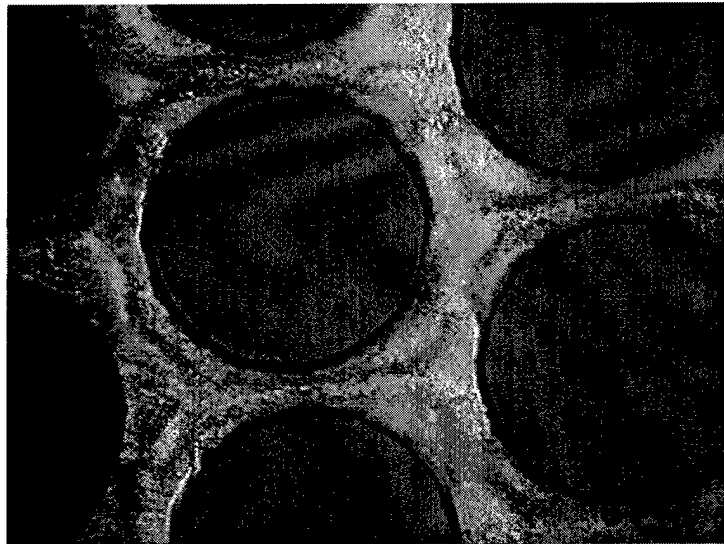


(b)

Figure 5.1 Microscope images of AFRL sample *G2 - 2612C1* showing (a) sample etched for 1:15 min in a sulfuric acid solution and (b) the same sample after 1:45 min sulfuric acid solution etch. The figure shows surface roughness and resist degradation as a result of sulfuric acid solution etch

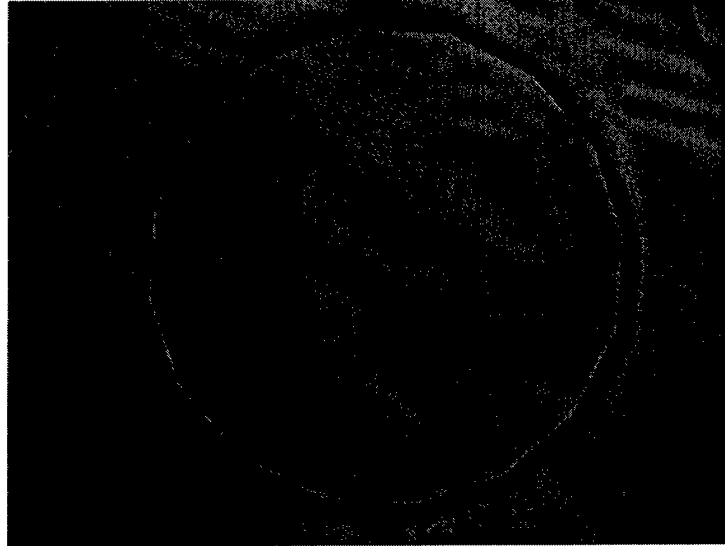


(a)

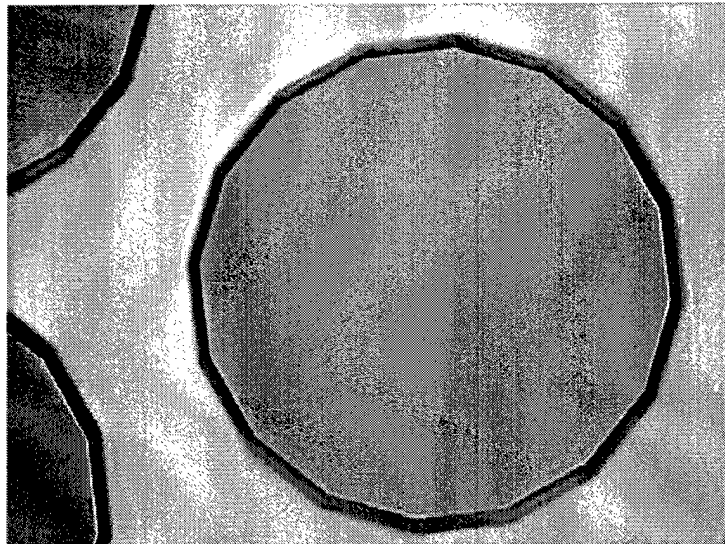


(b)

Figure 5.2 Microscope images of samples *G2 - 2612C2* and *G2 - 2612C3* after citric acid etch. The figure shows (a) sample etched for 10:30 min in citric acid solution and (b) same sample after 20:00 min citric acid solution etch. Surface pitting as a result of the citric acid etch is clearly visible.

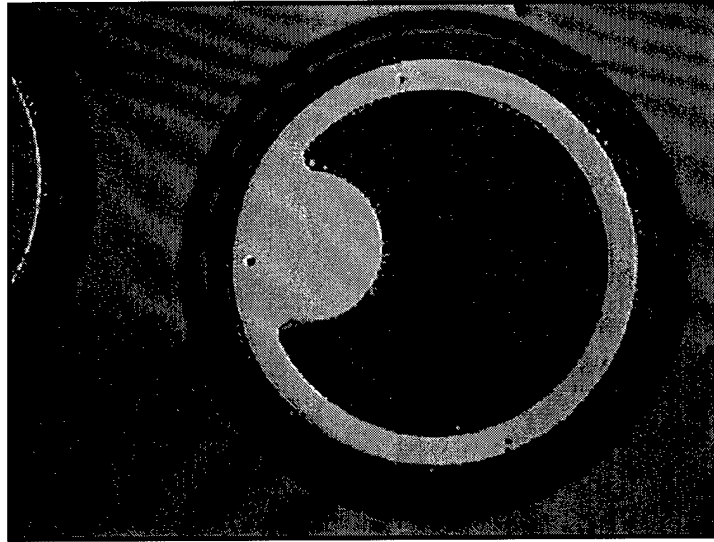


(a)

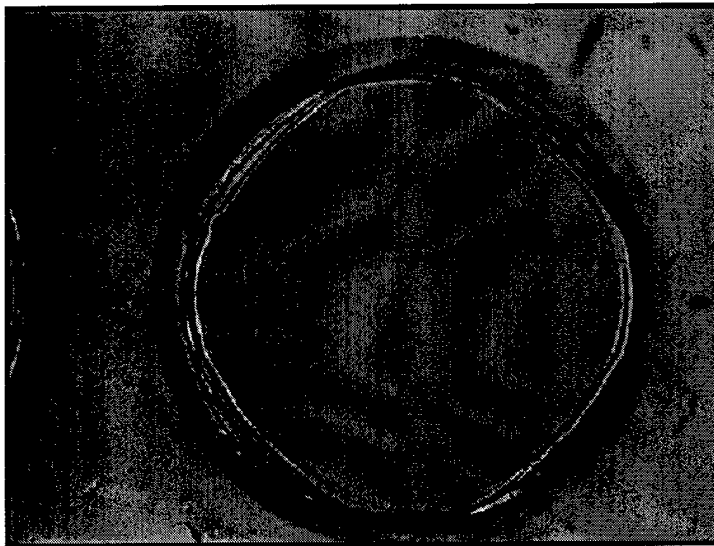


(b)

Figure 5.3 Microscope images of AFRL sample *G2 - 2612C4* after sulfuric acid solution etch. The figure shows (a) sample after 3:00 min sulfuric acid solution etch and (b) large area mesa after complete oxidation of AIAs DBR and microcavity layers.

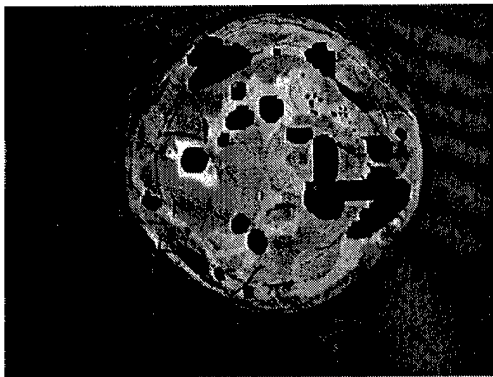


(a)

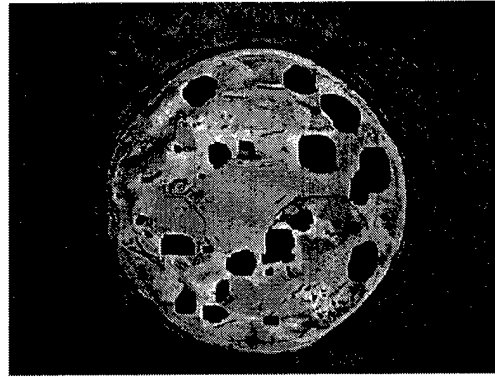


(b)

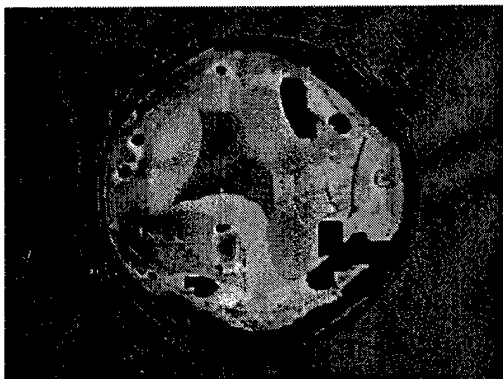
Figure 5.4 Microscope images of AFRL sample G2-2477 (28-period DBR) with (a) gold contact ring and (b) Metal contact ring removed via Technostrip and BOE etch.



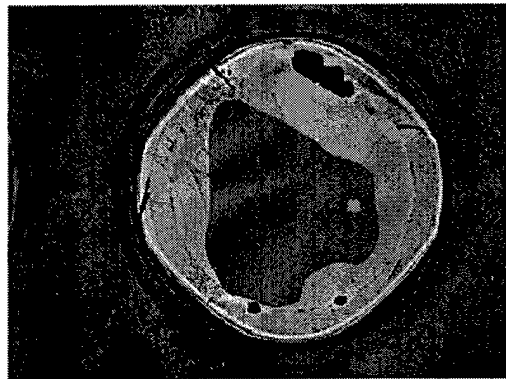
(a)



(b)



(c)



(d)

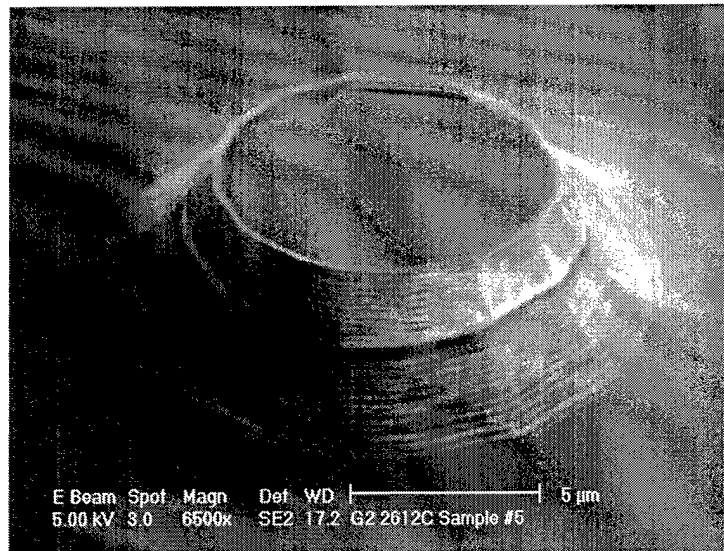
Figure 5.5 Microscope images of AFRL sample *G2* – 2477 (28-period DBR) after oxidation. Figure shows: (a) complete oxidation of mesa showing debris and delamination; (b) complete oxidation of mesa also showing debris and delamination; (c) partial oxidation of mesa structure displaying phase front non-uniformity and delamination effects; and (d) incomplete oxidation showing similar effects as in (a), (b), and (c).

I then completely oxidized AFRL sample $G2 - 2612C4$ (see Table 4.1 for run specifics; note: the sample was cleaved into several pieces for processing. Sample $G2 - 2612C4$ refers to piece 4 from quarter-wafer section C taken from whole 3" wafer grown during MBE growth run G2-2612). When I partitioned the sample into further pieces, an extension of i, ii, iii, etc. was used to differentiate the pieces (e.g. 2612C4i). Figure 5.3b displays a microscope image of the sample after oxidation. I evaluated the structures further using the FEI 620 dual beam focused ion beam (FIB)/scanning electron microscope(SEM) workstation.

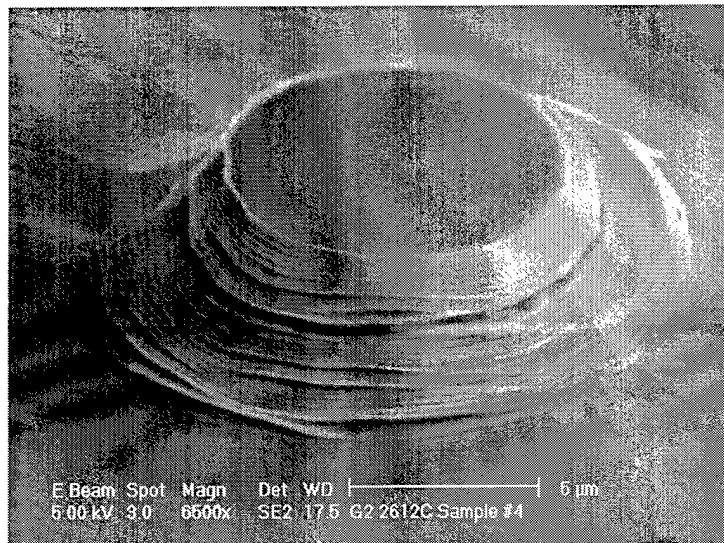
I compared a non-oxidized sample ($G2 - 2612C5$) to the completely oxidized sample ($G2 - 2612C4$). Figure 5.6 shows the two samples and the resultant layer delamination as the AlAs layer undergoes volumetric shrinkage due to the oxidation process. I also investigated the extent of the delamination effects by using the FIB system to mill away a portion of the large area mesas. Figure 5.7 shows a reduction in overall delamination effects towards the center of the device. This information proved critical in further measurements when layer uniformity (or lack of delamination) is assumed.

5.3 Sample Growth and Analysis

Next, I designed and grew several samples for the purpose of extracting the index of refraction for native aluminum oxide. The design process includes several molecular beam epitaxy (MBE) runs to properly calibrate the Varian Gen II MBE system. I designed and grew the first structure to calibrate proper flux- and growth-rates for an epitaxially grown GaAs/AlAs etalon structure designed for a λ_{Bragg} equal to 980nm. The structure (G2-2651) was designed to have a 12 period AlAs/GaAs bottom DBR, a 3λ -thick AlAs microcavity region, and a 10.5 period GaAs/AlAs top DBR. Physical thickness target values are shown in Table 3.1. Calculated reflectance, transmittance, and absorptance values as a function of wavelength are shown in Figure 3.1, Figure 3.2, and Figure 3.3 respectively. The data was fit using both AFRL's fitting technique [34] and work

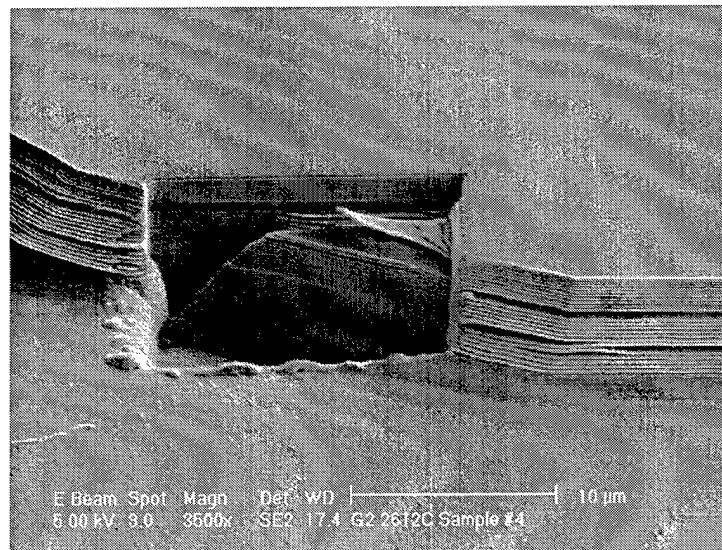


(a)



(b)

Figure 5.6 SEM micrographs of AFRL sample *G2 – 2612C5* and AFRL sample *G2 – 2612C4*. The figure shows (a) non-oxidized structure where the AlAs microcavity is clearly visible as the dark contrast in the center region; (b) shows the completely oxidized structure and the effects of delamination due to stress induced from volumetric shrinkage of the AlAs layers as a result of the oxidation process. The sample *G2-2612* is a Fabry-Perot etalon composed of AlAs/GaAs DBRs surrounding a 1λ microcavity.



(a)



(b)

Figure 5.7 SEM micrographs of AFRL sample G2 – 2612 (#4 and #5) after FIB milling. Figure shows: (a) Selective removal of mesa material using FIB milling system and (b) Shows magnified in view of milled area from (a). Layers show signs of contractive stress due to volumetric layers shrinkage as a result of the oxidation process. Interior layer uniformity is preserved despite outer-edge delamination and curling due to layer stress. The sample G2-2612 is a Fabry-Perot etalon composed of AlAs/GaAs DBRs surrounding a 1λ microcavity.

completed using *FilmWizard*[®]. Figure 5.8 shows measured data taken from the in-situ MBE reflectometry system. Figure 5.9 compares measured data to initial calculated power reflectance values. Finally, Figure 5.10 shows improved fit to measured data after completing regression analysis. Adjusted layer thickness values are shown in Table 5.3. I used these values in conjunction with actual MBE growth times to properly calibrate MBE growth rates.

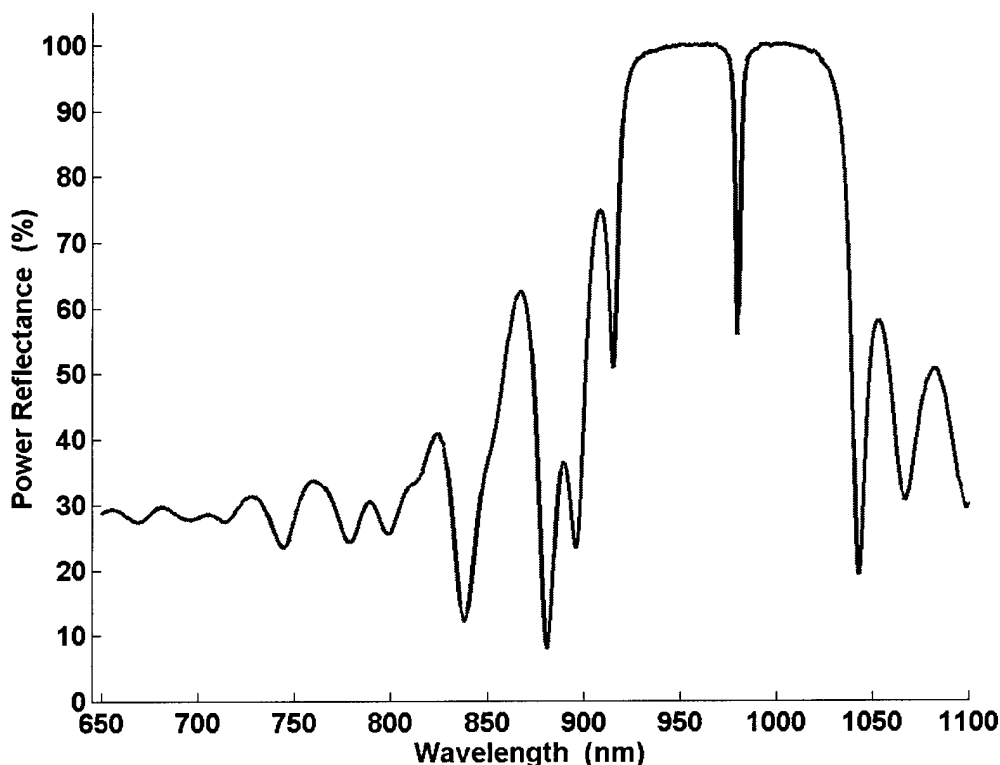


Figure 5.8 Measured MBE reflectometry system power reflectance for AFRL sample *G2* – 2651 (etalon structure with GaAs/AlAs DBR layers and a 3λ -thick AlAs microcavity)

After completing the system calibration, I designed and grew AFRL sample *G2* – 2652 (see Table 3.5). I designed the structure to resonate light at 980nm. The microcavity region is composed of a 2λ -thick GaAs layer. The DBR layers are composed of GaAs/AlAs layers. The sample was grown and I measured power reflectance using the MBE reflectometry system. An excellent fit to the measured data was again obtained through regression analysis. The *FilmWizard*[®] regression

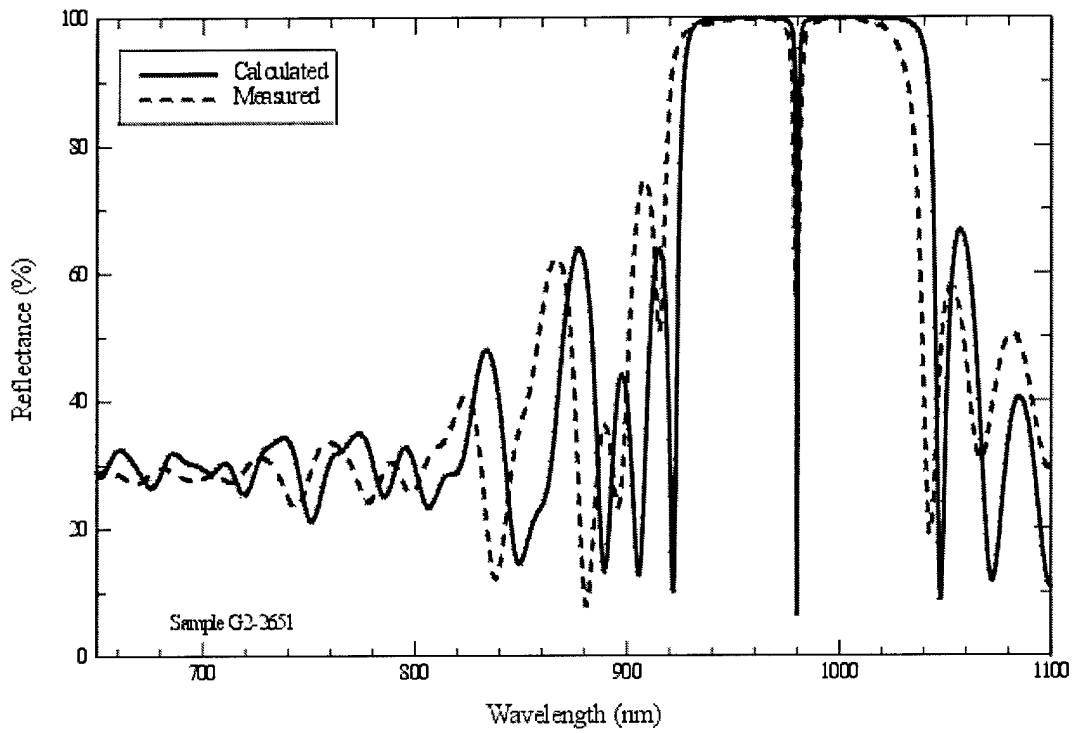


Figure 5.9 Measured MBE reflectometry system power reflectance for AFRL sample *G2 - 2651* compared to initial calculated power reflectance values. (etalon structure with GaAs/AlAs DBR layers and a 3λ -thick AlAs microcavity).

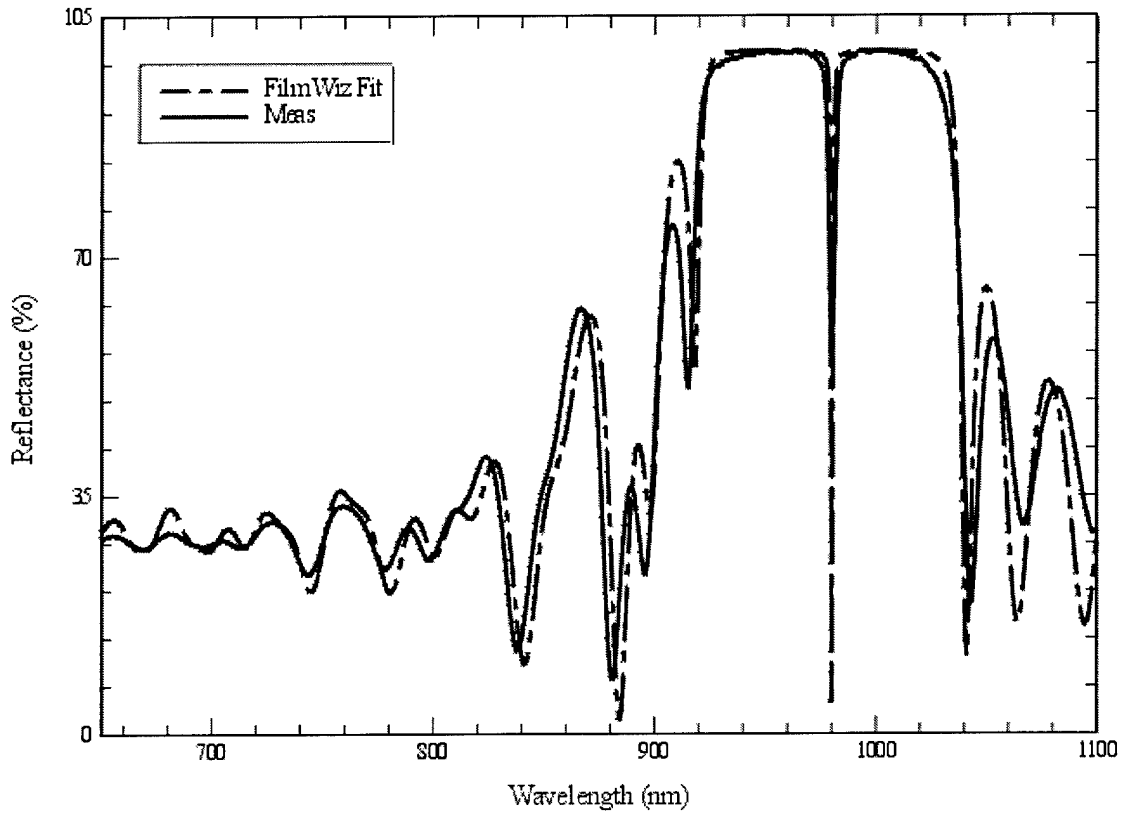


Figure 5.10 Measured MBE reflectometry system power reflectance for AFRL sample G2-2651 (etalon structure with GaAs/AlAs DBR layers and a 3λ -thick AlAs microcavity) compared to calculated power reflectance values after adjusting layers via regression analysis fitting technique.

Table 5.3 Pre- and Post-Regression Analysis Thickness Values (Sample *G2* – 2651)

Layer	Original Thickness (Å)	Post-Regression Thickness (AFRL)(Å)	Post-Regression Thickness (FilmWiz)(Å)
GaAs Sub	∞	∞	∞
AlAs	838	845	853
GaAs	696	672	679
AlAs	10053	10150	10150
GaAs	696	672	682
AlAs	838	845	821
GaAs	696	672	699

analysis software proved to be more robust than the existing AFRL fitting program because of its ability to independently vary each layer thickness value. AFRL's algorithm can only vary each type of layer (e.g. all $\frac{1}{4}$ -wave layers of a particular material are varied simultaneously) Pre- and post-regression layer thickness values are shown in Table 5.4. Figure 5.11 shows the results of regression analysis as simulated using values from Table 5.4.

Table 5.4 Pre- and Post-Regression Analysis Thickness Values (Sample *G2* – 2652, etalon structure with a 2λ -thick GaAs microcavity)

Layer	Original Thickness (Å)	Post-Regression Thickness (AFRL)(Å)	Post-Regression Thickness (FilmWiz)(Å)
GaAs Sub	∞	∞	∞
AlAs	838	806	831
GaAs	696	696	685
AlAs	838	806	837
GaAs	5568	5567	5532
AlAs	838	806	793
GaAs	696	696	696

5.4 Aluminum Oxide Refractive Index Values

Next, I patterned samples (*G2* – 2651 and *G2* – 2652) to define mesa structures and expose layers for oxidation. I then completely oxidized (see Table 4.1 for details) both samples. I was unable to take reflection measurements on AFRL sample *G2* – 2651 due to the deleterious effects of oxidizing the large AlAs (3λ -thick @ 980nm) microcavity. Figure 5.12 shows microscope images

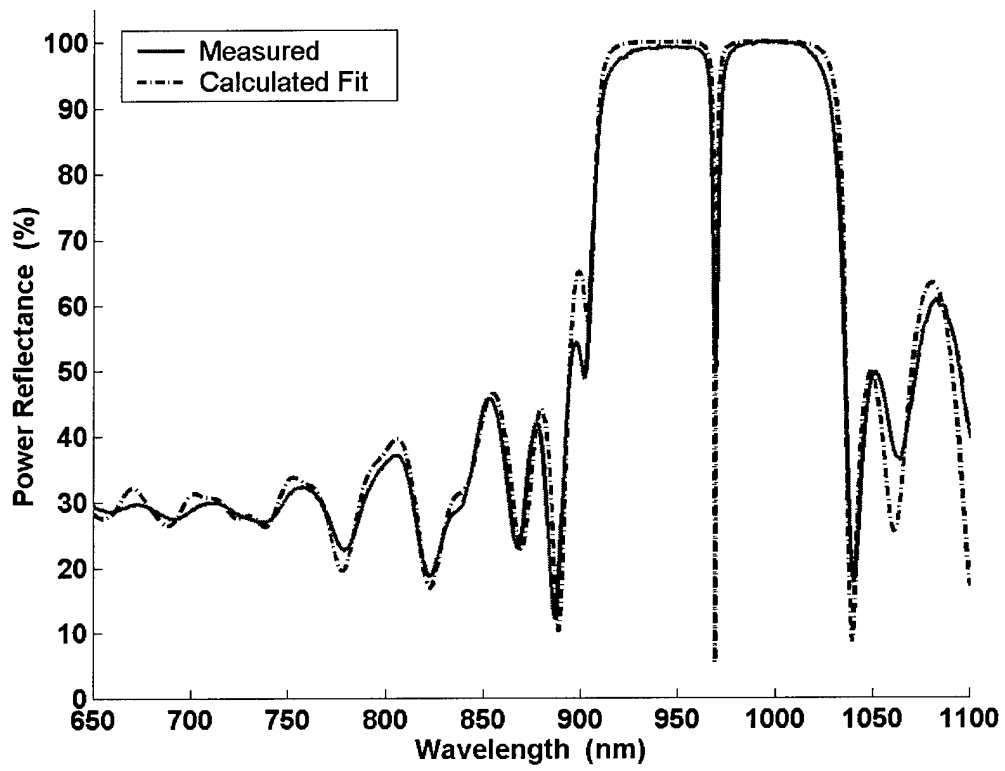


Figure 5.11 Measured power reflectance and calculated power reflectance after regression fit for AFRL sample G2 – 2652 (2λ -thick GaAs microcavity etalon).

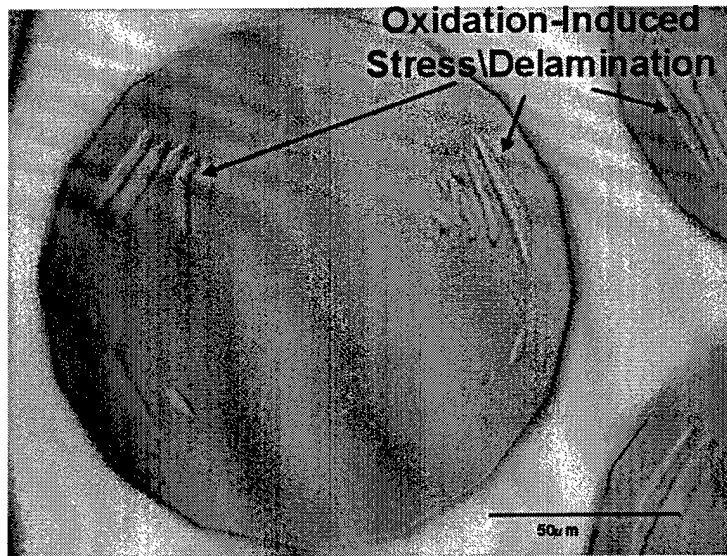
of the damage caused to structures as a result of volumetric layer shrinkage. I explored the damage further utilizing the FIB/SEM system. Figure 5.13 displays micrographs of the layer delamination.

Power reflectance measurements were taken on AFRL sample *G2* – 2652 after oxidation (see setup Section 4.6). Measured data is shown in Figure 5.14. Profilometry was used to determine layer shrinkage in the 1λ -thick $Al_{0.98}Ga_{0.02}As$ cavity in AFRL sample *G2* – 2658. Mesa heights were using the Tencor P-10 profilometer. I cleaved a small piece from the sample and measured the same mesas for both pre- and post-oxidation step-heights. Measurements were taken in the center region of the large area mesas where all of the volumetric layer shrinkage can be attributed to the change in layer thickness of the $Al_{0.98}Ga_{0.02}As$ microcavity layer ($Al_{0.9}Ga_{0.1}As$ mirror layers oxidized to some extent $\sim 10\mu m$). The pre- and post-oxidation step-heights are listed in Table 5.5. My experimentally determined value for layer shrinkage of -6.2% is in agreement with previously conducted research [51].

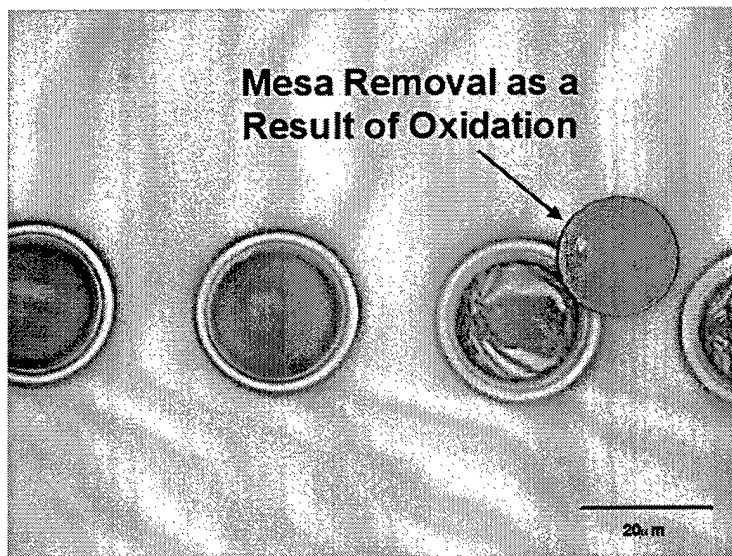
Table 5.5 Pre- and Post-Oxidation Step-Height Measurements (Sample *G2* – 2658)

Meas Number	Pre-Ox Step Height (μm)	Post-Ox Step Height (μm)	Diff (\AA)	% Change
1	4.250	4.211	390	-6.7
2	4.269	4.231	-380	-6.5
3	4.192	4.162	-300	-5.1
4	4.332	4.293	-390	-6.7
5	4.259	4.227	-320	-5.5
6	4.234	4.198	-360	-6.2
7	4.219	4.178	-410	-7.0
			Avg % Change	-6.2

The measured data was used with previously calculated layer thickness values (adjusted for volumetric shrinkage) to extract index of refraction values. I used the regression analysis tool in the *FilmWizard*[®] software package to minimize the root mean square error (RMSE) between model parameters and measured data. I used a parametric Cauchy fit to model index values. The Cauchy dispersion relation describes the index of refraction for transparent materials. It is assumed that AlO layers are transparent over my region of interest (650nm-1100nm) and longer wavelengths. That is to say that the imaginary part of the index of refraction, k , equals zero over this wavelength

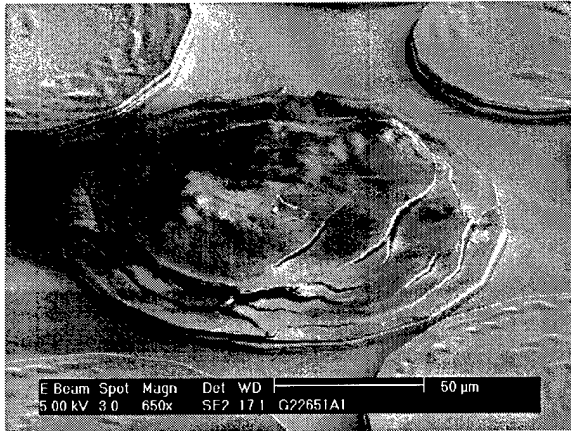


(a)

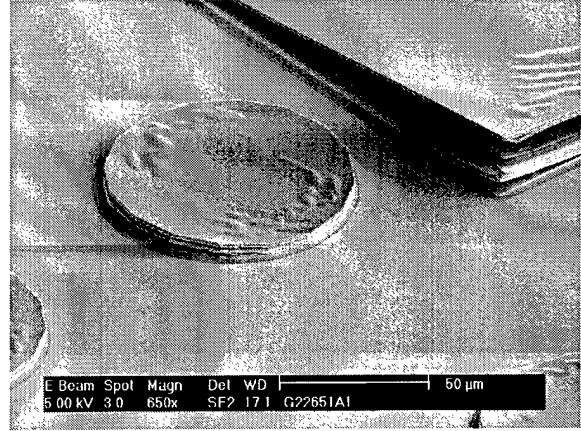


(b)

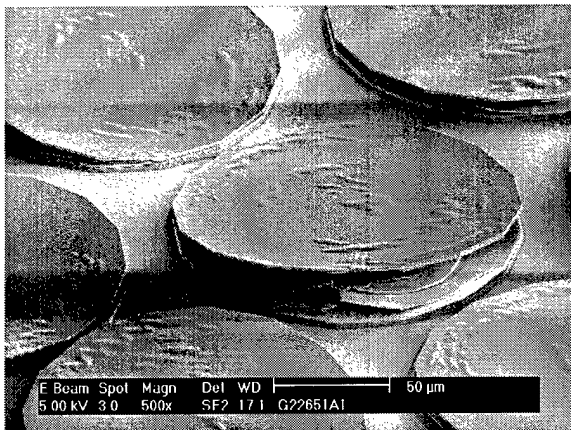
Figure 5.12 Post-oxidation microscope images of AFRL sample G2 – 2651 showing deleterious effects of layer shrinkage (3λ -thick AlAs microcavity etalon).



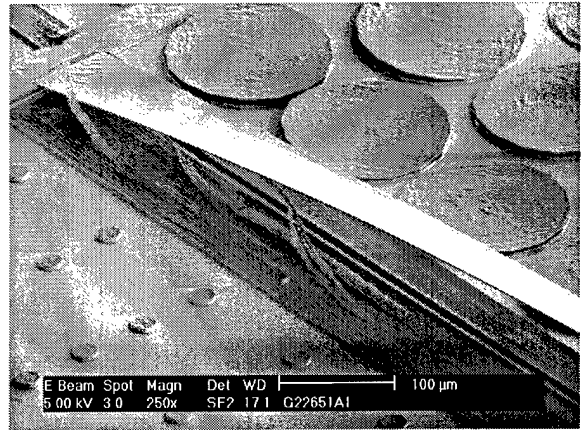
(a)



(b)



(c)



(d)

Figure 5.13 Post-oxidation micrographs of AFRL sample G2 – 2651 showing induced stress and layer delamination as a result of the oxidation process (3λ -thick AlAs microcavity etalon).

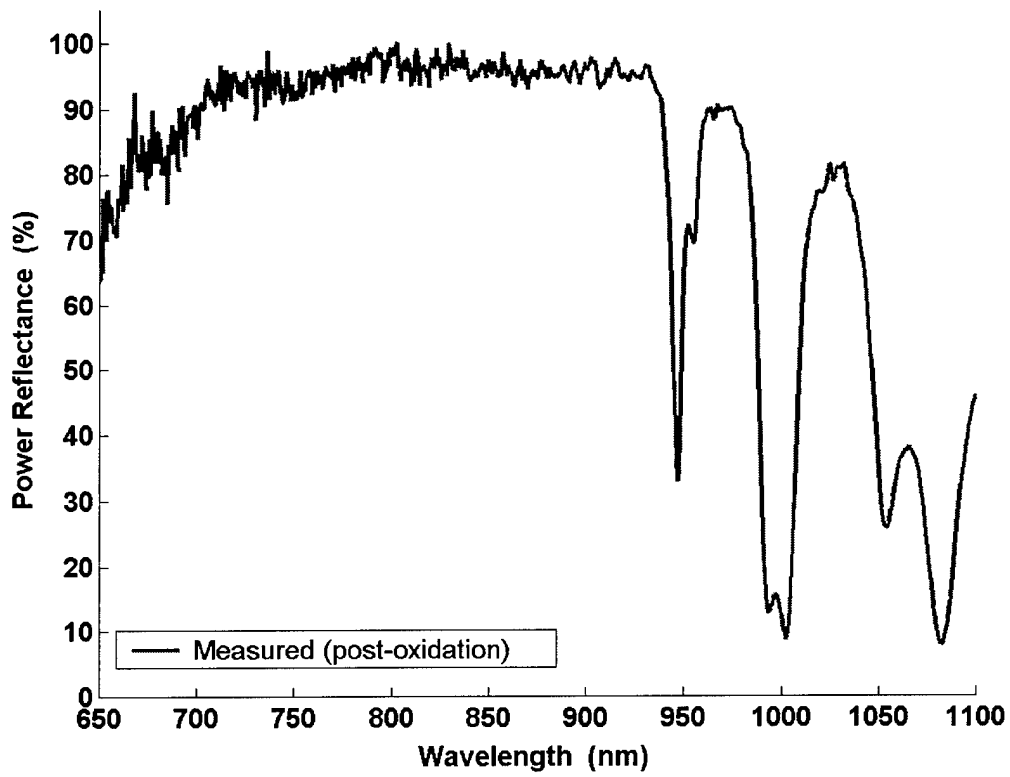


Figure 5.14 Measured post-oxidation power reflectance spectrum for AFRL sample G2 - 2652 (2λ -thick GaAs microcavity etalon).

range. The refractive index as a function of wavelength, $n(\lambda_o)$, was extracted and fit using Cauchy parameters in the form [23]

$$n(\lambda_o) = A_n + \frac{10^6 B_n}{\lambda_o^2} + \frac{10^{12} C_n}{\lambda_o^4} \quad (5.1)$$

where λ_o is wavelength in nm. A minimum RMSE of 14.23 was found for the following Cauchy coefficients of $A_n = 1.683$, $B_n = .00294$, $C_n = .000834$.

A plot of the resultant index of refraction for AlO a function of wavelength is shown in Figure 5.15. Values are extrapolated for longer wavelengths, as is allowed by the assumption of transparency. Figure 5.16 compares my calculated values with the values currently used by AFRL to model oxide-layer containing microcavity structures. [29].

The post-oxidation power reflectance data for AFRL sample *G2-2658* (1λ -thick $Al_{0.98}Ga_{0.02}As$ cavity, with bottom GaAs/ $Al_{0.90}Ga_{0.10}As$ DBR layers and a 1.5 period GaAs/ $Al_{0.90}Ga_{0.10}As$ DBR) is shown in Figure 5.17. Visual inspection shows the improved fit to measured data. Calculated RMSE values also dropped from 32.44 for the previous dispersion file to 16.57 for my extracted Cauchy parameter model.

5.5 Selective Etching of Oxidized Layers

The field of III-V MEMS is growing as the demand for micro-optical systems increases. The design possibilities for tunable VCSEL devices are endless [7]. A key step in the manufacturing of such a tunable device is the ability to selectively remove layers for an air gap to create a microcavity that is selectively tuned to a desired wavelength. Figure 5.18 shows the power reflectance for a tunable filter device. The structure is composed of top and bottom GaAs/AlAs DBRs with a tunable air gap in between. Location of the Fabry-Perot dip is obtained by modulation of the air gap distance [46]. A necessary step in the design of such a device is the ability to selectively remove

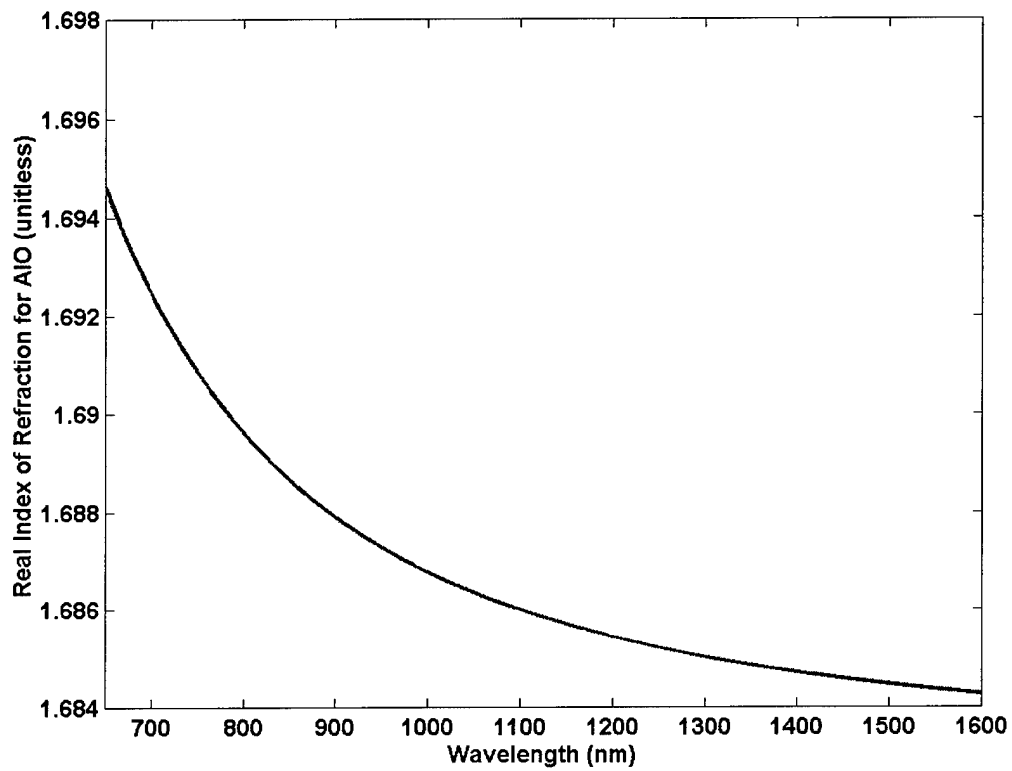


Figure 5.15 Index of refraction for aluminum oxide converted through oxidation in the AFRL custom-built oxidation system @ 400°C.

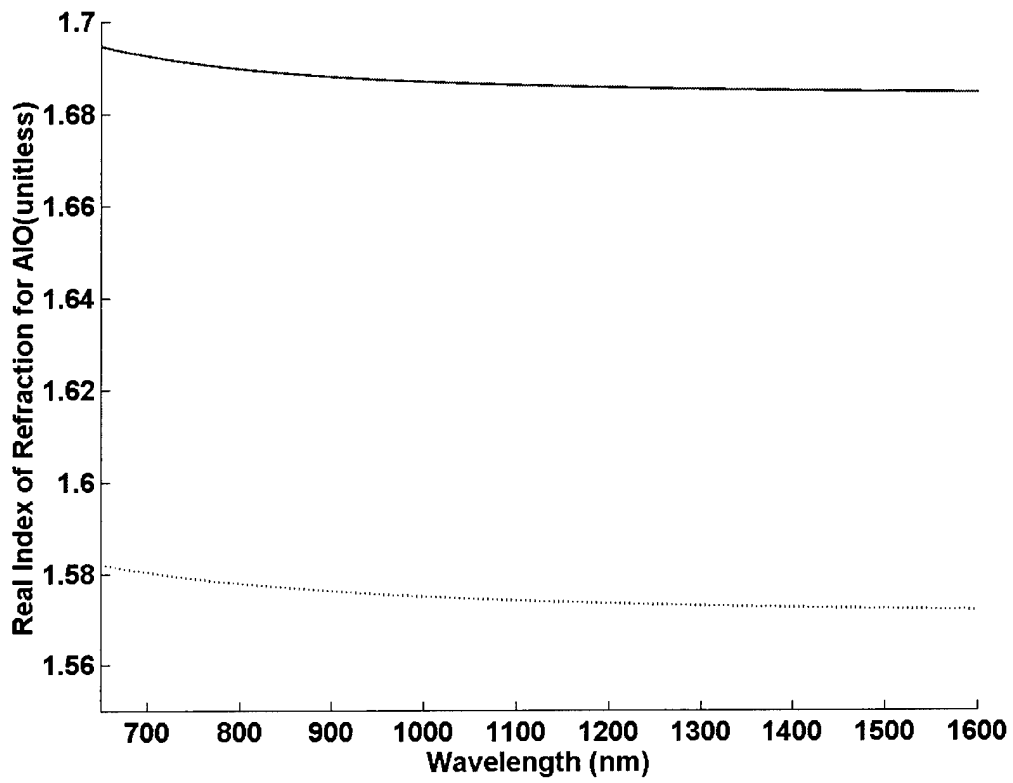


Figure 5.16 Comparison of previous AFRL AIO (dotted line) dispersion file and my extracted Cauchy parameter fit model (solid line) to measured data.

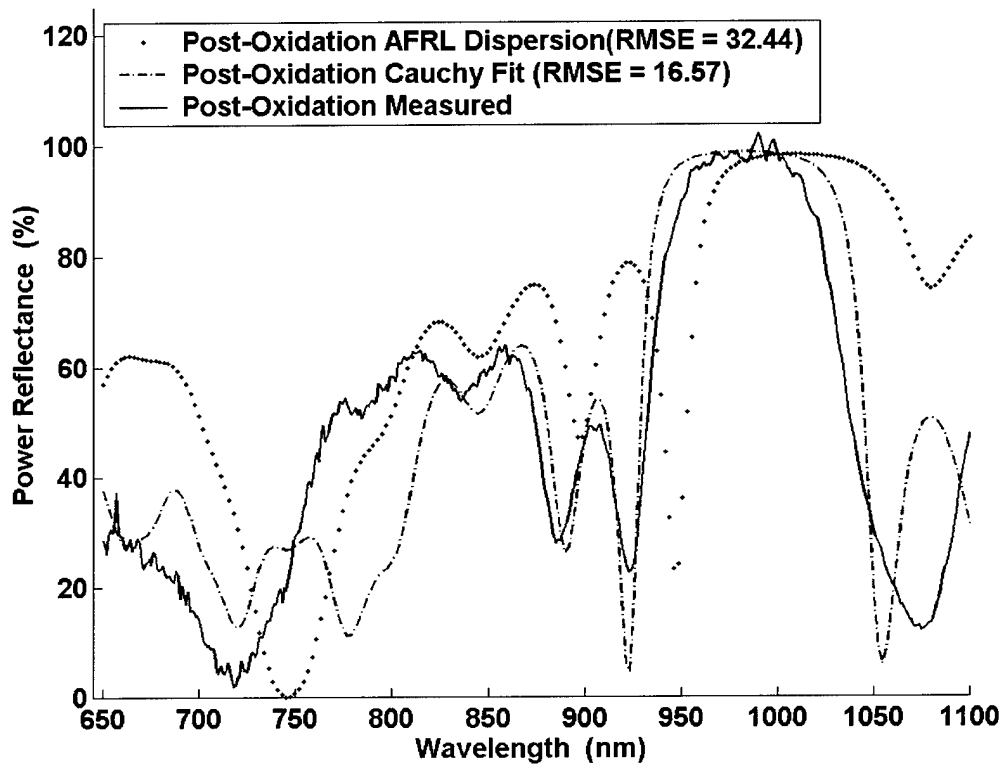


Figure 5.17 Comparison of calculated reflectance spectrum for AFRL sample 2658 to measured data. The figure shows a comparison of reflectance calculations between a model using my extracted Cauchy parameter fit and one calculated using the previous AFRL dispersion curve [29].

material to create the tuning mechanism. I investigated the possibility of using converted AlO layers as a sacrificial layer in a III-V MEMS process. I evaluated the ability of several etchants to selectively remove converted AlO layers. Etchants evaluated are listed in Table 5.6.

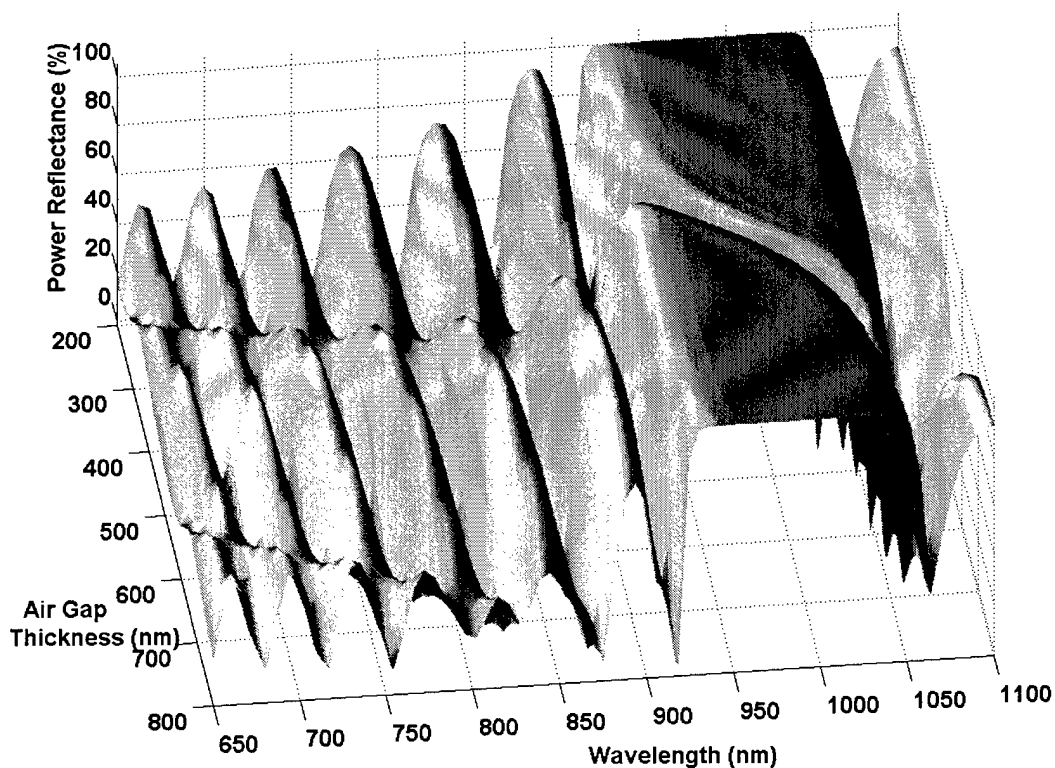


Figure 5.18 Example of tunable etalon structure designed around a central Bragg wavelength of 980nm. Modulation of the air gap inside the microcavity shifts the location of the Fabry-Perot dip as a function of air gap thickness.

The preferred etchant for the selective removal of AlO layers was determined to be BOE. The HF:H₂O solution ratio I chose proved to be too aggressive while the AZ400K developer solution had no observable removal of the AlO layers. I evaluated all of the samples on the FIB/SEM system. The results of the aggressive HF:H₂O etch is shown in Figure 5.19. Entire microcavity structures were removed from the substrate (GaAs) as a result of the etch. Figure 5.20 shows the dramatic effect of the HF-solution etch. While this was not the desired outcome of the experiment, the figure shows how the aggressive nature of the HF:H₂O solution could potentially be used to remove

Table 5.6 Etchants Evaluated for their Ability to Selectively Etch AlO Sacrificial Layers

Piece Id	Etchant	Solution Ratio	Etch Time min:sec	Rinse
G2-2652A3i	BOE	Not Diluted	0:30	30 sec DI H_2O
G2-2652A3ii	HF: H_2O	2:10	0:30	30 sec DI H_2O
G2-2652A3iii	AZ400K Developer (KOH)	Not Diluted	0:30	30 sec DI H_2O
G2-2652A3iv	AZ400K Developer (KOH)	Not Diluted	0:60	30 sec DI H_2O

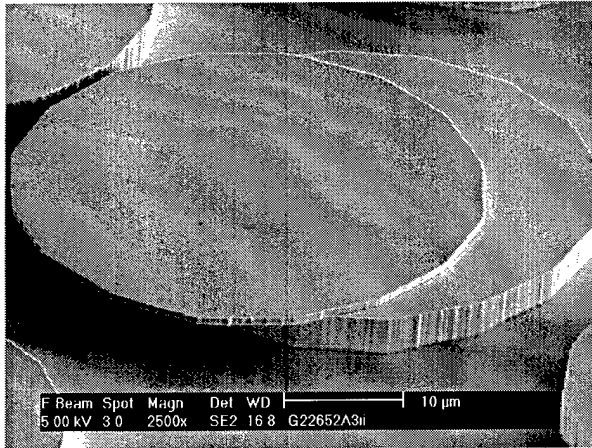
etalon, or VCSEL, structures from the substrate. The removed microcavity structures could then be integrated onto a tiltable silicon MEMS structure to create a tiltable III-IV-V MEMS laser. Results of the AZ400K developer (60 second dip) wet etch are shown in Figure 5.21. Results of the 30 second BOE etch are shown in Figure 5.22. The etch exhibited selectivity to etch AlO over GaAs.

I further investigated the use of BOE as a selective etchant by evaluating AFRL sample G2 – 2558 (see Table 3.6 for layer specifications). The sample was completely oxidized (see Table 4.1). This sample was grown using GaAs- $Al_{0.9}Ga_{0.1}As$ DBR mirror layers and an $Al_{0.98}Ga_{0.02}As$ microcavity region. The reduction in aluminum content for both the DBR mirror layers and the microcavity region resulted in a longer oxidation process time and reduction in induced stress as a result of layer shrinkage. Figure 5.23 shows microscope images of the sample after oxidation. The sample (G2 – 2658C3i) was placed in a BOE solution for 60 seconds and evaluated for etch selectivity. The SEM micrographs in Figure 5.24 and Figure 5.25 show the etch selectivity, a reduction in overall layer stress and delamination, and the sample did not exhibit the dendritical growth as experienced in AFRL sample G2 – 2652A3i. The SEM micrographs in Figure 5.24 show the effects of etch selectivity as observed after milling a 20 μ mesa structure with the FIB/SEM system. The image in Figure 5.24b was used to calculate an etch rate. The BOE uniformly etched layers in the bottom DBR structure for this mesa. The etch distances were determined by examining the SEM micrographs and using the scale as shown in the figure. An etch rate of 13.3 ($\frac{nm}{sec}$) was calculated using the known etch time. Figure 5.25 shows selective etching of AlO over GaAs as experienced

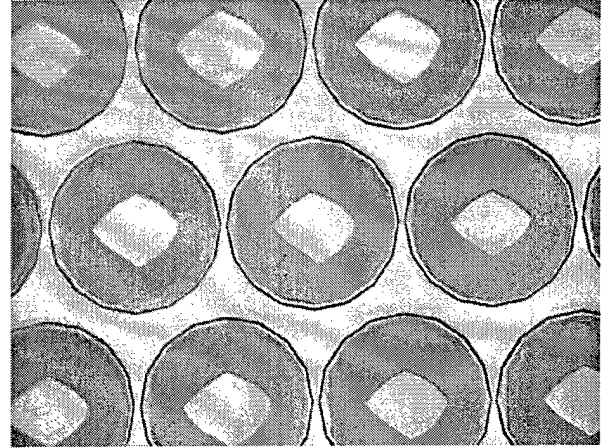
by mask alignment marks. Further studies which examine a thicker ($\sim 2000\text{\AA}$) AlO layers would be necessary to properly calibrate etch rate.

5.6 Chapter 5 Summary

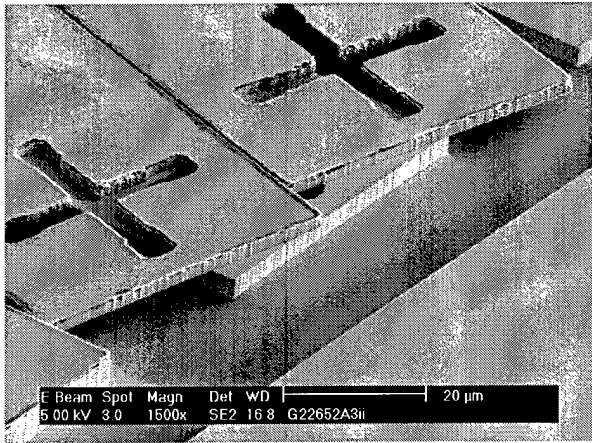
I evaluated my modeling and processing results. I found a suitable wet chemical etching solution for mesa definition to be a $H_2SO_4:H_2O_2:H_2O$ mixture to be used only after a wait time of no less than four hours. Etch rates and surface uniformity degradation were discussed. I derived a new dispersion relation for AlO as processed in the custom-built AFRL oxidation system. Newly obtained model parameters were validated against collected data and compared to previously modeled RMSE values. Finally, I performed an AlO wet chemical selective etch study and determined a suitable selective etchant to be BOE with an approximate etch rate of $13.3 \left(\frac{nm}{sec}\right)$.



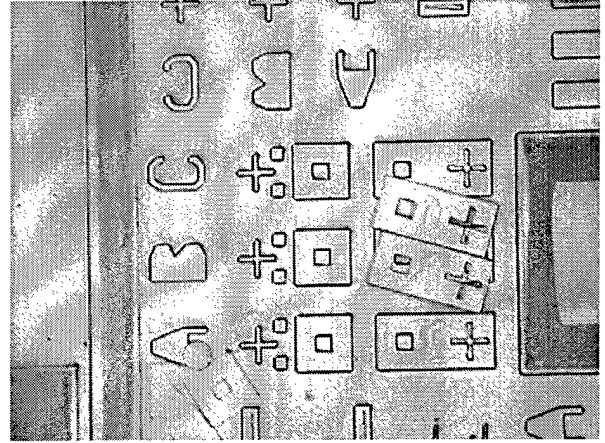
(a)



(b)



(c)



(d)

Figure 5.19 AFRL sample *G2 - 2652Aii* after 30 sec $\text{HF:H}_2\text{O}$ (2:10) etch.

Microscope images and SEM micrographs show aggressive nature of $\text{HF:H}_2\text{O}$ etch. Epitaxially grown structures were completely removed from the substrate. Top row of pictures show resultant stress bulge after $\text{HF:H}_2\text{O}$ dip while bottom layers show structures that have been displaced from the substrate. Etched mesas still attached to substrate are GaAs. The sample experienced 5 μm over-etch while in the ICP etching system.

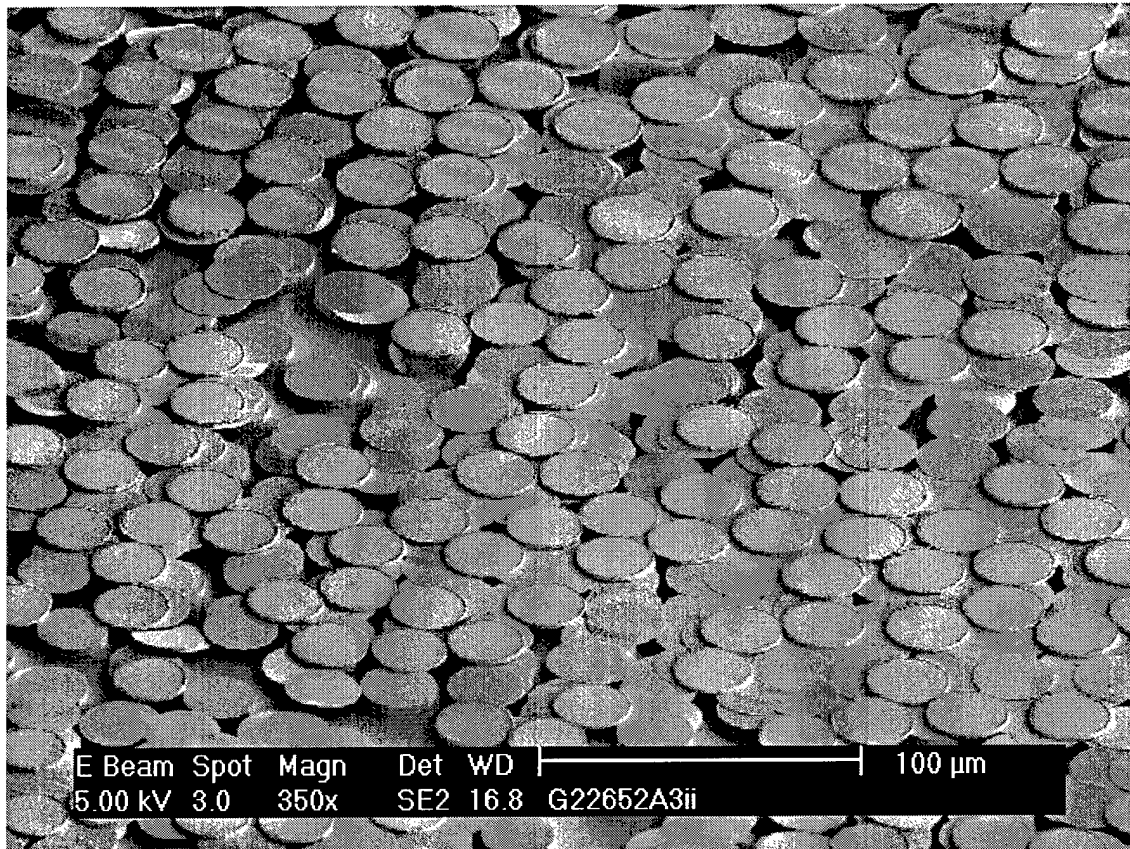
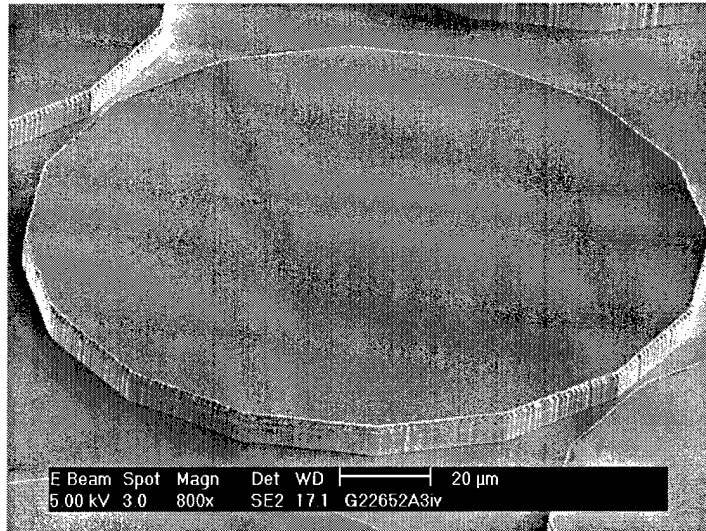
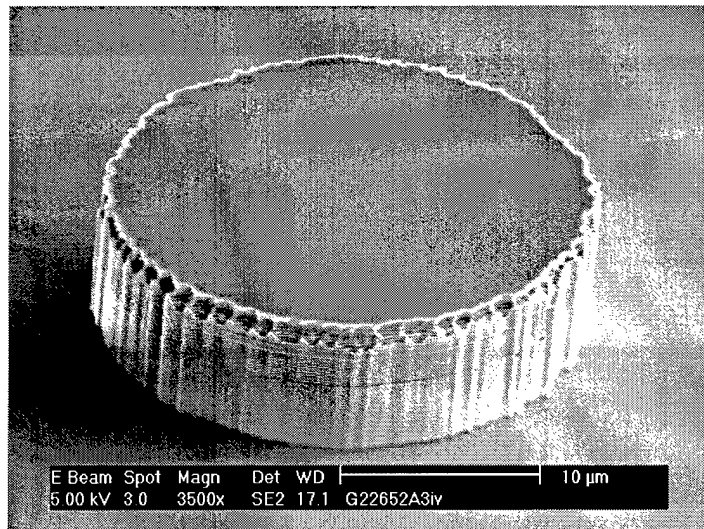


Figure 5.20 SEM micrograph of AFRL sample *G2 - 2652Aii* after 30 sec HF: H_2O (2:10) etch. Figure shows stress induced by aggressive nature of HF: H_2O etch. This removal of a microcavity structure could be used to remove an etalon (or VCSEL) structure from the GaAs substrate. After removal, this device could be placed onto a tiltable (or otherwise movable) silicon MEMS structure to create an integrated III-IV-V MEMS tiltable laser system.

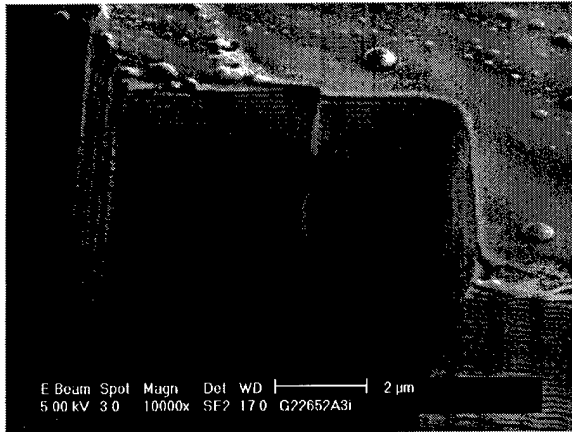


(a)

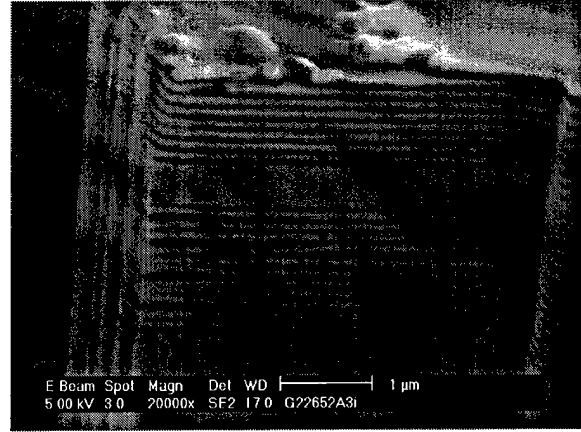


(b)

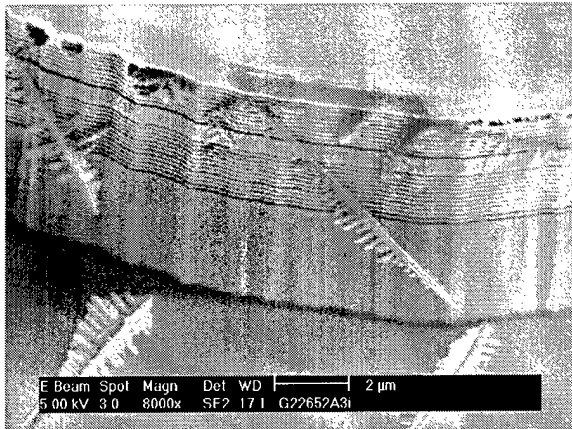
Figure 5.21 SEM micrographs of AFRL sample *G2 - 2652Aiv* after 60 seconds AZ400K etch. SEM micrographs show no evidence of selective etch by the AZ400K developer. The sampled etched for 30 seconds was not evaluated.



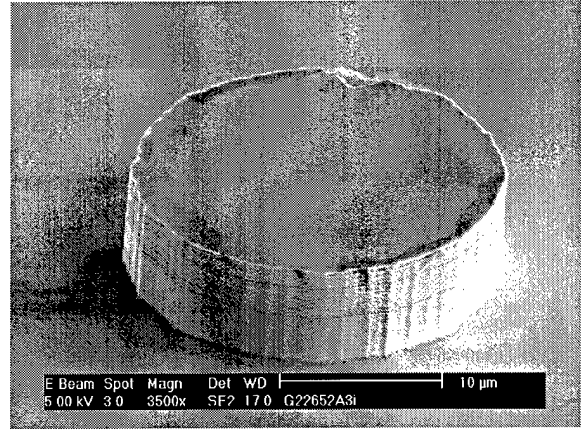
(a)



(b)



(c)



(d)

Figure 5.22 SEM micrographs of AFRL sample *G2 – 2652Ai* after 30 sec BOE etch. Figure shows (a) FIB removal of section for 20- μm mesa structure and (b) zoomed in view of layer structure. Selective etch is non-uniform due to delamination stress caused by oxidation of AlAs layers. (c) Shows dendritical formations that appeared on some structures and (d) structures that did not experience dendrite formation. Further research will be necessary to determine the reaction causing such formation.

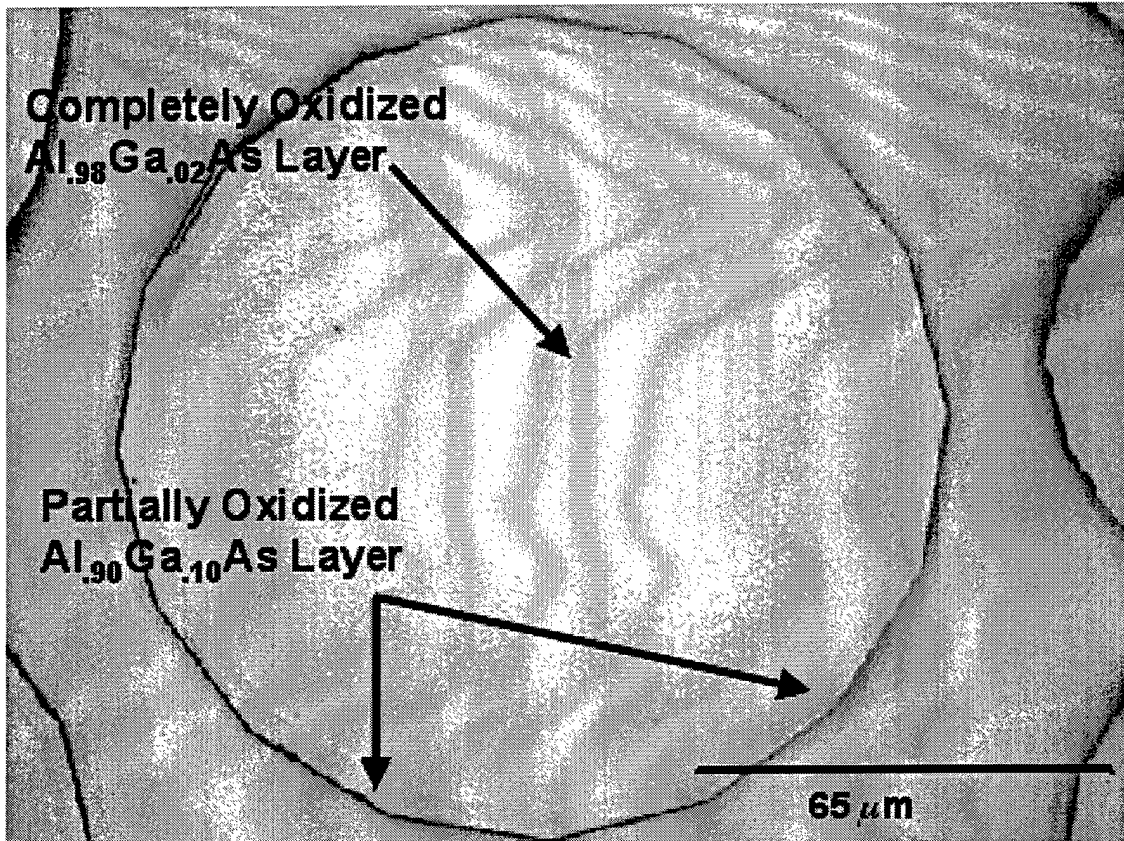
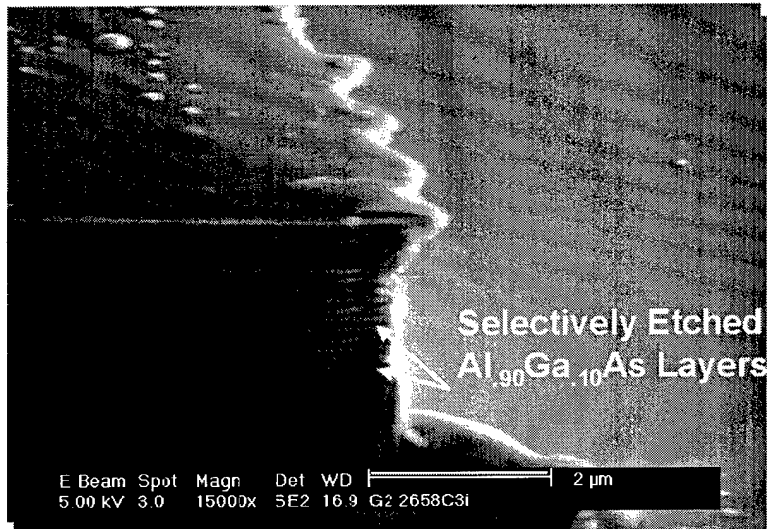
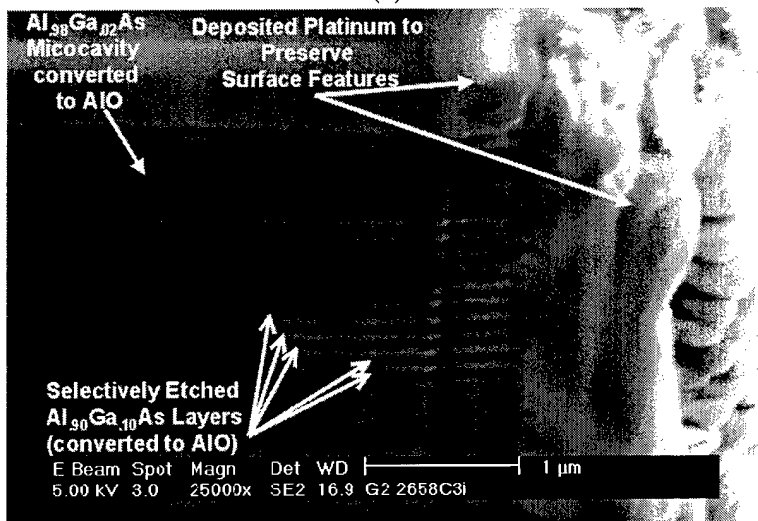


Figure 5.23 Microscope image of AFRL sample G2 - 2658 after oxidation. Images show reduced oxidation rate for $Al_{.90}Ga_{.10}As$ DBR layers. Figure shows completely oxidized large area mesa structure microcavity ($Al_{.98}Ga_{.02}As$) layer and partially oxidized DBR mirror layers

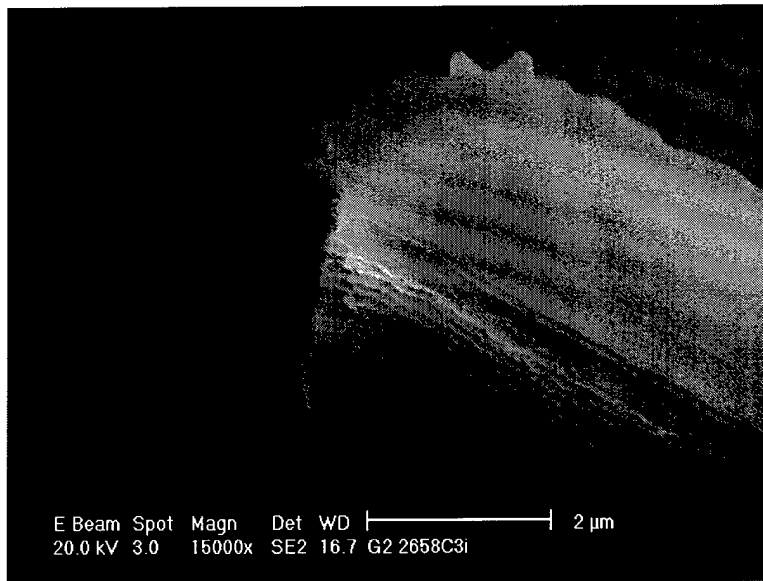


(a)

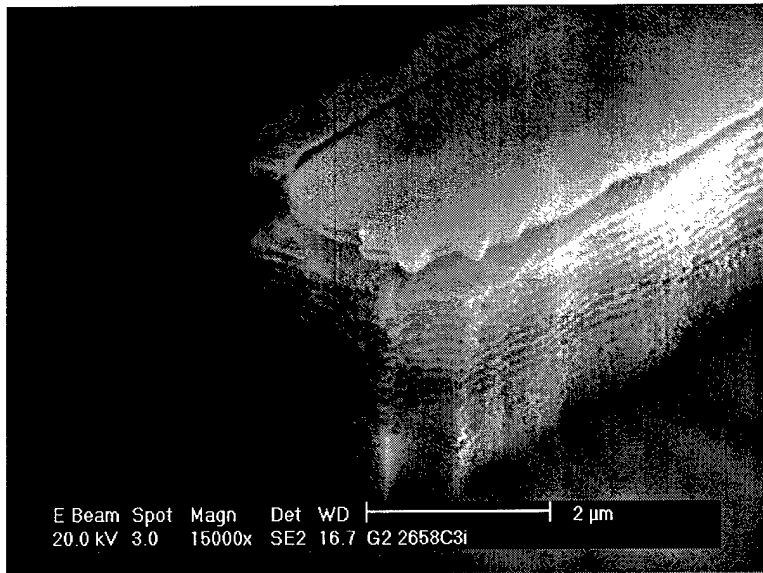


(b)

Figure 5.24 Micrographs of mesa structures on sample *G2 – 2658C3i* after 60 sec BOE etch. Figure shows (a) cross-sectional look at 20 μm mesa. Etched voids are observed on the lower DBR structure. (b) Again shows etched voids on a different 20 μm mesa structure that has been milled using FIB. A layer of Ti was deposited to preserve surface features.



(a)



(b)

Figure 5.25 Micrographs of alignment marks on sample *G2 – 2658C3i* after 60 sec BOE etch. Figure shows (a) BOE etch selectivity of AlO over GaAs, (b) clearly etched void in alignment mark structure. Both images show a greater etch extent than the previous mesa structures due to the increased exposure area during the etching process.

6. Contributions, Conclusions and Suggestions for Further Research

6.1 Contributions and Conclusions

I determined a new dispersion relation for native aluminum oxide layers. This new model parameter along with accurate molecular beam epitaxy (MBE) growth rates can be used in conjunction with other index parameter files to accurately model and grow microcavity devices. Use of buffered oxide etchant (BOE), a selective etchant for AlO layers over GaAs layers, offers the possibility to monolithically grow tunable optoelectronic devices in a single processing step thus eliminating many of the post-processing necessities of current tunable designs. This work also opens the door for studies of processing techniques for a general III-V MEMS technology. I showed that modeling and simulation can accurately predict many of the optical properties of multilayer microcavity devices. The ability to accurately model these structures prior to growth saves time and research dollars. Finally, I investigated the use of the custom-built AFRL oxidation system to oxidize large area devices and examined the process-induced stress that accompanies the conversion of AlAs to AlO. Large area optoelectronic devices are needed by both the military and civilian sectors to meet the ultra high bandwidth requirements of future optoelectronic communication and computing systems.

6.2 Further Research

My research efforts laid the foundation for future research in the areas of integrated optoelectronic systems and III-V MEMS. I now propose further research efforts and follow-on studies to my thesis. Continued work must be completed on the selective etching of converted AlO layers. A limitation of my study was the evaluation of AlO layers of varying thickness, notably thin ($< 1500\text{\AA}$) layers within a microcavity layer. Measurements of residual layer stress from volumetric layer contraction for layers of variable thickness and AlAs mole-fraction should be performed. Additionally, my specific study should be recreated for a Fabry-Perot (F-P) etalon structure composed of a $1-\lambda$

GaAs microcavity containing an embedded 1500 Å thick $Al_{0.98}Ga_{0.02}As$ layer for conversion to AlGaO. A controllable and repeatable process is necessary for the development of III-V MEMS devices such as tunable VCSELs. In addition, I propose to conduct research on the selective etching of GaAs over AlO in order to better quantify layer thicknesses. A layer-by-layer removal process allows for more accurate layer contraction measurements as a function of oxidation and also serve as a validation tool for future MBE growth. Finally, procedures to fabricate graded interface junctions that produce tapered oxide apertures, and ultimately ultra-low threshold devices, should be explored and documented.

I also recommend making changes to the existing power reflectance measurement setup currently in use by AFRL. The measured light beam must make two passes through a beam splitter before it is analyzed. This effectively eliminates 75% of the incident light. The use of a small-angle triangular-shaped mirror could be used to reflect and re-direct light at near-normal incidence without the signal loss currently experienced.

Appendix A. VCSEL Fabrication

A.1 VCSEL Fabrication Process

This section details the fabrication process for an oxide aperture VCSEL structure. The steps listed follow the epitaxial growth of a multilayer etalon structure containing InGaAs quantum well layers in the microcavity of the device. These steps are for an electrically contacted device with p-contacts on the top p-doped DBRs and n-contacts on the underside of the n-doped GaAs substrate.

1. Prepare Wafer Surface

- (a) Spin clean wafer with acetone, methanol, isopropyl alcohol and DIW 30 seconds each @ 500 rpm
- (b) N_2 blow dry
- (c) 2 min hot plate bake (HPB) @ $100^\circ C$ (removes accumulated H_2O)
- (d) cool

2. XP LOR 3A Coat

- (a) Set spinner ramp rate to 2000 rpm/sec ; and spin rate 4000 rpm
- (b) Coat sample with XP LOR 3A
- (c) Spin 30 seconds @ 4000 rpm
- (d) 2 minute HPB @ $170^\circ C$
- (e) Cool

3. 1805 Photoresist (PR) Coat

- (a) Set photoresist spinner ramp rate = 2000 rpm/sec; and spin rate 4000 rpm
- (b) Flood wafer with 1805
- (c) Spin 30 seconds @ 4000 rpm
- (d) 1 minute 15 sec HPB @ $110^\circ C$
- (e) Cool

4. Edge Bead Removal

- (a) Flood expose edge bead mask for 2 min ($2 \frac{mW}{cm^2}$)
- (b) Develop for 30 seconds using LDD26W developer
- (c) DI water rinse for 30 seconds
- (d) N_2 blow dry

5. Expose 1805 PR with VCSEL P-Ohmic Mask (01)
 - (a) Align and expose VCSEL P-Ohmic Mask (01) on MJB-3, 405 nm, 17.5 seconds ($2\frac{mW}{cm^2}$)
6. 1805 PR Develop
 - (a) 75 second spin develop with LDD26W with spinner set to 1000 rpm
 - (b) 30 second DIW rinse
 - (c) N_2 blow dry
7. Inspect Lithography
 - (a) Examine wafer alignment
 - (b) Examine to ensure 1813 completely developed.
8. O_2 plasma descum
 - (a) 4 minute O_2 plasma descum @ 200W
9. Oxide Removal Prior to Metal Deposition
 - (a) 30 second BOE (7:1) dip
 - (b) 30 second DIW rinse
 - (c) N_2 blow dry (Ensure all water has been removed from surface)
10. P-Ohmic Metal Deposition
 - (a) Deposit metal (200 Å Ti, 2550 Å Au)
11. Metal Lift Off
 - (a) Acetone Spray lift off (as necessary)
 - (b) Methanol, Isopropyl rinse, 30 seconds each
 - (c) N_2 blow dry
12. XPLOR 3A Removal
 - (a) Develop remaining XPLOR 3A using LDD26W (2-3 minute soak)
 - (b) Isopropyl rinse, DI rinse, 30 seconds each
 - (c) N_2 blow dry
13. 1818 Resist Spin On
 - (a) 2 min HPB @ 110° C
 - (b) Set photoresist spinner ramp rate = 2000 rpm/sec; and spin rate 4000 rpm

- (c) Flood wafer with 1818n resist
- (d) Spin 30 seconds @ 4000 rpm
- (e) 1 min 15 seconds HPB @ 110° C
- (f) Cool

14. Edge Bead Removal

- (a) Flood expose edge bead mask for 2 min ($2\frac{mW}{cm^2}$)
- (b) Develop for 60 seconds using 351 developer
- (c) Swab off corners and edges w/ Acetone
- (d) DI rinse 30 seconds, N_2 dry

15. Mesa Contact Mask (02)

- (a) Expose mesa contact mask for 2 min ($2mW/cm^2$)
- (b) Develop for 30 seconds using 351 developer
- (c) DI rinse 30 seconds, N_2 dry
- (d) Microscope inspect to ensure alignment
- (e) Clean mask using acetone wipe and N_2 dry

16. Step Height Profile Prior to Mesa RIE etch

- (a) Measure step height using TENCOR profilometer

17. Mesa RIE/ICP Etch

- (a) Set up reflectance monitoring equipment on Plasma-Therm ICP system
- (b) PC - double click on RIE Reflectance
- (c) Change time interval to .01 (seconds)
- (d) Mount sample on Sapphire holder using diffusion pump oil (use a SMALL amount of oil, otherwise it will contaminate wafer surface)
- (e) Etch 3-4 HL pairs past microcavity using reflectance data
- (f) Clean wafer and sapphire holder using acetone swabs

18. Post RIE/ICP Step Height Measurement (w/ 1818 resist)

- (a) Measure step height using TENCOR profilometer

19. 1818 Resist Removal

- (a) Remove remaining 1818 resist using acetone spray, acetone rinse, methanol rinse, isopropyl rinse (30 seconds each)
- (b) N_2 blow dry

- (c) Inspect resist removal using microscope
20. Post RIE Step Height Measurement (after 1818 resist removal)
- (a) Measure step height using TENCOR profilometer
21. Backside Metallization
- (a) Mount wafers to sapphire substrates using Crystal Bond 509
 - i. Heat hotplate to 130°C
 - ii. Place sapphire substrate on hotplate
 - iii. Place sample UPSIDEDOWN on melted crystal bond (ensure all air bubbles have been removed)
 - (b) Acetone rinse to remove excess crystal bond
 - (c) Methanol, Isopropanol rinse (30 seconds each)
 - (d) Coat edges of sample and exposed sapphire surface with 1818 resist
 - (e) 5 min HPB @ 110°C
 - (f) 30 sec BOE (7:1) dip, 30 sec DI rinse
 - (g) N₂ blow dry
 - (h) Standard SD n-Ohmic metalization
22. Remove Wafer from Sapphire Substrate
- (a) Score metal (on Sapphire Substrate - NOT on wafer) w/ tweezers
 - (b) Soak wafer and substrate in Acetone bath for 5 min
 - (c) Swab edges of sample with Acetone
 - (d) Heat hotplate to 130°C
 - (e) Heat substrate and remove sample once Crystal Bond 509 melts
 - (f) Remove Crystal bond from sample
 - (g) 30 sec Acetone, 30 sec Methanol, 30 sec Isopropanol rinse
 - (h) N₂ blow dry
 - (i) Clean substrate using above steps

Appendix B. Oxidation System Operation Guide

B.1 Oxidation System "How To" Manual

1. Ensure N_2 dewar is full. If not, fill up. Reconnect to lab lines and start purging lines (set valve inside lab (next to thermal probe station) to 4 cfm) Note: Full Weight of N_2 dewar is around 550 lbs (empty weight 265 lbs)
2. Refill DI water bottle on system.
3. Turn power on for temperature and pressure controllers (Master switch). BEFORE plugging in pump, make sure gate is OPEN (3) (protects valve and starts evacuating the chamber). Put the middle toggle switch (2) in the CLOSED position.
4. Make sure that N_2 and H_2O mechanical valves are CLOSED. Plug in pump.
5. Move middle toggle switch (2) to OPEN position to pump through the manifold. Pressure should get down to 50 mTorr. (see pressure gauge (3)).
6. OPEN the mechanical valve on the H_2O bottle. This pulls a vacuum on the water bottle. Let the pump work on the H_2O bottle for 5 min to remove impurities.
7. Turn ON heat tape controllers. Set to between 3 and 4. (NOTE: Flow controller is calibrated for output pressure of 1 Torr. The oxidation system operates @ 5 Torr. There is therefore an offset on the flow controller of 200 sccm. We want to flow 500 sccm through the system. The flow controller reading (4) will read 700 sccm.)
8. CLOSE the mechanical valve on the H_2O bottle and continue roughing on the chamber. OPEN throttle valve (2) until pressure is below 100 mTorr (removes excess H_2O from the system). Make sure flow controller switch is in the OPEN position and then backfill with N_2 . Turn the pump OFF.
9. Let chamber backfill with N_2 so that you can load the sample.
10. LOAD sample (microscope swings to the side for ease of loading).

11. Move the flow controller switch to the CLOSED position and turn pump ON. Pump down the chamber to 50 mTorr. Put the flow controller switch (2) in the MIDDLE position and turn N_2 valve so that you are flowing 700 sccm of N_2 (noting that this is a value with the offset included). Put the Pressure controller in Pressure mode by pressing the MODE button (note: system will automatically go to "Pos" (position) mode when the OPEN or CLOSE buttons are pressed (3))
12. Use the "SET" button on the temperature controller (1) to set desired temperature (375°C standard). See LOG book for temperature offset. The SET point on the temperature controller will usually NOT be 375°C (approx 369°C).
13. Let chuck heat to desired temperature.
14. Once chuck has reached set point, CLOSE N_2 mechanical valve and OPEN mechanical valve on H_2O bottle to begin flowing water vapor over sample (noting time in log book).
15. The system will occasionally get water droplets that propagate through the MFC. This will cause a change in pressure as well as flow rate from the MFC. You may need to manually close (only a small amount) the mechanical valve on the H_2O bottle. This should stabilize the system and allow for proper flow rates and chamber pressure to be re-established. Also make sure that the switch on the MFC is in the CONTROL POSITION (not off), otherwise the MFC will not be controlling the flow.
16. When you have reached the oxidation time, CLOSE mechanical valve on H_2O bottle. Move flow controller switch to OPEN and OPEN the throttle valve. Let system pump down to below 100 mTorr. This will remove any excess water from the system. Allow chamber to backfill with N_2 by OPENING the mechanical N_2 valve. Flow 700+ sccm of N_2 .
17. Set chuck set point back to 0°C and allow chuck to cool before removing sample.
18. To shut down the system, have N_2 flowing @ 700 sccm, pressure is at 5 mTorr. Wait until chuck cools to less than 150°C. OPEN the throttle valve, move flow controller switch to OPEN

position and turn pump OFF. Close N_2 valve AFTER removing the sample from the chuck. Turn OFF heat tape controllers. Turn OFF master power switch. Turn OFF main N_2 flow valve (next to thermal probe station). Turn OFF N_2 valve on the main N_2 tank.

Appendix C. MATLAB Simulations

C.1 MATLAB Simulations of Existing AFRL Samples

Pre-Oxidation

Post-Oxidation

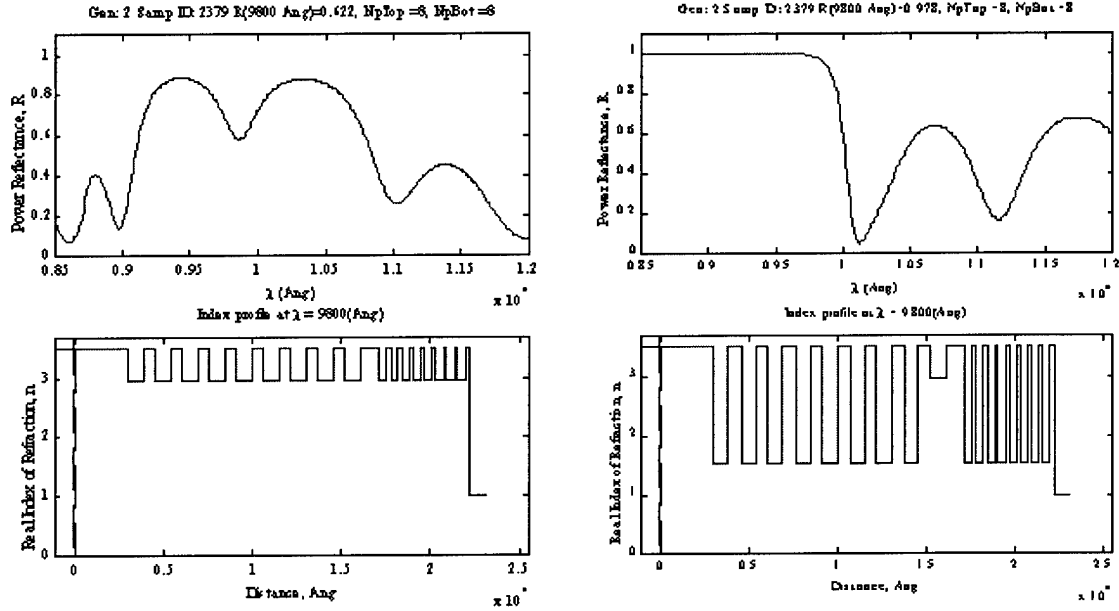
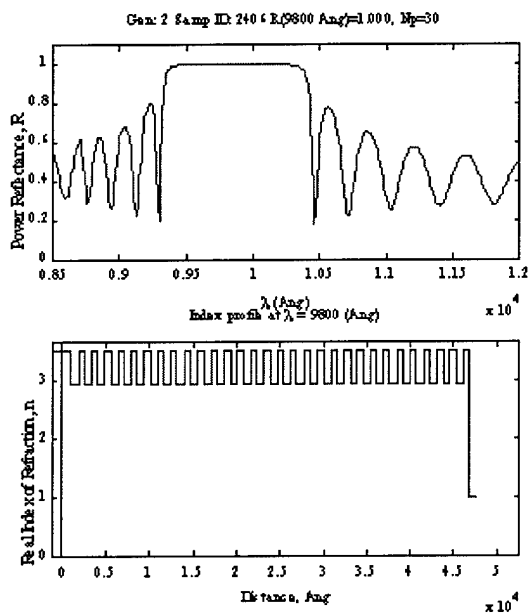


Figure C.1 Pre- and post- oxidation MATLAB simulation for AFRL sample G2 – 2379. Growth starting at substrate: GaAs(3000Å); AlAs(834Å)/GaAs(695Å), repeat 8 times; AlAs(834Å); GaAs(300Å); GaAs(780Å); AlAs(411Å)/GaAs(218Å), repeat 8 times

Pre-Oxidation



Post-Oxidation

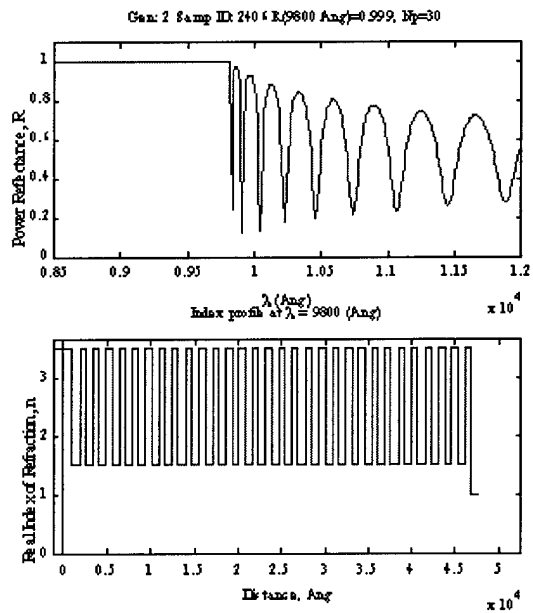


Figure C.2 Pre- and post- oxidation MATLAB simulation for AFRL sample G2 – 2406. Growth starting at substrate: GaAs(1000Å); AlAs(834Å)/GaAs(695Å), repeat 30 times; GaAs(695Å)

Pre-Oxidation

Post-Oxidation

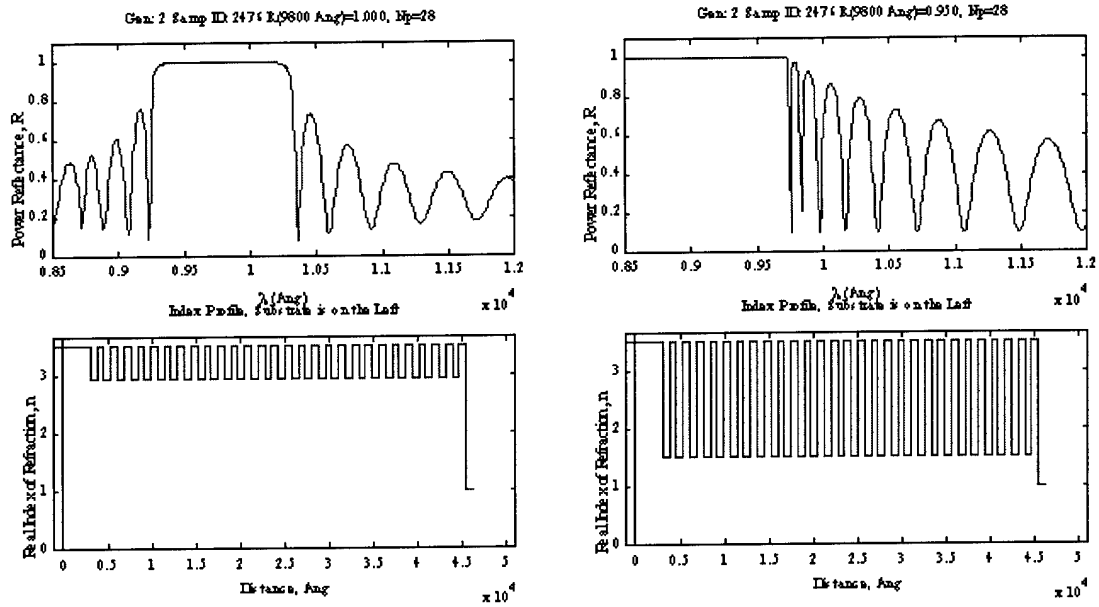
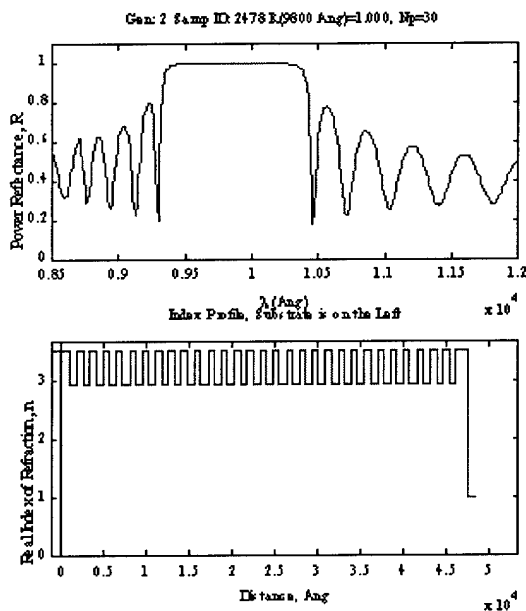


Figure C.3 Pre- and post- oxidation MATLAB simulation for AFRL sample G2 – 2476. Growth starting at substrate: GaAs(3000Å); AlAs(827Å)/GaAs(687Å), repeat 28 times

Pre-Oxidation



Post-Oxidation

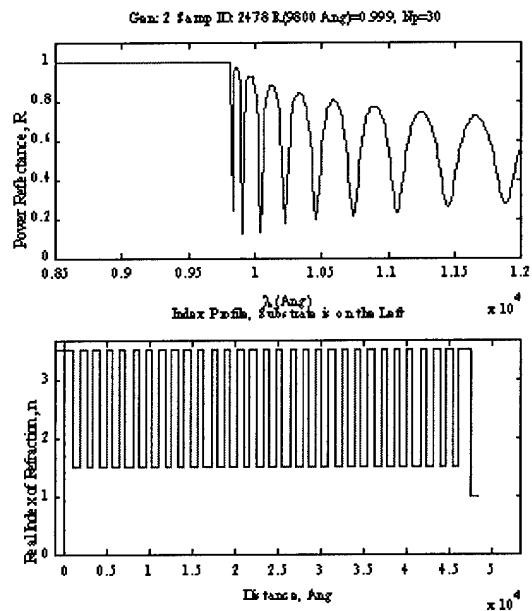


Figure C.4 Pre- and post- oxidation MATLAB simulation for AFRL sample G2 - 2478. Growth starting at substrate: GaAs(1000Å); AlAs(834Å)/GaAs(695Å), repeat 30 times; GaAs(695Å)

Pre-Oxidation

Post-Oxidation

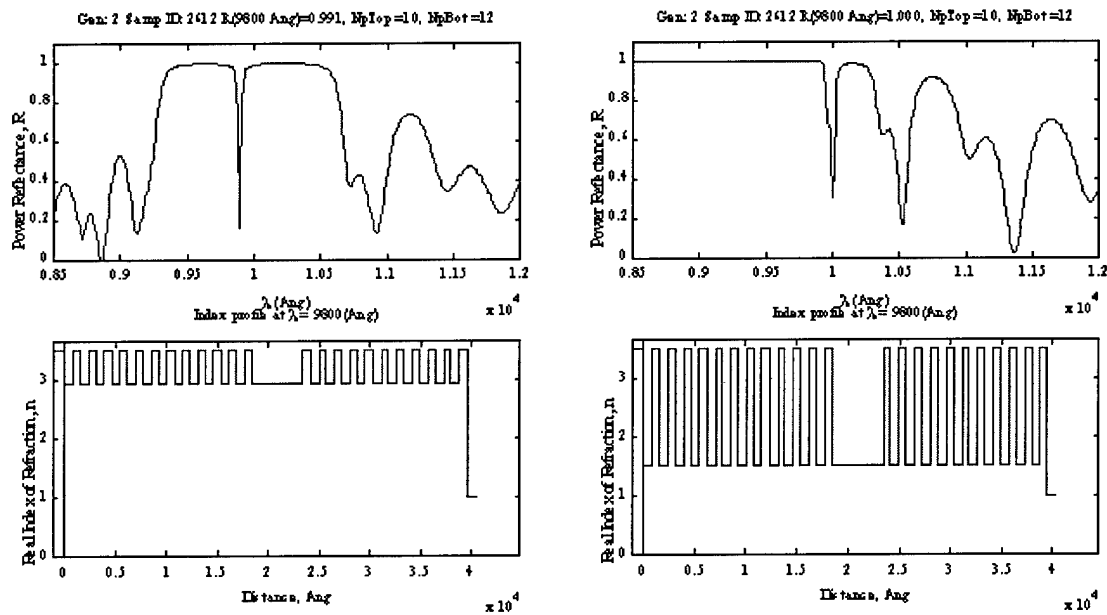


Figure C.5 Pre- and post- oxidation MATLAB simulation for AFRL sample G2 – 2612. Growth starting at substrate: AlAs(837Å)/GaAs(696Å), repeat 12 times; AlAs(5026Å); GaAs(696Å)/AlAs(837Å), repeat 10 times; GaAs(696Å)

References

1. Aspnes, D. E., et al. "Optical Properties of $Al_xGa_{1-x}As$," *Journal of Applied Physics*, 754-767 (1986).
2. Aurthur, J. "Interaction of Ga and As_2 molecular beams with GaAs surface," *Journal of Applied Physics*, 4032-4034 (1968).
3. Bagnell, R. J. *Experimental Investigation and Computer Modeling of Optical Switching in Distributed Bragg Reflector and Vertical Cavity Surface Emitting Laser Structures*. PhD dissertation, Graduate School of Engineering, Air Force Institute of Technology (AETC), Wright-Patterson AFB OH, 1995.
4. Bishop, C. M. *Neural Networks for Pattern Recognition*. Clarendon Press, 1998.
5. Chairman, Joint Chiefs of Staff, "Joint Vision 2010." From Joint Vision 2010 as written under General Shalikashvili, 1997.
6. Chang-Hasnain, C. J., et al. "Multiple wavelength tunable surface-emitting laser arrays," *IEEE Journal of Quantum Electronics*, 1332-1346 (1991).
7. Chang-Hasnain, C. J., et al. "Tunable VCSEL," *IEEE Journal on Selected Topics in Quantum Electronics*, 978-987 (2000).
8. Choquette, K. D., et al. "Advances in selective wet oxidation of AlGaAs Alloys," *IEEE Journal of Selected Topics in Quantum Electronics*, 916-926 (1997).
9. Choquette, K. D., et al. "Wavelength insensitive performance of robust selectively oxidized vertical-cavity lasers," *Photonics Technology Letters*, 1237-1239 (1995).
10. CRC. *Handbook of Chemistry and Physics, 63rd Edition*. CRC Press, 1982.
11. Dallesasse, J. M., et al. "Hydrolyzation oxidation of $Al_xGa_{1-x}As$ -AlAs-GaAs quantum well heterostructures and superlattices," *Applied Physics Letters*, 2844-2846 (1990).
12. Deal, B. E. and A. S. Grove. "General relationship for the thermal oxidation of silicon," *Applied Physics Letters*, 741-743 (1997).
13. Deng, H. and D. G. Deppe. "Very small oxide-confined vertical cavity surface emitting lasers with a bulk active region," *IEEE Journal of Quantum Electronics*, 1332-1346 (1991).
14. Eddy, S. D. and D. R. Sparks. "Application of MEMS technology in automotive sensors and actuators," *Proceedings of the IEEE*, 1747-1755 (1998).
15. Eyinck, Kurt. Not Published, 1998. Ellipsoemtry study to determine optical properties of GaAs (AFRL/MLPS, WPAFB, OH).
16. Fawcett, B. K., et al. "Medical applications of MEMS," *WESCON Conference Proceedings*, 300-302 (1995).
17. Feld, S. A. and W. L. Bernhard, "Unpublished," 2000.
18. Feld, S. A., et al. "In situ optical monitoring of AlAs wet oxidation using a novel low-temperature low-pressure steam furnace design," *IEEE Photonics Technology Letters*, 197-199 (1998).
19. Feld, S. A., et al. "In situ optical monitoring of AlAs wet Oxidation using a novel low-temperature low-pressure steam furnace design," *IEEE Photonics Technology Letters*, 197-199 (1998).

20. Forward, R. L. "Einstein's Legacy," *Omni*, 54-57 (1979).
21. Hanaamaki, Y., et al. "Fabrication of InGaAs vertical-cavity surface-emitting laser by molecular beam epitaxy and its room-temperature operation on (411)A GaAs substrates," *Jpn Journal of Applied Physics*, L150-L153 (1996).
22. Hartnagel, H. L., et al. "MEMs based on III-V-compounds for sensing applications and optical communication," *Device Research Conference. Annual 1999*, 112-115 (1995).
23. Hilfiker, J. N. and T. Wagner. "DUV-VASE Measurements of Photoresists and ARCs," *J. A. Woolam Co. Inc. - L.O.T.-Oriel GmbH Technical Manual*, 1-5 (1997).
24. Iga, K., et al. "Surface emitting semiconductor lasers," *IEEE Journal of Quantum Electronics*, 1845-55 (1988).
25. Jenkins, D. W. "Optical Constants of $Al_xGa_{1-x}As$," *Journal of Applied Physics*, 1848-1853 (1990).
26. Johs, B., et al. "Real-time monitoring and control during MBE growth of GaAs/AlGaAs Bragg reflectors using multi-wavelength ellipsometry," *Materials Science and Engineering B*, 134-138 (1997).
27. Katz, E. "Oxidation" in *VLSI Technology by S.M. Sze*. Ch 4, McGraw-Hill Book Company, 1983.
28. Kish, F. A., et al. "Planar native oxide index guided AlGaAs-GaAs quantum well heterostructure lasers," *Applied Physics Letters*, 1755-1757 (1991).
29. Knopp, K. J., et al. "Optical constants of $(Al_{0.98}Ga_{0.02}As)_y$ native oxides," *Applied Physics Letters*, 3512-3514 (1998).
30. Kubaschewski, O., et al. *Materials Thermochemistry*. Pergamon, 1993.
31. Lear, K. L., et al. "Selectively oxidized vertical-cavity surface emitting lasers with 50(1995).
32. Levenberg, K. "A method for the solution of certain non-linear problems in least squares," *Quarterly Journal of Applied Mathematics*, 164-168 (1944).
33. Loehr, J., et al., "Ultra-Low Threshold Microcavity Lasers," 1999. Work completed at AFRL, AFIT, Wright-State University, and ASC Shared Research Center.
34. Loehr, J., et al., "AFRL Data Fitting Program," 1999. C++ code compiled at AFRL to fit model parameters to measured data.
35. Lott, J. A., "Personal communication with J. A. Lott Jan-Feb 2001." Engineering Professor and Deputy Department Head at the Air Force Institute of Technology, WPAFB, OH.
36. Lynn, L. "Investing in high payoff technology concepts," *Defense Issues*, 12(18):27-33 (March 1997).
37. Macleod, H. A. *Thin Film Optical Filters*. Macmillan Publishing Company, 1986.
38. Maranowski, S. A., et al. "Native oxide top and bottom confined narrow strip p-n AlGaAs-GaAs-InGaAs quantum well heterostructure laser," *Applied Physics Letters*, 97-99 (1994).
39. Marquardt, D. W. "An algorithm for least-squares estimation of non-linear parameters," *Journal of the Society of Industrial and Applied Mathematics*, 11(2):431-441 (1979).
40. Nishiyama, N., et al. "Multi-oxide layer structure for single-mode operation in vertical-cavity surface-emitting lasers," *Photonics Technology Letters*, 606-607 (2000).

41. Ochoa, E. and W. Bernhard, "MATLAB Code Developed to Calculate Reflectance of DBR and Etalon Structures." Developed at the Air Force Institute of Technology, WPAFB OH Jul 2000 - Jan 2001.
42. Safford, E. L. "MEMS applications in tactical aircraft systems," *Avionics Systems Conference. AIAA/IEEE*, 36-41 (October 1997).
43. Saleh, B. E. A. and M. C. Teich. *Fundamentals of Photonics*. John Wiley and Sons, Inc., 1991.
44. Schawlow, A. L. and C. H. Townes. "Infrared and Optical Masers," *Physical Review*, 1940-1949 (1958).
45. Scientific Computing International, SCI, "Film Wizard Commercial Software," 2000. 6355 Corte Del Abeto, Building C105, Carlsbad Ca 92009, USA, phone 760-634-3822.
46. Sugihwo, F., et al. "Micromachined widely tunable vertical cavity laser diodes," *Journal of Microelectromechanical Systems*, 48-55 (1998).
47. Sze, S. M. *Semiconductor Devices*. John Wiley and Sons, 1985.
48. Takamori, T., et al. "Interface structure of selectively oxidized AlAs/GaAs," *Applied Physics Letters*, 659-661 (1996).
49. Thibeault, B. J., et al. "Electrical and Optical Losses in Dielectrically Apertured Vertical Cavity Lasers," *SPIE, Vertical-Cavity Surface-Emitting Lasers, San Jose California*, 86-99 (1997).
50. Tsang, W. T. "Self-terminating thermal oxidation of AlAs epilayers grown on GaAs by molecular beam epitaxy," *Applied Physics Letters*, 426 (1978).
51. Tweston, R. D., et al. "Microstructure of laterally oxidized $Al_xGa_{1-x}As$ layers in vertical cavity lasers," *Applied Physics Letters*, 19-21 (1996).
52. Wilmsen, C., et al. *Vertical-Cavity Surface-Emitting Lasers: Design, Fabrication, Characterization, and Applications*. Cambridge University Press, 1999.
53. Yang, G. M., et al. "Ultralow threshold current vertical-cavity surface emitting lasers obtained with selective oxidation," *Electronic Letters*, 886-888 (1995).
54. Yeh, P. *Optical Waves in Layered Media*. John Wiley and Sons, 1988.

Vita

Captain William L. Bernhard graduated from Mount Gilead High School in Mount Gilead, Ohio in 1991. He obtained a bachelor's degree in electrical engineering from the Rochester Institute of Technology in Rochester, NY and then was commissioned a Second Lieutenant in the United States Air Force. From January 1997 through October 1997 he was a student at the Air Force Officer Intelligence Training center located at Goodfellow AFB in San Angelo, TX. Upon graduation he received an assignment as Chief of Current Operations for the 26th Intelligence Group located on Ramstein Air Base in Germany. While in Germany he coordinated RC-135 RIVET JOINT (RJ) operations for missions in the European Command (EUCOM) area of responsibility (AOR). In addition to RJ operations, Captain Bernhard also served as part of the Measurement and Signatures Intelligence (MASINT) systems integration team for the EUCOM MASINT Liaison Officer in support of EUCOM advanced concept technology demonstrations (ACTD). He then deployed to the 4416th Intelligence Squadron, Prince Sultan Air Base, Kingdom of Saudi Arabia to serve as Chief of Flight Operations in July of 1998. Captain Bernhard flew RJ missions in support of Operation SOUTHERN WATCH and participated in Operation DESERT FOX. He then returned to Ramstein Air Base and served as primary intelligence officer for the Director of Mobility Forces (DIRMOBFOR) as part of Operation NOBLE ANVIL and other operations in and around the Kosovo AOR. Capt Bernhard was then selected to attend the Air Force Institute of Technology, Wright-Patterson AFB OH to earn a masters degree in electrical engineering. Upon graduation in March 2001 he will report to his next assignment at the National Air Intelligence Center, also located on Wright-Patterson AFB.